Interfacial engineering of $NbSe_2$ and $TaSe_2$ to enhance their electrocatalytic activity for hydrogen production

WITS
UNIVERSITY

A thesis submitted to the Faculty of Science, University of the Witwatersrand, in partial fulfilment of the requirements for the degree of Doctor of Philosophy

by

Tshwarela Kolokoto

Student number: 670850

Supervisor: Prof. Nosipho Moloto

2023

Declaration

I declare that the work reported in this thesis is my independent work, submitted for the degree of Doctor of Philosophy to the School of Chemistry, Faculty of Science at Wits University, Johannesburg. This study has not been submitted to any other institution previously for examination.

Candidate name: Tshwarela Kolokoto Date:

02/07/2023

Supervisor: Nosipho Moloto Date:

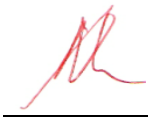

02/07/2023

Abstract

There has been a need to replace fossil fuels, develop sustainable energy systems, and alleviate the negative environmental effects. These effects can be alleviated by developing efficient processes such as water-splitting, which can produce hydrogen gas in an environmentally friendly manner and, in turn, use it as a clean fuel. However, this process requires an effective electrocatalyst comparable to Pt and cost-effective. Herein, we demonstrate that the electrocatalytic activity of $NbSe_2$ and $TaSe_2$ can be improved by metal inclusion using interfacial engineering for the hydrogen evolution reaction (HER). The readily synthesised $NbSe_2$ was decorated with 20% wt. Ni, 20% wt. Pt, 10% wt. Pt / 10% wt. Ni using two synthetic methods, namely the ex-situ and in-situ methods. The ex-situ samples had higher HER activities than the in-situ samples. Pt/PtO_2-$NbSe_2$ (derived from Pt decorated $NbSe_2$ using the ex-situ method) showed a significantly enhanced HER activity compared to bare $NbSe_2$. The Pt/PtO_2-$NbSe_2$ nanomaterial had the lowest overpotential, favourable kinetics and durability in an alkaline solution of 0.1 M KOH. The trend was as follows: Pt/PtO_2-$NbSe_2$ (Pt-decorated ex-situ) > PtO-$NbSe_2$ (Pt-decorated in-situ) > PtO/NiO-$NbSe_2$ (Pt/Ni-decorated) > Ni/NiO-$NbSe_2$ (Ni-decorated ex-situ) > $Ni_{0.5}Se/Ni(OH)_2$-$NbSe_2$ (Ni-decorated in-situ) > $NbSe_2$. In addition, $NbSe_2$ was further decorated with 20% wt. Co using both the ex-situ and in-situ synthetic methods, and 10% wt. Pt / 10% wt. Co using the in-situ method. The ex-situ sample resulted in a higher HER activity compared to the in-situ samples. In particular, Co/Co_3O_4-$NbSe_2$ nanomaterial (Co-decorated ex-situ) had the lowest overpotential, favourable kinetics and durability in an alkaline solution of 0.1 M KOH. The resultant trend was as follows: Co/Co_3O_4-$NbSe_2$ (Co-decorated ex-situ) < $Co_3O_4/CoSe_2/PtO/PtO_2$-$NbSe_2$ (Pt/Co-decorated in-situ) < $Co_3O_4/CoSe_2$-$NbSe_2$ (Co-decorated in-situ) < $NbSe_2$. Consequently, the ex-situ method was the optimum synthetic method for forming $NbSe_2$-based nanomaterials. $TaSe_2$-based nanomaterials were formed similarly. $TaSe_2$-based hybrids were formed by decorating $TaSe_2$ with 20% wt. Ni, Co and Pt using the ex-situ method. The hybrid nanomaterials resulted in higher HER activities compared to pristine $TaSe_2$ (i.e. $Pt/PtO/PtO_2$-$TaSe_2$ (Pt-decorated) > $Ni/Ni(OH)_2$-$TaSe_2$ (Ni-decorated) > Co/Co_3O_4-$TaSe_2$ (Co-decorated) > $TaSe_2$). $Pt/PtO/PtO_2$-$TaSe_2$ hybrid, in particular, resulted in the lowest overpotential under alkaline solutions (0.1 M KOH). Generally observed, was $NbSe_2$-based electrocatalysts were better than $TaSe_2$-based catalysts. In addition, the Pt-decorated ex-situ $NbSe_2$ and Pt-decorated $TaSe_2$ electrocatalysts were better than the model Pt/C catalyst, with the prior being the best overall. This is attributed

to the basal sites of the $NbSe_2$ and $TaSe_2$. The ex-situ method was better than the in-situ method and this was due to the presence of metallic particles and the minimization of oxidation compared to the latter.

Dedication

I dedicate this to my future, mother, partner, family, and friends.

Acknowledgements

- Firstly, I would like to express my gratitude to God almighty for the life he has given me and the strength to push to the finish line.
- Most importantly, I would like to say thank you to my mother for her unconditional love and support. All the long phone calls we've had where I was updating her on my progress.
- To my partner, Mr Thato Choshi, thank you for always being there when times were tough. You always pushed me to work and ensured I was in the right headspace. Thank you for Snow, he has been the breath of fresh air that I needed. I love you.
- I would also like to express my sincere gratitude to my supervisor Prof Nosipho Moloto for her guidance, advice, and support throughout my academic career. Thank you for inspiring me to push beyond my limits and reach for the stars. Your guidance will go a long way. We did it!
- Thank you to the Wits MMU unit for providing the microscopic instrumentation and expertise necessary to get the best images possible, NRF for funding, NIMSA for XPS, and Centre for Nanostructures and Advanced Materials CSIR for HRTEM.
- I would also like to express my gratitude to all my colleagues who have helped me throughout the project. Thank you, Dr Victor Mashindi, for the collaboration in this work, CATOMAT and nano-WEBS for the weekly seminars and progress report meetings that helped me with the challenges I encountered.
- Special thanks to my close friends in science, Miss Khanani Machumele, Miss Mulweli Nethathe, Dr Siyabonga Nkabinde, Dr Ndivhuwo Shumbula and Dr Zakhele Ndala, for their support and inspiration.
- To my colleagues at Deloitte, thank you for understanding and giving me time to complete my research. Without your support and understanding, I would not be here.

Presentations

- Oral presentation at the Catalysis Organometallics and materials' (CATOMAT) seminar held at the Chemistry department, the University of the Witwatersrand, on 04/05/2017 – 30/11/2022.
- Weekly nano-WEBS progress meetings held at the Chemistry department, the University of the Witwatersrand, on 01/05/2017 – 30/11/2022.
- Poster presentation at the 7th Annual Gauteng Nanosciences Young Researchers' Symposium (2017 SANi-NYRS) on 20/10/20217. (Best poster 3rd place).
- Poster presentation at the 8th cross-faculty postgraduate symposium (WITS) 25/10/2017 - 26/10/2017. (Best poster 3rd place).
- Oral presentation at the Catalysis Organometallics and materials' (CATOMAT) seminar held at the Chemistry department, the University of the Witwatersrand, on 23/03/2018.
- Poster presentation at the 7th international conference on nanoscience and nanotechnology (NanoAfrica 2018) from 22/04/2018 - 24/04/2018. (Best poster 3rd place).
- Poster presentation at the 70th Annual Meeting of the International Society of Electrochemistry from 04/08/2019 - 09/08/2019.
- Poster presentation at the 9th SANi Nanoscience's young researchers' symposium (NYRS) to be held at Future Africa, the University of Pretoria, on 12/11/2019.
- Oral presentation at the Catalysis Organometallics and materials' (CATOMAT) seminar held at the Chemistry department, the University of the Witwatersrand, on 28/02/2020.
- Oral presentation at the PhD seminar (WITS) on 30/09/2021. (Best oral presentation 3rd place).

Publications

Publication emanating from this study

- **T. Kolokoto**, V. Mashindi, R. Kadzutu-Sithole, L. Machogo-Phao, Z. Ndala, N. Shumbula, S. Nkabinde, G. Ngubeni, S. Gqoba, K. Mubiayi, N. Moloto, The effect of the metal and selenium precursors on the properties of $NbSe_2$ and Nb_2Se_9 nanostructures and their application in dye-sensitized solar cells *RSC Adv.*, **2021**, 11, 31159–31173. {I performed all the synthesis and electrochemical work and analysed samples with XRD, TEM/EDX, SEM, UV-vis spectroscopy, and FTIR. HRTEM was conducted by the Centre for Nanostructures and Advanced Materials, and XPS by NIMSA. Dr V. Mashindi helped with the synthesis of the hybrid materials. Dr Z. Ndala, Dr S. Nkabinde, Dr N. Shumbula, Dr R. Kadzutu-Sithole, Dr L. Machogo-Phao, G. Ngubeni, S. Gqoba, and K. Mubiayi helped with the brainstorming of ideas and discussion of results. Prof. N. Moloto conceptualized the project and helped with correcting the manuscript}.
- **T. Kolokoto**, V. Mashindi, S. Nkabinde, Z. Ndala, N. Shumbula, N. Moloto, Activating the inert two-dimensional $NbSe_2$ surface by decorating with Ni and Pt-based nanoparticles to enhance the electrocatalytic activity to produce hydrogen, *Energy Advances*, **2023**, (In press, Manuscript ID: TA-ART-02-2023-000711) {I performed all the synthesis and electrochemical work, analysed samples with XRD and TEM. HRTEM was conducted by the Centre for Nanostructures and Advanced Materials, and XPS by NIMSA. Dr V. Mashindi helped with the synthesis of the hybrid materials. Dr Z. Ndala and Dr S. Nkabinde helped run electrochemical experiments and data processing. Dr N. Shumbula helped with the brainstorming of ideas and discussion of results. Prof. N. Moloto conceptualized the project and helped with correcting the manuscript}.
- **T. Kolokoto**, V. Mashindi, S. Nkabinde, Z. Ndala, N. Shumbula, M.J. Moloto, N. Moloto, Ni and Co-decorated $NbSe_2$ nanoflowers: properties and electrochemical activity toward the hydrogen evolution reaction, *Journal of Electroanalytical Chemistry*, **2023**, (To be submitted).
- **T. Kolokoto**, V. Mashindi, S. Nkabinde, Z. Ndala, N. Shumbula, M.J. Moloto, N. Moloto, 2H-$NbSe_2$ and $TaSe_2$ as superior electrocatalysts towards the hydrogen evolution reaction, *ChemElectroChem*, **2023**, (To be submitted).

Publications emanating from expertise gained in this study

- E. Mposa, **T. Kolokoto**, G.N. Ngubeni, L. Machogo-Phao, N. Moloto, Gold diethyldithiocarbamate complex as a single-source precursor for gold sulphide dye-sensitized counter electrode, *Royal Society of Chemistry*, **2023**, (Manuscript submitted, Manuscript ID: YA-ART-02-2023-000073) {I contributed to the electrochemical characterization and discussed the results with the first author}.
- O. B Nchoe, N. P. Shumbula, Z. B. Ndala, S. S. Nkabinde, **T. Kolokoto**, P. Tetyana; K. Sikhwivhilu, Facile synthesis of Ag_2O, Ag_2S and AgCl NPs for the photocatalytic degradation of Rhodamine B dye, Optical Materials, **2023,** (Manuscript submitted, Manuscript Number: OM-D-23-00607) {I contributed with the transmission electron microscopy analysis and discussed the results with the first author}.
- Z. B. Ndala, S. S. Nkabinde, N. P. Shumbula, O. A. Makgae, **T. Kolokoto**, M. Ek, S. S. Gqoba, C. E. Linganiso, P. S. Mdluli4, N. Moloto, Unravelling the effects of surface functionalization on the catalytic activity of $ReSe_2$ nanostructures towards the hydrogen evolution reaction, *SSRN*, **2022**, {I contributed to the electrochemical characterization and discussed the results with the first author}.
- Z. Ndala, N. Shumbula, S. Nkabinde, **T. Kolokoto**, E.C. Linganiso, S. S. Gqoba, N. Moloto, Electrocatalytic activity of pristine and electrochemically activated $SnSe_2$ nanoplates for the hydrogen evolution reaction, *J. Electroanal. Chem.*, **2022**, 116464. {I contributed to the electrochemical characterization and discussed the results with the first author}.
- **R. Kadzutu-Sithole**, L. F. E. Machogo-Phao, T. Kolokoto, M. Zimuwandeyi, S, S. Gqoba, K. P. Mubiayi, M. J. Moloto, J. Van Wyk, N. Moloto, Elucidating the effect of precursor decomposition time on the structural and optical properties of copper(I) nitride nanocubes, *RSC Adv.*, **2020**, 10, 34231–34246. {I contributed to the graphic illustrations and discussed the results with the first author}.
- R. K. Sithole, **T. Kolokoto**, L. F.E. Machogo, G. N. Ngubeni, M. J. Moloto, J. Van Wyk, N. Moloto, Simultaneous capping and substitution of nitrogen ions of Cu_3N nanocrystals with sulfur ions using DDT as a co-surfactant to form chalcocite and digenite nanocrystals, *Materials Chemistry and Physics*, **2020**, 251, 123074. {I contributed to the graphic illustrations and discussed the results with the first author}.

- Z. Ndala, N. Shumbula, S. Nkabinde, **T. Kolokoto**, O. Nchoe, P. Shumbula, Z. N. Tetana, E. C. Linganiso, S. S. Gqoba, N. Moloto, Evaluating the effect of varying the metal precursor in the colloidal synthesis of $MoSe_2$ nanomaterials and their Application as electrodes in the hydrogen evolution reaction, *Nanomaterials*, **2020**, *10* (9), 1786. {I contributed to the electrochemical characterization and discussed the results with the first author}.
- S.S Nkabinde, Z. B. **Ndala, N. P.** Shumbula, T. Kolokoto, O. Nchoe, G. N. Ngubeni, K. P. Mubiayi, N. Moloto, Delineating the role of crystallinity in the electrocatalytic activity of colloidally synthesized MoP nanocrystals, *New Journal of Chemistry*, **2020,** *44* (33), 14041-14049. {I contributed to the electrochemical characterization and discussed the results with the first author}.

Table of Contents

List of Figures

Chapter 1

Chapter 2

Chapter 3

Chapter 3 Supplementary information

Chapter 5

Chapter 5 Supplementary information

Chapter 6

List of Tables

List of Symbols and Abbreviations

BET – Brunauer-Emmet-Teller

CDW – Charge density wave

Cdl – Electrochemical double-layer

Cs – Specific capacitance

CVD – Chemical vapour deposition

CV – Cyclic voltammetry

ECSA – Electrochemically active surface area

EIS – Electrochemical impedance spectroscopy

EXAFS – Extended X-ray adsorption fine structure

H_{ad} – Hydrogen adsorption

HER – Hydrogen evolution reaction

j_0 – Exchange current density

LSV – Linear sweep voltammetry

OH_{ad} – Hydroxyl group adsorption

OER – Oxygen evolution reaction

ODE – Octadecene

OLA – Oleylamine

Rct – Charge transfer resistance

RGO – Reduced graphene oxide

RHE – Reversible hydrogen electrode

SHE – Standard hydrogen electrode

TEM – Transmission electron microscope

TMDC – Transition metal dichalcogenide

XRD – X-ray diffraction

XPS – X-ray photoelectron spectroscopy

Synopsis

1. Brief description of the thesis

The study aimed to enhance the electrocatalytic activity of 2D transition metal dichalcogenides (TMDCs) ($NbSe_2$ and $TaSe_2$) towards hydrogen production under alkaline conditions. This was achieved through interfacial engineering – decoration of the 2D TMDC nanomaterials with transition metals (10% wt. Pt, Ni, Co, or mixed metals) to form hybrid nanomaterials. Consequently, the thesis is structured is as follow:

- **Chapter 1:** consists of the background of the study along with the problem statement, rationale, as well as aims and objectives of the study.
- **Chapter 2:** reviews the literature outlines all the concepts discussed in each chapter of the thesis.
- **Chapter 3:** describes the synthesis and characterisation of $NbSe_2$ and $NbSe_2$-based hybrid nanomaterials decorated with 20% wt. Pt, 20% wt. Ni, 10% wt. Pt /10% wt. Ni (mixed metals) and their performance as electrocatalysts in hydrogen evolution reaction (HER). This chapter is currently in press (Manuscript ID: TA-ART-02-2023-000711).
- **Chapter 4:** offers further enhancement of the $NbSe_2$-based hybrid nanomaterials' electrocatalytic activity toward HER through the decoration of 20% wt. Co, 10% wt. Pt / 10% wt. Co.
- **Chapter 5:** describes the synthesis and characterisation of $TaSe_2$ and $TaSe_2$-based hybrid nanomaterials (decorated with 20% wt. Pt, Ni, and Co). These materials' HER activity was evaluated and resulted in the enhancement of the $TaSe_2$ electrocatalyst.
- **Chapter 6:** provides general conclusions of the study and recommendations for future work.

Chapter 1

General Background

1.1 Introduction

For decades, there has been a drive to diversify fossil fuels-derived energy with clean, sustainable, environmentally friendly, and secure alternatives [1, 2, 3-5]. This is due to the increasing demand for energy, high and unstable oil prices, as well as the issue of environmental preservation [6]. As such, fuel cells have been considered an alternative to combustion-based technologies currently used in many power plants and passenger vehicles. Fuel cells combine hydrogen and oxygen to produce heat, electricity, and water. They use pure hydrogen to operate appropriately [6-8]. Hydrogen is a highly efficient and clean (low pollution) energy carrier [9]. Safe storage and delivery of hydrogen gas are essential aspects in maintaining the economy of this gas [10]. Since hydrogen cannot be produced naturally on earth because it exists in the form of compounds (water, coal, and other various hydrocarbons), hydrogen can be made by essentially converting these compounds into hydrogen [9]. The following methods are currently used to produce hydrogen: steam-methane reforming and coal gasification chemical processes [10]. Various hydrogen production methods are summarised in Fig. 1, along with their advantages and disadvantages (Table 1) [11].

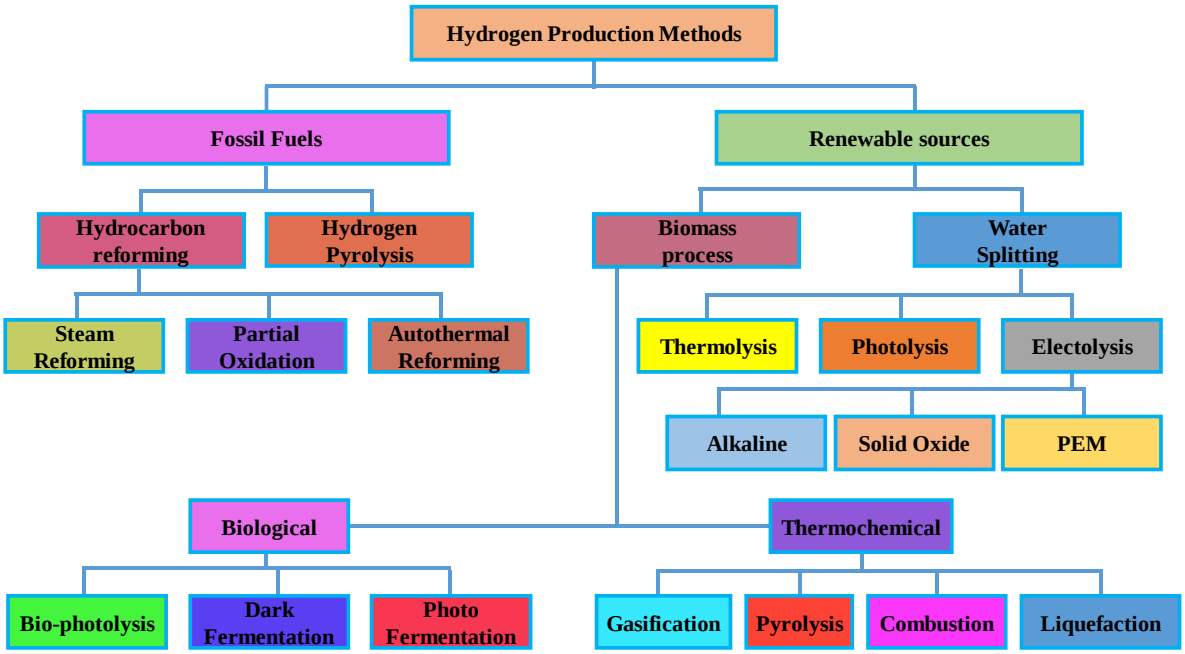

Fig. 1: Various hydrogen production methods.

Table 1: Various hydrogen production methods along with their advantages, disadvantages, efficiency, and cost [11-14]

Hydrogen production method	**Advantages**	**Disadvantages**	**Efficiency**	**Cost ($/kg)**
Steam Reforming Partial Oxidation	Developed technology & Existing infrastructure Estabilished technology	Produced CO, CO_2 unstable supply. Along with H_2 production, produced heavy oils and petroleum coke	74-85 60-75	2.27 1.48
Auto thermal Reforming	Well estabilished technology & Existing infrastructure	Produced CO_2 as a by-product, use of fossil fuels	60-75	1.48
Bio photolysis	Consumed CO_2, produced O_2 as a by-product, working under mild conditions	Low yields of H_2, sunlight needed, large reactor required, O_2 sensitivity, high cost of material	10-11	2.13
Dark Fermentation	Simple method, H_2 produced without light, no limitation O_2, CO_2-neutral, involves to waste recycling	Fatty acids elimination, low yields of H_2, low efficiency, necessity of huge volume of reactor	60-80	2.57
Photo Fermentation	Involves to water recycling, used different organic waste waters, CO_2-neutral	Low efficiency, low H_2 production rate, sunlight required, necessity of huge volume of reactor, O_2-sensitivity	0.1	2.83
Gasification	Abundant, cheap feedstock and neutral CO_2	Fluctuating H_2 yields because of feedstock impurities, seasonal availability and formation of tar	30-40	1.77-2.05
Pyrolysis	Abundant, cheap feedstock and CO_2-neutral	Tar formation, fluctuating H_2 amount because of feedstock impurities and seasonal availability	35-50	1.59-1.70
Thermolysis	Clean and sustainable, O_2-by product, copious feedstock	High capital costs, elements toxicity, corrosion problems	20-45	7.98-8.40
Photolysis	O_2 as by-product, abundant feedstock, no emissions	Low effieciency, non-effective photocatalytic material, requires sunlight	0.06	8-10
Electrolysis	Established technology, zero emission, existing infrastructure O_2 as by-product	Storage and transportation problems	60-80	10.30

Moreover, hydrogen can be produced through the environmentally friendly electrochemical water splitting technique that yields water as the by-product [15]. Hydrogen fuel generated from water electrolysis has no contaminants compared to the hydrogen gas from reformed hydrocarbons that tend to poison the fuel cell electrocatalyst, reducing their lifetime and efficiency [16]. Therefore, hydrogen is an excellent alternative to fossil fuels [10]. Electrolysis can be powered using renewable energy technologies such as photovoltaics or photolysis, or photoelectrochemical processes can be used and thus result in entirely renewable and clean hydrogen production processes [19]. Fig. 2 highlights the different renewable sources of hydrogen production [17, 18].

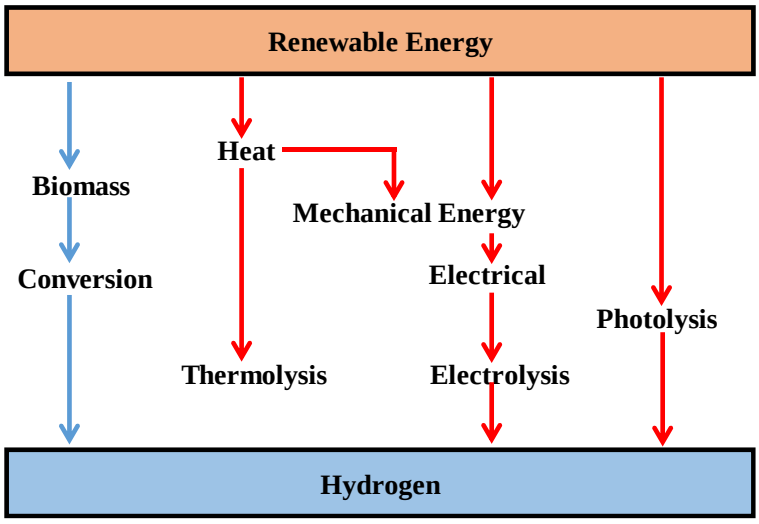

Fig: 2: Schematic of a sustainable strategy to generate H_2.

Electrolysis of water is the preeminent electrochemical method for producing pure hydrogen at room temperature and is the main alternative to hydrogen synthesis from fossil fuels [20-24]. Efficient electrocatalysts are recommended as cathode materials in the water electrolysis cell because they can produce large amounts of hydrogen at reduced overpotentials by simply accelerating the kinetics of the hydrogen evolution reaction (HER) [21-23]. However, storage and delivery remain significant challenges [25-28]. Pt-based electrocatalysts are the most efficient and stable electrocatalysts used for the HER and operate under highly corrosive conditions (strong acids), increasing the overall set-up's cost and safety concerns [25, 29-31]. Moreover, Pt is an expensive noble metal which increases the cost of water electrolysers [21-23]. Developing new, cheap, and effective HER electrocatalysts have become a significant target for efficient hydrogen production on large scales [6, 32, 33]. HER under alkaline conditions seems to be a potential substitute that increases the stability of platinum group

metals (PGMs) based water electrolyser and paves the way for the possibility of using transition metal-based catalysts [25, 34-36]. This study focuses on the HER in alkaline media for sustainable hydrogen production using 2D transition metal dichalcogenide (TMDC) based hybrids as electrocatalysts through electrolysis. TMDC-based hybrid electrocatalysts have received much attention for hydrogen production from water splitting because they represent an easy way to solve the current energy and environmental problems [37-41]. Several methods have been developed, including the wet-chemistry route, to synthesise TMDC-based hybrid nanoparticles of different structures (nanocomposites with metal nanoparticles of different sizes, Janus, and core-shell), dimensions, and various morphologies [42-46]. Among these methods, solvothermal, hydrothermal, and sol-gel are widely used [47, 48]. As such, it is still essential for the scientific and industrial worlds to develop a new facile and one-step method for producing semiconductor-metal hybrids with monodispersed shapes and sizes [6]. In this study, TMDC-based ($NbSe_2$ and $TaSe_2$) hybrid nanomaterials were synthesised using the colloidal synthesis one-step reaction and chemical vapour deposition (CVD) synthesis to test their potential to substitute Pt as an electrocatalyst for efficient hydrogen production.

1.2 Problem statement

Although Pt-based electrocatalysts are the most efficient for hydrogen production in the electrolysis of water, this noble metal is rare and expensive [2]. As a result, the entire process is costly. Furthermore, even though 2D-based hybrid nanomaterials have the potential to replace Pt, the main difficulty in synthesising these nanoparticles is in the weak interaction between the semiconductor and the metal [6, 45, 49, 50]. Although water splitting is an eco-friendly technique for hydrogen production, it requires plenty of energy due to its large overpotential for HER [10]. In addition, the HER in alkaline media suffers from sluggish reaction kinetics due to the additional water dissociation step [25, 51, 52]. Therefore, the need for a catalyst with outstanding electrocatalytic activity and lifespan is still imminent [10, 53]. Most importantly, even though hydrogen production has been extensively researched, sustainable hydrogen production is a great challenge [25, 54].

1.3 Rationale

Therefore, the aim is to enhance hydrogen gas production by forming and using TMDC-based hybrid nanomaterials. To investigate the interaction of the highly active metallic nanoparticles to the TMDC by using two methods to form the hybrids: ex-situ and in-situ. The overpotential of TMDC will be improved by the addition of highly active metallic nanoparticles to form

hybrids, potentially improving the sluggish kinetics. Heterostructuring of TMDC nanomaterials with transition metals has been proven to increase their electrocatalytic activity for HER [10].

1.4 Aim and Objectives

This work aimed to use the heat-up colloidal synthesis method to synthesise and characterise $NbSe_2$ and $TaSe_2$ for application as alternative electrocatalysts to pure Pt for hydrogen production. Generally, 2D TMDC nanomaterials have less desirable electrocatalytic activity due to fewer active sites compared to Pt. To circumvent this, they were decorated with transition metals (Ni, Co, Pt, Ni/Pt and Co/Pt) to enhance their activity. To achieve the forementioned aim, the following objectives were identified:

- Synthesis and characterisation of $NbSe_2$ and $TaSe_2$.
- Synthesis and characterisation of $NbSe_2$-based hybrids.
- Synthesis and characterisation of $TaSe_2$-based hybrids.
- Application of the synthesised $NbSe_2$ and $TaSe_2$ nanomaterials and their subsequent hybrid nanomaterials as electrocatalysts for HER under alkaline conditions.

1.5 References

[1] M. S. Faber, S. Jin, *Energy Environ. Sci.*, 2014, 7, 3519-3542.

[2] K. Zhu, C. Li, Z. Jing, X. Liu, Y. He, X. Lv, Y. Wang, K. Liu, *FlatChem*, 2019, 18, 100140.

[3] S. Chu, A. Majumdar, *Nature*, 2012, 488, 294-303.

[4] V. R. Stamenkovic, D. Strmcnik, P. P. Lopes, N. M. Markovic, *Nat. Mater.*, 2016, 16, 57-69.

[5] Z. W. Seh, J. Kibsgaard, C. F. Dickens, I. Chorkendorff, J. K. Nørskov, T. F. Jaramillo, *Science*, 2017, 355.

[6] A. Mezni, M. M. Ibrahim, M. El-Kemary, A. A. Shaltout, N. Y. Mostafa, J. Ryl, T. Kumeria, T. Altalhi, M. A. Amin, *Electrochimica Acta*, 2018, 290, 404-418.

[7] A. F. Ghenciu, *Curr. Opin. Solid State Mater. Sci.*, 2002, 6, 389-399.

[8] A. Kirubakaran, S. Jain, R. K. Nema, *Renew. Sustain. Energy Rev.*, 2009, 13, 2430-2440.

[9] K. Mazloomi, C. Gomes, *Renew. Sustain. Energy Rev.*, 2012, 16, 3024-3033.

[10] U. Gupta, C. N. R. Rao, *Nano Energy*, 2017, 41, 49-65.

[11] S. S. Kumar, V. Himabindu, *Materials Science for Energy Technologies*, 2019, 2, 442-454.

[12] J. Chi, Y. Hongmei, *Chin. J. Catal.*, 2018, 39, 390-394.
[13] D. A. J. Rand, *J. Solid State Electrochem.*, 2011, 15, 1579-1622.
[14] A. Züttel, *Naturwissenschaften*, 2004, 91, 157-172.
[15] A. A. Gewirth, M. S. Thorum, *Inorg. Chem.*, 2010, 49, 3557-3566.
[16] S. Srinivasan, R. Mosdale, P. Stevens, C. Yang, *Annu. Rev. Energy*, 1999, 24, 281-328.
[17] N. S. Lewis, D. G. Nocera, *Proc. Natl. Acad. Sci.*, 2006, 103, 15729-15735.
[18] J. A. Turner, *Science*, 1999, 285, 687.
[19] S. Warren, Photoelectrochemical Splitting of Water: Using Porphyrins as Catalysts. DOE ERULF Program, Whitman College, *National Renewable Energy Laboratory.*, 2000. p. 4
[20] Y. Shi, B. Zhang, *Chem. Soc. Rev.*, 2016, 45, 1529-1541.
[21] J. A. Turner, *Science*, 2004, 305, 972-974.
[22] S. Bhavsar, M. Najera, R. Solunke, G. Veser, *Catal. Today*, 2014, 228, 96-105.
[23] W. Yan, S. K. Hoekman, *Environ. Prog. Sustain. Energy*, 2014, 33, 213-219.
[24] M. Carmo, D. L. Fritz, J. Mergel, D. Stolten, *Int J Hydrog Energy*, 2013, 38, 4901-34.
[25] N. Mahmood, Y. Yao, J. Zhang, L. Pan, X. Zhang, J. Zou, *Adv. Sci.*, 2018, 5, 1700464-1700487.
[26] M. Fellet, D. M. Tiede, *MRS Bull.*, 2017, 42, 190.
[27] L. Qing, N. Mahmood, J. Zhu, Y. Hou, S. Sun, *Nano Today*, 2014, 9, 668.
[28] N. Mahmood, C. Zhang, H. Yin, Y. Hou, *J. Mater. Chem. A.*, 2014, 2, 15.
[29] J. Li, M. Yan, X. Zhou, Z.-Q. Huang, Z. Xia, C.-R. Chang, Y. Ma, Y. Qu, *Adv. Function. Mater.*, 2016, 26, 6785.
[30] P. Xiao, W. Chen, X. Wang, *Adv. Energy Mater.*, 2015, 5, 1500985.
[31] R. Subbaraman, D. Tripkovic, D. Strmcnik, K.-C. Chang, M. Uchimura, A. P. Paulikas, V. Stamenkovic, N. M. Markovic, *Science*, 2011, 334, 1256.
[32] Y. Yan, B. Xia, Z. Xu, X. Wang, *ACS Catal.*, 2014, 4, 1693-1705.
[33] M. S. Faber, S. Jin, *Energy Environ. Sci.*, 2014, 7, 3519-3542.
[34] X. Zou, Y. Zhang, *Chem. Soc. Rev.*, 2015, 44, 5148.
[35] H. Duan, D. Li, Y. Tang, Y. He, S. Ji, R. Wang, H. Lv, P. P. Lopes, A. P. Paulikas, H. Li, S. X. Mao, C. Wang, N. M. Markovic, J. Li, V. R. Stamenkovic, Y. Li, *J. Am. Chem. Soc.*, 2017, 139, 5494.
[36] D. M. F. Santos, C. A. C. Sequeira, J. L. Figueiredo, *Química Nova*, 2013, 36, 1176.
[37] X. Chen, S. Shen, L. Guo, S.S. Mao, *Chem. Rev.*, 2010, 110, 6503-6570.
[38] J. Li, N. Wu, *Catal. Sci. Technol.*, 2015, 5, 1360-1384.
[39] R. Singh, S. Dutta, *Fuel*, 2018, 220, 607-620.

[40] H. Ahmad, S. K. Kamarudin, L. J. Minggu, M. Kassim, *Renew. Sustain. Energy Rev.*, 2015, 43, 599-610.

[41] C. Acar, I. Dincer, F. Naterer Greg, *Int. J. Energy Res.*, 2016, 40, 1449-1473.

[42] A. Mezni, A. Mlayah, V. Serin, L. S. Smiri, *Mater. Chem. Phys.*, 2014, 147, 496-503.

[43] G. L. Chiarello, E. Selli, L. Forni, *Appl. Catal. B Environ.*, 2008, 84, 332-339.

[44] B. P. Khanal, A. Pandey, L. Li, Q. Lin, W. K. Bae, H. Luo, V. I. Klimov, J. M. Pietryga, *ACS Nano*, 2012, 6, 3832-3840.

[45] Y. Lee, E. Kim, Y. Park, J. Kim, W. Ryu, J. Rho, K. Kim, *J. Materiomics*, 2018, 1-12.

[46] G. Hippargi, P. R. Maddigapu, N. Labhsetwar, S. Rayalu, *Russ. J. Phys. Chem. B*, 11 2017, 6, 1002-1011.

[47] N. Y. Mostafa, Z. K. Heiba, M. M. Ibrahim, *J. Mol. Struct.*, 2015, 1079, 480-485.

[48] G. A. M. Mersal, N. Y. Mostafa, A. E. H. Omar, *Mater. Res. Express*, 2017, 4, 85031.

[49] R. Michal, S. Sfaelou, P. Lianos, *Molecules*, 2014, 19, 19732-19750.

[50] Z. K. Heiba, M. B. Mohamed, N. G. Imam, N. Y. Mostafa, *Colloid Polym. Sci.*, 2016, 294, 357-365.

[51] J. Wang, F. Xu, H. Jin, Y. Chen, Y. Wang, *Adv. Mater.*, 2017, 29.

[52] K. G. dos Santos, C. T. Eckert, E. De Rossi, R. A. Bariccatti, E. P. Frigo, C. A. Lindino, H. J. Alves, *Renewable Sustainable Energy Rev.*, 2017, 68, 563.

[53] Y. Li, L. Wang, A. Song, M. Xia, Z. Li, G. Shao, *Electrochimica Acta*, 2018, 268, 268-275.

[54] C. R. Rajamathi, U. Gupta, N. Kumar, H. Yang, Y. Sun, V. Suss, C. Shekhar, M. Schmidt, H. Blumtritt, P. Werner, B. Yan, S. Parkin, C. Felser, C. N. R. Rao, *Adv. Mater.*, 2017, 29, 1606202.

Chapter 2

Literature Review

2.1 Transition metal dichalcogenides

Transition metal dichalcogenides (TMDCs) are 2D layered materials that can be represented by MX_2, where M is a group IV-IX transition metal (typically Mo, W, V, Re, Nb, Ta, or Ti) and X is a chalcogen atom (S, Se, or Te) [1]. The M atoms are sandwiched between two X atoms to give X-M-X. Covalent bonding exists between M and X atoms, whereas weak van der Waals forces exist between the stacked layers [1]. Bulk TMDCs can form in different crystal phases, with two main heterogeneous polymorphic structures such as the octahedral coordination phase (T) and the trigonal prismatic phase (H) [2]. Fig.1 illustrated a simple ball-and-stick atomic model of the polymorphic structures. Within the H phase for hexagonal symmetry, the six atoms are arranged similarly in the upper and lower tetrahedrons, with the M atoms as a symmetrical point. The 2H and 3R phases result from the sequential stacking of the 1H layer. The 2H phase consists of two layers with AB stacking exhibiting a hexagonal symmetry (point group D_{3h}), whereas the 3R consists of three layers with ABC stacking exhibiting a rhombohedral symmetry (point group C_{3v}). The T phase is formed due to twisting the upper (or lower) tetrahedron by 180 ℃ and is characterised by the tetragonal symmetry (point group D_{2d}). The 1T phase has metallic properties, whereas the 2H phase has semiconductor properties (e.g. MoS_2 and WS_2). The distorted octahedral phase (1T'), including the monoclinic (1T') and orthorhombic (T_d) structures, can also be observed with semi-metallic properties (e.g. VSe_2) [1-3]. Moreover, a low-temperature phenomenon results in TMDCs having superconductivity properties (e.g. $NbSe_2$ and TaS_2) [4-6]. The 2H phase is usually thermodynamically favoured [7]. However, some TMDC family members crystallise naturally into the 1T or 1T' phase [8]. The 2H phase can be converted into the 1T phase through a popular method which involves solution phase intercalation. Bulk TMDCs can be exfoliated into 2D atomic crystals like graphite [4-6]. The resultant 2D atomic crystals have exciting properties due to the effects of quantum confinement [4-6]. For example, if the bulk material has an indirect band gap, the 2D atomic crystals will have a direct band gap [9, 10].

(a) Trigonal Prismatic	2H		3R
	Semiconductor (group VIB) (MoS_2, WS_2, …)	Metallic (group VB) (TaS_2, $TaSe_2$, NbS_2,…)	Metallic (group VB) (TaS_2, NbS_2…)
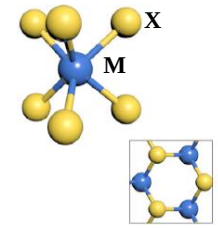	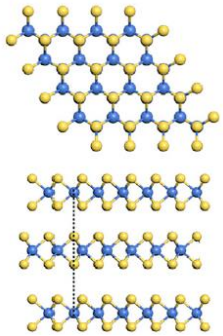	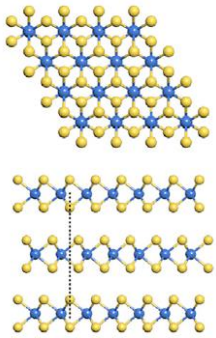	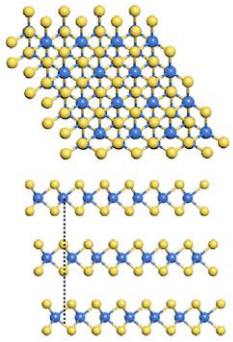

(b) Octahedral	1T	1T'	T_d
	Metallic (group VB, VIB) (TaS_2, NbS_2, MoS_2, WS_2,)	Metallic (group VIB) ($MoTe_2$)	Metallic (group VIB) (WTe_2)
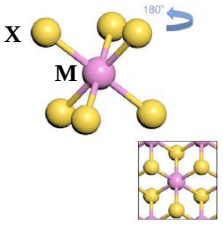	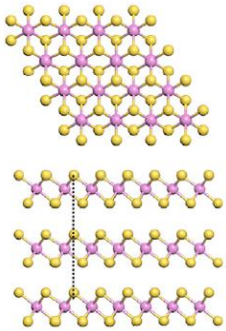	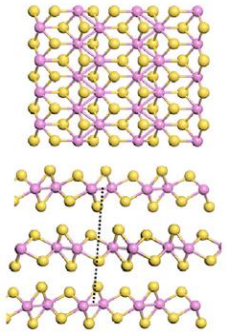	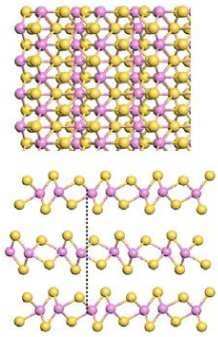

Fig. 1: (a) Trigonal prismatic and (b) Octahedral phase.

2.2 Electronic structure of TMDCs

The electronic structure and structural stability of TMDCs are mainly influenced by d electron counts of the transition metal [2, 11]. Fig. 2a shows the H-TMDCs phase transition metal d-orbitals are divided onto three degenerated states d_{z_2}, $d_{x_2-y_2,xy}$, and $d_{xz,yz}$ with a large energy gap of ~ 1 eV between d_{z_2} and $d_{x_2-y_2,xy}$ orbitals [2]. However, Fig. 2b shows the T-TMDCs phase result in d_{z_2,x_2-y_2}(e.g.) and $d_{xy,yz,xz}$ (t_{2g}) crystal field. The oxidation state of the TMDC transition metal is +4; therefore, the orbitals are filled from 0 (d_0, transition metal group IVB) to 6 (d_6, transition metal group VIIIB) electrons. In the T-TMDC phase, the t_{2g} levels are between the d_{z_2} and $d_{x_2-y_2,xy}$ levels of the H-TMDC phase. In the TMDCs with a semiconductor and metallic nature, the d-orbitals are all occupied and partially occupied, respectively. Under ambient conditions, two electrons in group VIB TMDCs are inclined to fill

the dz_2 level (2H phase) with preference over the t2g levels (1T phase) due to lower energy required. The stable semiconductor 2H phase is thermodynamically favoured over the metastable metallic 1T phase, except for WTe_2 (Td phase) [2]. Fig. 2c illustrates that the 1T' phase has even lower ground-state energy than the 1T phase without mechanical stress [12-14]. As such, introducing structural distortions by mechanical stress or injecting an electron has received extensive interest in improving the structural stability of group VIB TMDCs. The 2H and 1T phases with group VB TMDCs are stable due to the energy difference between the two phases being less than 0.1 eV [2]. Their d-orbitals are partially filled with additional electrons irrespective of the crystal field. As such, they are always metallic (2H and 1T phase of group VB TMDCs). Recent studies have shown that TMDCs containing group VB transition metals extended to four structures as 2H, 3R, 1T, and 1T' [2, 15-18].

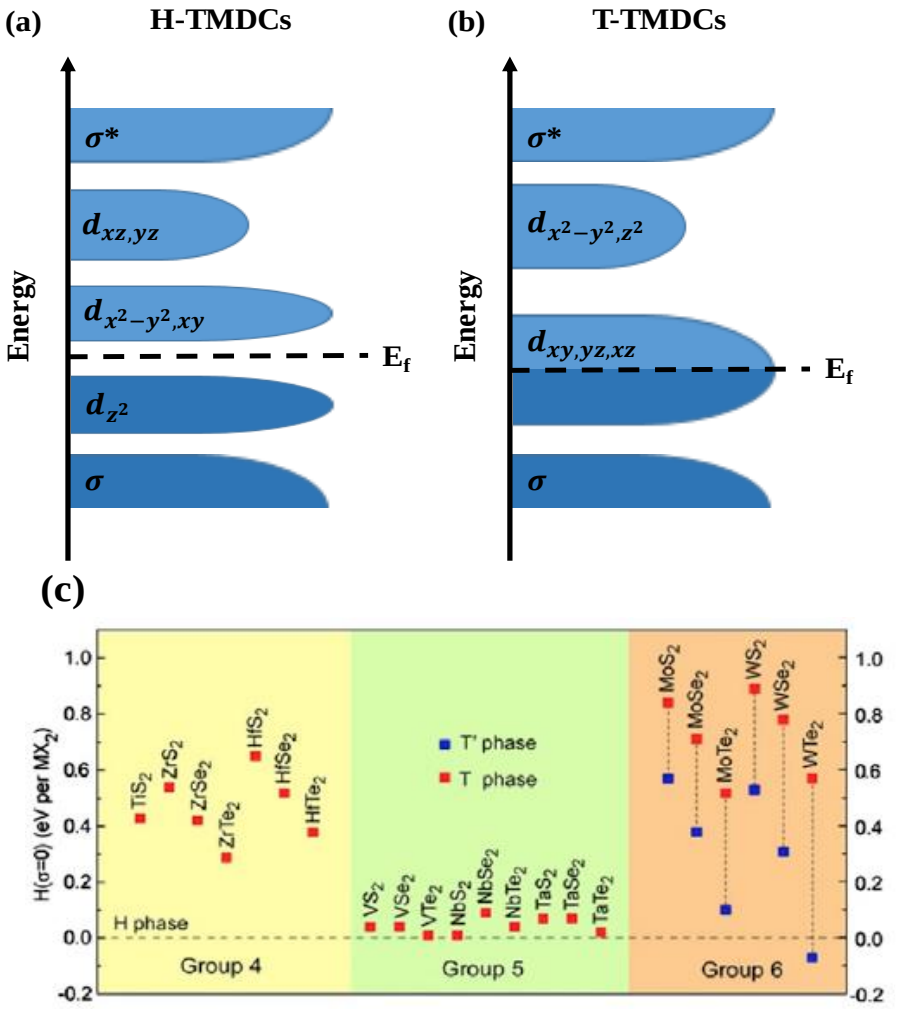

Fig. 2: An illustration of the d orbital filling of (a) H- and (b) T-phases, (c) energy differences between monolayer TMDC phases without mechanical stress.

2.3 Synthetic techniques used to synthesise transition metal dichalcogenides

Without a doubt, synthesising TMDCs with high crystallinity, uniform thickness, large domain size, and continuity is very critical not only to manipulate the electronic structure of the material but also to investigate their catalytic and unique physical properties (charge density wave (CDW), superconductivity, and ferromagnetism) [19, 20]. Generally, two main synthetic techniques are used to synthesise TMDCs: hydrothermal/solvothermal and chemical vapour deposition [1]. Other techniques include liquid exfoliation and colloidal synthesis methods. The methods are discussed in this section.

2.3.1 Top-down approach

2.3.1.1 Liquid exfoliation synthesis

Liquid exfoliation is a synthetic technique that uses foreign substances such as ions, inorganic and organic molecules, and metal nanoparticles to weaken the van der Waal forces between the bulk TMDC material layers to produce single or few layered TMDC material [21, 22]. Two processes are used to conduct the liquid exfoliation technique: intercalation and chemical exfoliation. Fig. 3a shows the intercalation process, which involves introducing charged ions, such as Li^+, between the layers of the bulk TMDC material to weaken the van der Waal forces [22]. The intercalation process results in maintained individual sheets [22]. Fig. 3b illustrates the chemical process of using ultrasound waves (sonication) to separate the bulk TMDC, in a suitable solvent, into individual or few-layered TMDC material. The advantage of using the liquid exfoliation synthesis process is accessibility to doping with various species, tuneable properties, and it is a controlled process, ease of operation, and results in high yield [23-26]. The challenge is controlling the lateral size and producing a high yield of the individual layers [21, 22, 27, 28].

Moreover, intercalation using Li^+ may result in by-products such as Li_2X (where X = S, Se, or Te) if the process is not strictly controlled and the processes can take a long time to complete [21, 22, 29]. To produce TMDCs at a large-scale, Coleman *et al.* designed a shear-exfoliation method using an aqueous surfactant and a kitchen blender to produce MoS_2 nanosheets [30]. Coleman *et al.* discovered that the nanosheets' dimensions depended on the concentration of MoS_2, mixing time, volume, and rotation speed. As such, they could control the dimensions of the nanosheets by using the optimal conditions, resulting in lateral sizes of the nanosheets between 40-220 nm and layer thickness between 2-12 layers. The shear-exfoliation method has

produced other TMDCs, such as WS_2 [30]. Moreover, they produced 1.3 mg/min of product. As such, making this process an excellent method for large-scale production.

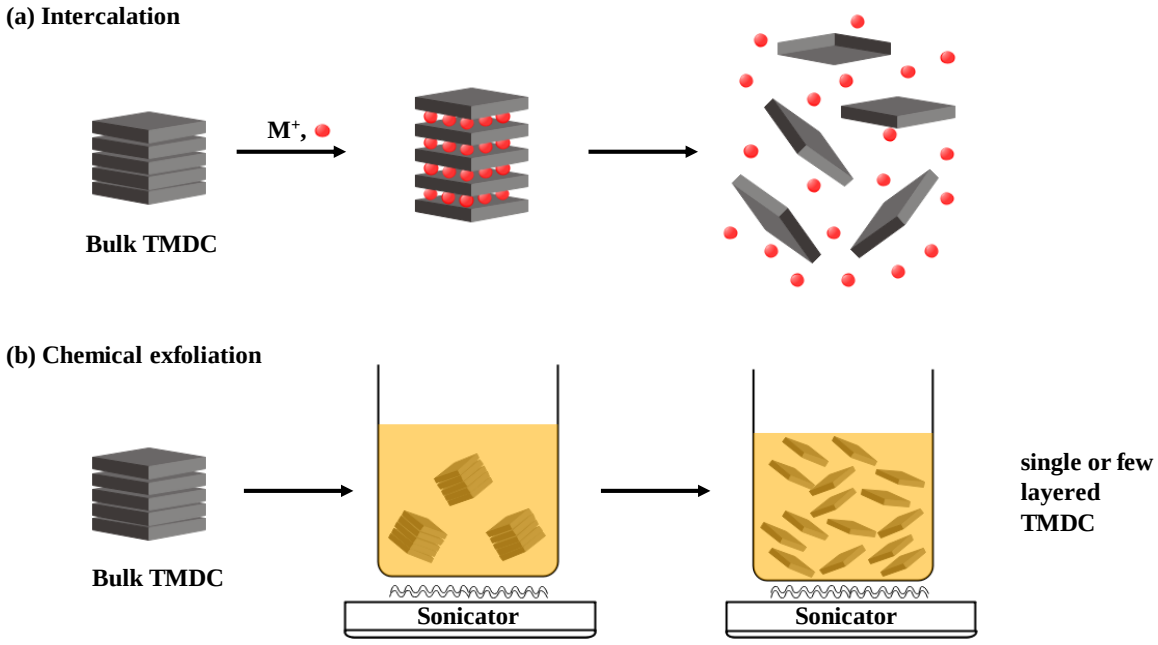

Fig. 3: Schematic diagrams of the liquid exfoliation synthetic techniques (a) intercalation and (b) chemical exfoliation.

2.3.2 Bottom-up approach

2.3.2.1 Chemical vapour deposition

The chemical vapour deposition (CVD) technique involves the sulfurisation or selenisation of the metal (e.g. Mo) or metal oxide (e.g. WO_3) in a furnace to produce 2D TMDCs with large surface areas [1]. CVD has produced high-quality, low-defect, ultrathin epitaxial TMDCs films on different substrates [31-35]. Fig. 4 shows a schematic diagram of the CVD synthetic technique. CVD suits vertically aligned TMDCs and Janus structures [36, 37]. The advantage of using CVD is the ability to form TMDCs and TMDC-based hybrids such as MoS_2 and $MoS_2/ReSe_2$, as well as the resultant of good adherence to different substrates [31, 38]. Kheng *et al.* synthesised MoS_2 and WS_2 wafer-thin films using the metal-organic CVD synthetic technique [39]. Kheng *et al.* used MC_6O_6 (where M = Mo or W; metal hexacarbonyl) as the metal source and C_2H_6S (dimethyl sulfide) as the S source. The challenge with the metal-organic CVD process was carbon contamination due to using dimethyl sulfide as a precursor [39].

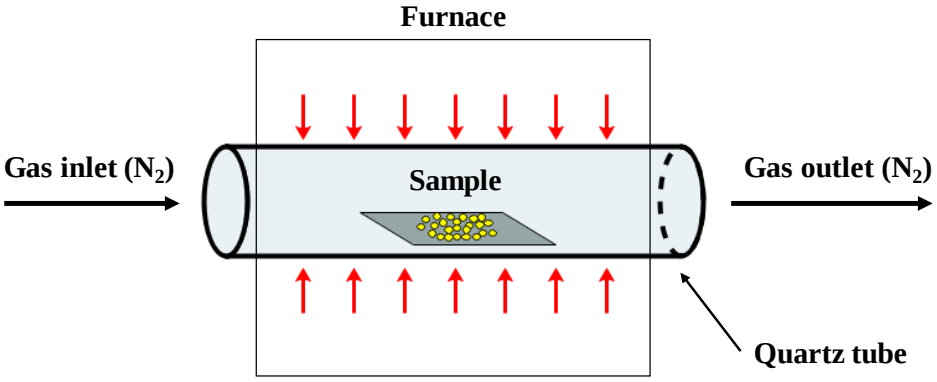

Fig. 4: Schematic diagram of CVD synthetic technique.

2.3.2.2 Hydrothermal synthesis

Hydrothermal synthesis is a straightforward synthesis that uses H_2O as a solvent, where precursors are added and autoclaved at low temperatures [1]. Fig. 5 shows a schematic diagram of the hydrothermal synthesis technique. The hydrothermal synthesis technique has been used to form nanomaterials with various morphologies, such as nanoflowers, nanoflakes, nanoplates, nanoparticles and quantum dots [40-43]. Furthermore, hydrothermal synthesis is suited to form 2D TMDC-base composites or hybrids, where the TMDC is combined with another conducting material, such as carbon nanofibers, transition metal nanoparticles, and graphene [44-46]. Fan *et al.* were among the first researchers to successfully synthesise crystalline MoS_2 and $MoSe_2$ nanomaterials using the synthetic hydrothermal process [47]. Fan *et al.* used Na_2MoO_4 as a Mo precursor and NaS_2O_3 as an S precursor, and $NaSeO_3$ as a Se precursor to produce amorphous MoS_2 and $MoSe_2$ with a size of 4 and 7nm, respectively. The amorphous nanomaterials were annealed at 350 ℃ to produce crystalline 2H-MoS_2 and 2H-MoS_2 [47]. Sakthivel *et al.* made Ni-doped $MoSe_2$ nanoplates by dissolving Na_2MoO_4 and $Ni(NO_3)_2$ in water [48]. The selenium precursor and hydrazine (reducing agent) were added dropwise into the water mixture, followed by adding the mixture into the autoclave and maintained at 180 ℃ for 12 h [48]. The advantage of using the hydrothermal synthesis technique is the usage of low temperatures; it is economical, suitable for large scales, and environmentally friendly because of the use of H_2O as a solvent [1]. The disadvantage stems from the lack of solubility of some precursors in H_2O.

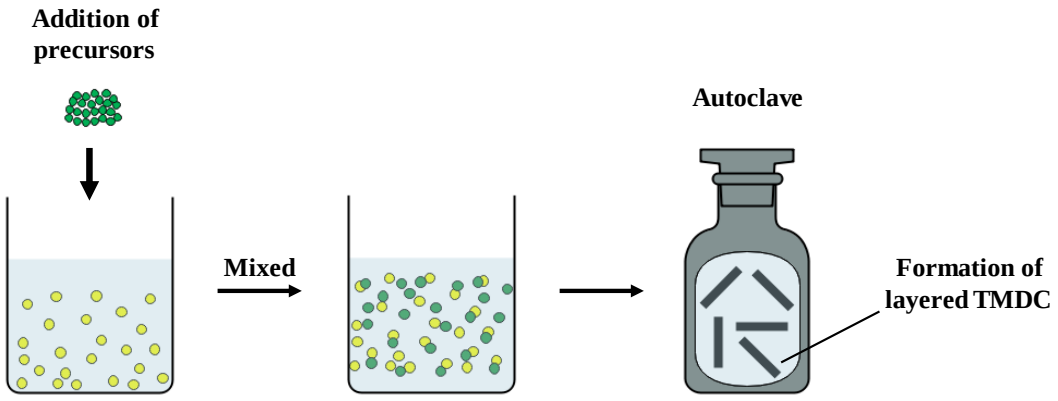

Fig. 5: Schematic diagram of the synthetic hydrothermal technique.

2.3.2.3 Solvothermal synthesis

Solvothermal synthesis is similar to hydrothermal synthesis; organic solvents are used instead of using H_2O as a solvent [1]. Organic solvents assist with the precursors or intermediates' viscosity, solubility, and polarity issues [1]. Instead of an autoclave, a reflux technique can also be used at temperatures between 150 and 320 ℃ under nitrogen flow (shown in Fig. 6) [49]. The solvothermal synthesis technique's advantage is the organic solvents; using organic solvents tunes the properties of the nanomaterials, including shape, size, efficiency, and fast and straightforward approach [1]. The disadvantage is that polar precursors will not dissolve in organic solvents. Colloidal synthesis is another type of solvothermal technique and is discussed below.

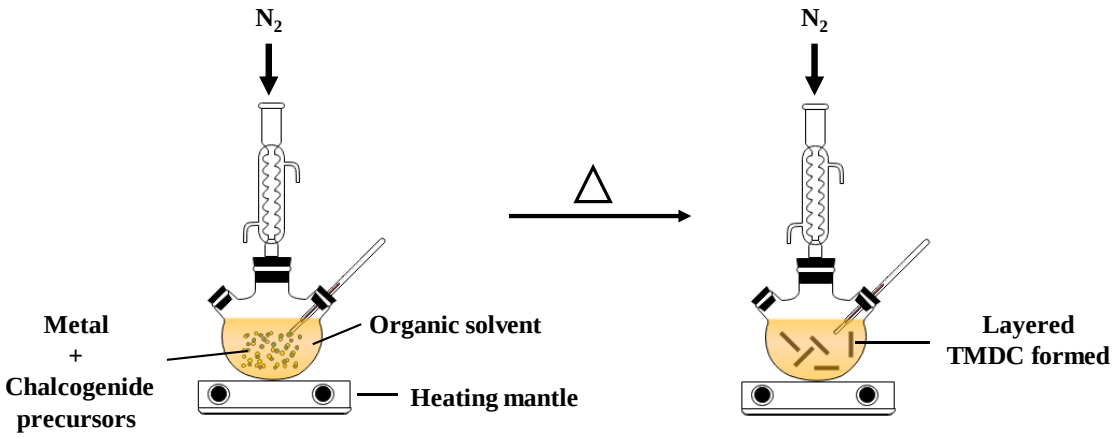

Fig. 6: Schematic diagram of the solvothermal synthetic technique set-up.

2.3.2.4 Colloidal synthesis

In the colloidal synthesis process, crystals or crystalline nanoclusters made up of a few 100-1000 atoms, commonly referred to as colloids, are formed [50, 51]. The atoms agglomerate to form colloids dispersed in a particular solvent [50, 51]. The colloidal synthesis technique uses different chemical processes, such as thermal deposition, chemical reduction, and sol-gel, to produce atoms needed to form colloids from different precursors. The thermal decomposition chemical process is a popular process that uses organometallic precursors decomposed in organic solvents at elevated temperatures [50]. In 1986, Chestoney *et al.* were among the first researchers to use this synthetic process to form crystalline group II-VI semiconductor nanocrystals [51]. The major challenge with using the thermal decomposition process stems from identifying and controlling the kinetics of the different precursors that would lead to precipitation and the nucleation and growth process [51]. In the 1950s, LaMar and Dinger developed theoretical principles for the nucleation and growth of nanocrystals which can be used to understand the mechanism of thermal decomposition synthesis [52, 53]. The theory suggests that a burst of nucleation after supersaturation forms many nuclei of the same size, known as homogenous nucleation. Growth of the nuclei occurs without new nuclei being formed. The process is described in three steps: (i) decomposition of the precursor results in an increase in monomer concentration until the solution reaches critical supersaturation (Cs), (ii) saturation will continue to increase until Cmin level, where a burst of nucleation occurs due to the nucleation energy barrier being overcome; (iii) a drastic drop of monomer concentration and supersaturation level occurs due to the burst of nucleation, and eventually, the nucleation process stops. At this point, nuclei begin to grow from the diffusion of the monomers to the nucleation site [52, 53]. The theory is only relevant to monodispersed nanocrystal processes [54, 55]. The growth process can be described as Ostwald ripening, where the smaller particles dissolve back into the solvent because of their high solubility and surface energy (thermodynamically unstable), which allows further growth of the larger particles [56]. Therefore, the molecules in small particles will detach themselves and migrate into the solution to attach themselves to larger particles. This process will continue until the overall resultant nanocrystals are of a large size average [56]. The burst in nucleation is a very crucial step [57].

The heat-up colloidal synthesis technique used in this study involves the addition of the metal and chalcogenide precursors in an organic solvent in a three-neck round-bottomed flask attached to a Schlenk line. The mixture is degassed with N_2 and heated to the desired temperature. The organic solvent can also act as a reducing agent, where the Se precursor is

reduced into a 2- charged monomer and reacts with the dissolved metal. The resultant TMDC nanomaterials are washed with organic solvents (e.g. Hexane), centrifuged, and dried. This synthetic method controls the nanomaterials' size, morphology, and phase [57-60]. The structural properties of the nanomaterials are controlled by varying the reaction parameters, such as temperature, type of precursor, solvent or surfactant, and the ratio of the precursors used. The effect of the reaction parameters is discussed below:

(i) Effect of the precursors:

Colloidal synthesis depends on the type of precursors used because it relies on forming the free monomer to begin the nucleation and growth process. The size and shape of the resultant nanomaterials depend on how fast the monomer is available and how fast the monomer reacts to begin the nucleation process [61, 62]. Thermal decomposition takes place through the heating of the precursors to release the required monomer [61, 62]. Usually, a metal salt or a metal complex is used in this method. The ligands on the metal in the metal precursor determine the rate of decomposition and formation of the reactive metal monomer.

(ii) Effect of temperature:

Temperature affects the rate of decomposition of the metal precursor. The quicker the metal precursor decomposes, the faster the monomer formed reacts, and the nucleation and growth process occurs [63, 64]. The temperature of the reaction affects the kinetics of the nanocrystal growth and the ligands which control the shape of the nanocrystals.

(iii) Effect of the capping agents (organic solvents):

The organic solvents act as capping agents that bind to the surface of the nanoparticles to stabilise nanoparticles and prevent agglomeration and oxidation on the surface of the nanoparticles [65-67]. The capping agents also control the shape and size of the nanoparticles. Colloidal synthesis can be scaled-up; commercial companies such as Nanosys and Nanoco have produced quantum dots and other nanostructures using modified colloidal synthesis at a large scale [68, 69]. Recently, Nanoco has released patents on the synthesis of TMDCs which sparks commercial interest in producing TMDCs using this process [68, 69].

2.2 Electrochemical water-splitting technique

For over a century, the energy demand has been met using non-renewable sources such as fossil fuels [70]. These sources have provided up to 80% of our energy for houses, cars, and industry [70-74]. However, these non-renewable sources are not abundant, and the pollution that comes with using them will have a long-lasting negative effect on the environment [75, 76]. As such, research has pointed to alternative sustainable renewable energy sources to reduce these harmful effects. Hydrogen is a viable alternative to fossil fuels as an energy carrier because it is the most abundant element, has an extremely high energy density, and is non-toxic [77-79]. Hydrogen energy is molecular hydrogen from compounds containing hydrogen to produce energy that can power our cars, houses, and industry. Hydrogen produces water as a by-product when it reacts with oxygen from the air (eq. 1) [77-79].

$$H_2(g) + \frac{1}{2}O_2(g) \rightarrow H_2O(l) \qquad (\Delta H = -286.0\ kJ/mol) \quad \text{(eq. 1)}$$

Eq. 1 illustrates that to generate 286.8 kJ energy, 0.5 mol of oxygen has to react with 1 mol of hydrogen [79]. Therefore, the mass hydrogen energy density would be 143 kJ/g (energy = 286.0 kJ/mol * 0.5 mol/g = 143 kJ/g), the highest energy density relative to fossil fuels [80]. Currently, steam methane reforming and gasification of petroleum coke and coal methods are used to produce hydrogen gas at a large scale. However, these methods use high temperatures and produce greenhouse gases as by-products making them less desirable technologies for the production of hydrogen [80]. Recently, a clean and efficient technology such as water-splitting has become of interest in the production of hydrogen gas [81, 82]. Fig. 7 shows the water-splitting technique, which involves decomposing water to form hydrogen and oxygen with an external current [81, 82]. This technique is merely a thermodynamically assisted uphill strategy where electricity is used as a primary source [83]. The area of interest in this study is the HER compartment.

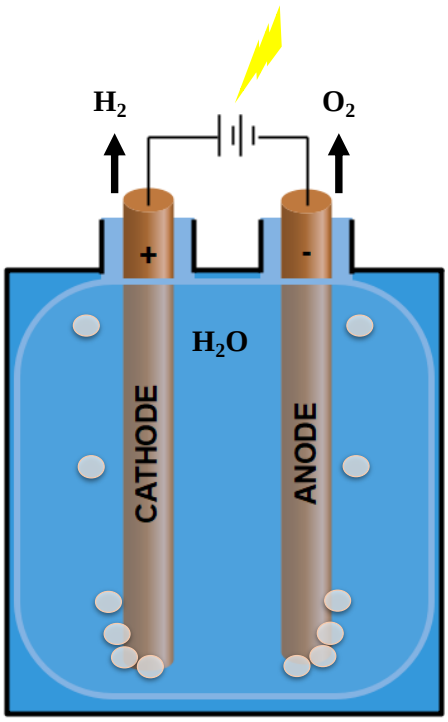

Fig. 7: Water-splitting technique.

2.2.1 Operation of HER

The electrolysis of water is expressed by the endothermic reaction eq. 2 (also illustrated in Fig. above) below:

$$H_2O(l) \xrightarrow{electrolysis} H_2(g) + \frac{1}{2}O_2(g) \quad \Delta G^{\theta} = +237.2\ KJ \cdot mol^{-1}\ \ \Delta E^{\theta} = 1.23\ V \quad \text{(eq. 2)}$$

The reaction consists of two half-reactions involving the HER and the oxygen evolution reaction (OER) processes [84-86]. The potentials of HER and OER are 0 V and 1.23 V, respectively, versus the reversible hydrogen electrode (RHE) at standard conditions (298.15 K and 1atm). The main focus of this study is the HER, whose response differs depending on the solution used:

In an acidic solution: $2H_3O^+(aq) + 2e^- \rightarrow H_2(g) + 2H_2O(l)$ (eq. 3)

In an alkaline solution: $2H_2O(l) + 2e^- \rightarrow H_2(g) + 2OH^-(aq)$ (eq. 4)

In this study, the focus will be on an alkaline solution. The adsorption energy of the catalyst plays a crucial role in determining the conversion efficiency and stability in an electrolyte solution [87-89]. According to theoretical studies, the activity trends of electrocatalysts in an acidic medium are concluded based on hydrogen adsorption (H_{ad}) at the active sites. However, in an alkaline medium, it is controlled by a balance of three critical reactions: (i) the H_{ad} on the surface of the catalyst, (ii) the prevention of hydroxyl group adsorption (OH_{ad}) because they poison the active sites, and (iii) energy needed to dissociate the H_2O molecules [90-93]. The issue of poor reaction kinetics and stability can be resolved by tuning the surface chemistry by modifying the electronic structure, composition, morphology, and porosity/active surface area [94]. HER is challenging to achieve at low overpotentials in an alkaline medium [95]. Extra energy is required to produce the protons by breaking the H_2O molecule, consequently influencing the overall reactions [87, 96, 97].

In the mechanism of HER under alkaline conditions, hydrogen is the only product, but the reaction is a multi-step reaction that involves three processes (adsorption, reduction, and desorption) [98-102]. The overall HER is made up of three steps (also illustrated in Fig. 8):

1. Volmer reaction: This involves hydrogen adsorption onto the electrode's surface. The electrochemical adsorption process is expressed by eq. 5 [99-102]:

$$H_2O(l) + e^- \xrightarrow{A} H_{ads} + OH^-(aq) \qquad \text{(eq. 5)}$$

   In this step, the Tafel slope (b_1) which gives important reference to the reaction mechanism, can be obtained by eq. 6:

$$b_1 = \frac{2.3\,RT}{\propto F} \qquad \text{(eq. 6)}$$

   R is the ideal gas constant, T is the absolute temperature, $\propto$ the symmetry coefficient with a value of 0.5, and F is the Faraday constant [84, 103-106]. At 25 ℃ b_1 = 118 mV/dec [99, 100].
2. Heyrovsky reaction: The electrochemical desorption process is expressed by eq.7:

$$H_{ads} + H_2O(l) + e^- \xrightarrow{A} H_2 + OH^-(aq) \qquad \text{(eq. 7)}$$

In this step, the Tafel slope (b_2) can be obtained by eq. 8:

$$b_2 = \frac{2.3\ RT}{(\propto +1)F} \qquad \text{(eq. 8)}$$

At 25 ℃ b_2 = 39 mV/dec. However, this reaction can occur in a different direction where two hydrogen atoms (H_{ads}) adsorbed onto the surface of the electrode combine to form a single hydrogen molecule. This electrochemical desorption process is expressed by eq. 9 (Tafel reaction) [99, 100]:

$$2H_{ads} \xrightarrow{A} H_2 \qquad \text{(eq. 9)}$$

The Tafel slope (b'_2) can be obtained by eq. 10:

$$b'_2 = \frac{2.3\ RT}{2F} \qquad \text{(eq. 10)}$$

At 25 ℃, b'_2 = 29 mV/dec.

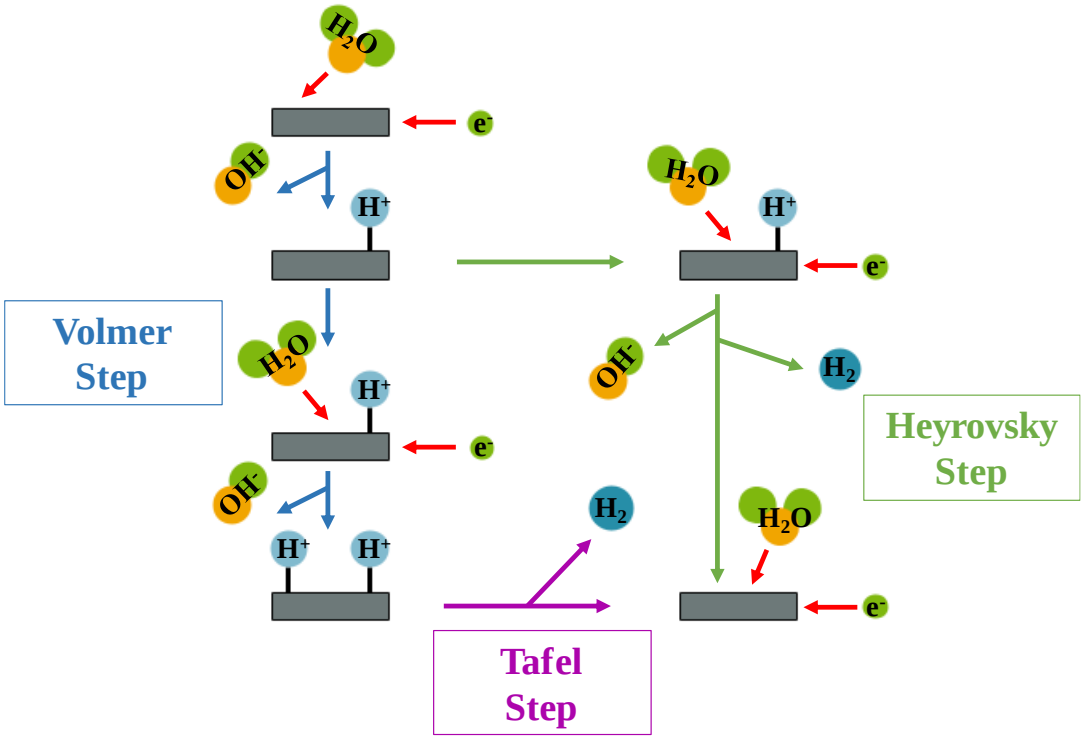

Fig. 8: Illustration of the HER mechanism under alkaline conditions with the Volmer reaction (blue), Heyrovsky reaction (green), and Tafel reaction (purple).

HER tests are performed using a three-electrode electrolytic tank consisting of the working electrode, a counter-electrode, a reference electrode, and a gas entrance [84]. These three steps are related to the electrode surface's inherent electronic and chemical properties [101]. As such, the Tafel slopes obtained from the polarisation curves can be used to determine which of these steps is the rate-controlling step [101]. A few details need to be considered and understood during these tests discussed below.

2.2.2 Overpotential

Overpotential is the additional potential required to drive a reaction at a specific rate beyond the thermodynamic requirement [84]. The intrinsic parameter used to evaluate the performance of the electrocatalyst is the onset potential which is ~ 0 V for Pt. The quantitative activity parameter used to assess the activity of the electrocatalyst is the overpotential at a fixed current density, typically 10 mA/cm^2 [84]. In some cases, the overpotentials at high current densities (e.g. 50, 100, and even 1000 mA/cm^2) are used as other activity parameters for high-performance electrocatalysts [107, 108]. The absolute overpotential is the difference between the standard hydrogen electrode (SHE) and the onset potential initiating the HER by an electrocatalyst. The SHE is the standard reference point for eq. 2, where the potential E^{θ} = 0.000 V at all temperatures and 1 atm hydrogen pressure. During the test, the hydrogen pressure influences the overpotential as indicated by the Nernst eq. (eq. 11):

$$E = E^{\theta} + \frac{RT}{R} ln \frac{[H^+]}{\sqrt{P_{H_2}}} \qquad \text{(eq. 11)}$$

To maintain equilibrium potential at the standard value (0 V versus RHE), H_2 gas should be introduced to maintain saturation of the gas [109, 110]. According to the origins of the polarisation of electrodes, the overpotential can be divided into three overpotentials: activation, concentration, and resistance [98]. The activation overpotential, which is the intrinsic property of the material, can be lowered by using modified electrocatalysts [98]. This concept was proven by Lukoski *et al.,* where at a current density of 10 mV/cm^2 on MoS_2, the overpotential was lowered from -320 mV to -187 mV after changing from the 2H-MoS_2 phase to 1T-MoS_2 phase [111]. The concentration overpotential can only be reduced to a certain extent by an

external force (such as stirring) because it derives from the concentration difference between the ions involved due to the slow ion diffusion rate and the fact that there is an existing diffusion layer. However, stirring may disturb the related reactions [111]. The resistance overpotential, also known as the junction potential, is the potential drop caused by the Ohmic resistance (R_Ω, also includes both the contact and solution resistances). It needs to be corrected to attain the real potential applied on the electrocatalyst by using the iR_Ω compensation method to effectively eliminate the resistance overpotential, expressed by eq. 12:

$$E_{corrected} = E_{measured} - iR_\Omega \quad \text{(eq. 12)}$$

Where $E_{measured}$ is the potential measured against RHE, i is the current measured without the background correction, and R_Ω uncompensated resistance, which can be measured by using electrochemical impedance spectroscopy. All potential measurements should be normalised to RHE for convenience [84, 111].

2.2.3 The electron of the reference- and counter-electrodes

The overpotential of the working electrode (electrocatalyst) is not directly measured, it is the difference between the potential of the reference and working electrodes [84]. Therefore, the choice of the reference electrode is crucial as the electrode should have a stable and well-defined potential for accurately measuring and regulating the potential applied to the working electrode in the solution. The most commonly used electrodes are, firstly, the saturated calomel electrode (SCE) which follows the reversible redox reaction (eq. 13):

$$Hg_2Cl_2 + 2e^- \leftrightarrow 2Hg + 2Cl^- \quad \text{(eq. 13)}$$

In KCl solution with saturated concentration. Secondly is the silver-silver chloride (Ag/AgCl) electrode, which follows the reversible redox reaction (eq. 14):

$$AgCl + e^- \leftrightarrow Ag + Cl^- \quad \text{(eq. 14)}$$

In a KCl solution at a specific concentration. The reference electrode is equipped with a double junction or salt bridge to separate it from the working electrode so that the potential is stable and fixed and minimises junction resistance. The counter-electrode (also known as the auxiliary

electrode) accepts electrons from the solution species and forms a current loop with the working electrode that must sustain high current and stability without interrupting the HER of the working electrode. The Pt electrodes (Pt wire, Pt plate, and Pt meshes) are the most commonly used as they can provide a large current for HER by acquiring electrons from the solution to reduce H_3O^+/H_2O at the working electrode. However, Pt electrodes are known to dissolve in certain acidic/basic solutions, which disturbs the activity of the working electrode [110-113]. Especially when using non-metal electrocatalysts, by using a minimal amount of Pt deposited onto the GC electrode, their activity may be primarily enhanced, leading to misleading results. Thus, it has been suggested that using carbon electrodes (such as graphite rod) is a more feasible choice than Pt electrodes. The carbon electrode should be very pure, or it may leach into the solution, thus affecting the activity of the working electrode. Furthermore, finally, the placement of the counter-electrode relative to the working electrode should be in such a way that a homogenous electric field is created to ensure the stability of the HER [84].

2.2.4 Polarisation curves

The polarisation curves for electrocatalysts are obtained using linear sweep voltammetry (LSV), which are presented by plotting current density versus potential [84]. The activity of a catalyst is better when the same current density presents at a lower potential, or the higher current density is at the same potential in a polarisation curve. This concept was proven by Voiry *et al.*, who reported that the 1T-MoS_2 phase had higher catalytic activity than a 2H-MoS_2 phase due to lower onset potential at the same current density [114]. The onset potential and overpotential are measured by using the LSV, shown in Fig. 9.

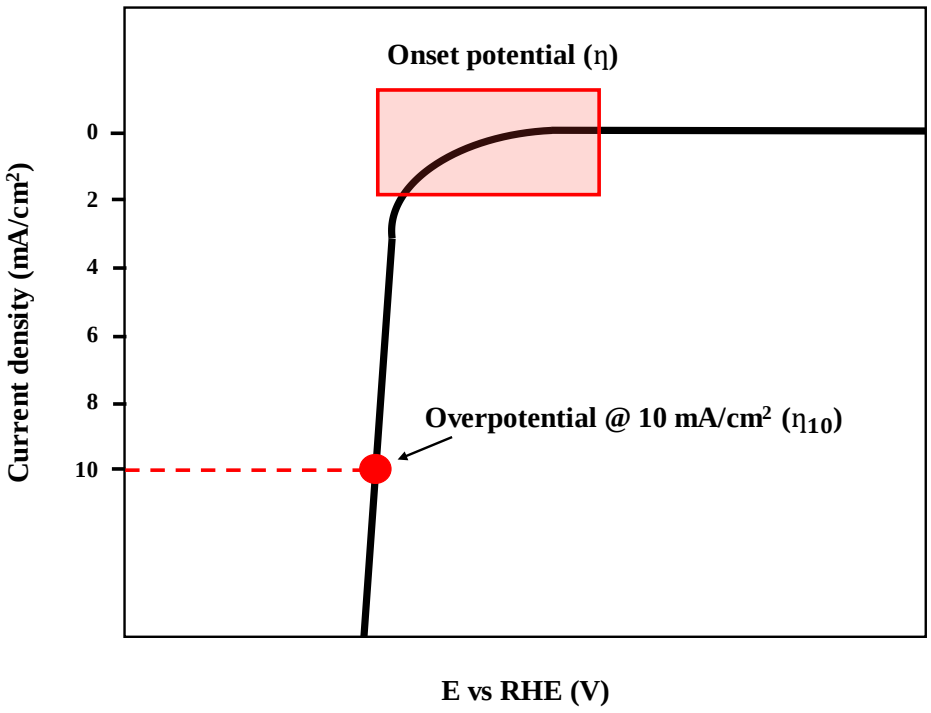

Fig. 9: Illustration of a typical LSV polarisation curve.

2.2.5 Tafel slope

The Tafel plot is obtained by replotting the polarisation curve where the overpotential is plotted against the log(current density). In processing the data, the Tafel slopes (b) are fitted by estimating a linear region of these slopes as expressed in eq. 15:

$$\eta = blog\frac{j}{j_0} \qquad \text{(eq. 15)}$$

where η is the overpotential, j is the current density, and j_0 is the exchange current density. Fig. 10 illustrates the Tafel plot, where the Tafel slope and exchange current density (j_0) is calculated. Therefore, the smaller the value of the Tafel slope, the faster the charge transfer kinetics because the lower applied potential is required to obtain the same current density. Voiry *et al.* obtained results that are in agreement with this theory, where the 1T-MoS_2 phase (40 mV/dec) had a lower Tafel slope value compared to the 2H-MoS_2 phase (75 mV/dec) due to faster charge transfer kinetics [114]. In section 2.5., two reactions could occur in the second step of the HER reaction: the Heyrovsky reaction (40 mV/dec) or the Tafel reaction (29 mV/dec). Therefore, the 1T-MoS_2 phase with a Tafel slope value of 40 mV/dec indicates that the Volmer-Heyrovsky mechanism dominates the HER, where the rate-determining step is the

electrochemical desorption reaction. However, since the Tafel slope plot is extracted from the polarisation curve, it may contain the contribution of the catalyst resistance, which depends highly on the electrocatalyst's conductivity and high mass loading. Hu *et al.* introduced another method for plotting the Tafel slopes using the impedance data by plotting log Rct (Rct is the charge transfer resistance obtained from Nyquist plots using the EIS method) versus overpotential. This avoids the catalytic resistance by reflecting on the charge transfer kinetics [114].

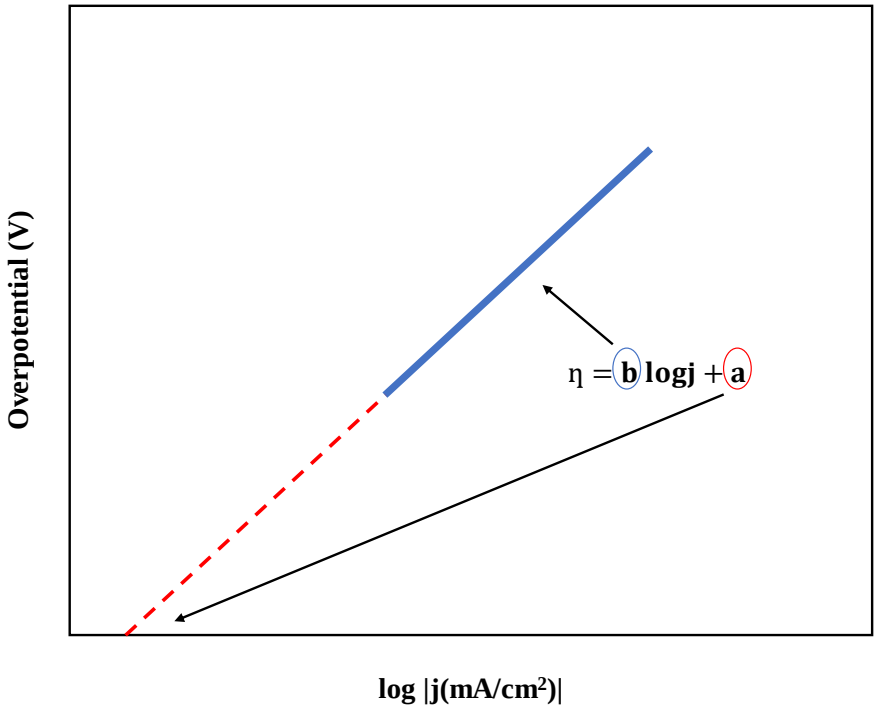

Fig. 10: Illustration of a Tafel plot.

2.2.6 Exchange current density

Exchange current density (j_0) is directly interrelated to the overpotential; as such, it can be considered an activity parameter. The value can be obtained by extrapolating the linear region, which is the current density when the overpotential is zero, calculated using eq. 14. Although measured at low scan rates, the exchange current density value may be higher than its actual value, especially when working with electrocatalysts with a high surface area [84].

2.2.7 Electrochemically active surface area

The surface area is the key parameter used to normalise the value of the current [84]. There are three types of surface area to normalise current for polarisation curves and the Tafel slopes plot: geometric surface area, Brunauer-Emmet-Teller (BET) surface area, and

electrochemically active surface area (ECSA). The geometric surface area is the surface area of the electrode (e.g. surface area of the glassy carbon electrode), and A/cm^2 denotes the units of the normalised current density. This method is widely used, but the current density could be an artificial effect, not representing the electrocatalyst's intrinsic catalytic properties [115]. Furthermore, the electrocatalyst's mass loading could significantly impact the applied potential; therefore, this method should only be used when the mass loading is a single layer with 100 % coverage. Thus, the geometric surface area method works well with planar electrodes (deposited thin films and foils). Two scenarios could occur if the mass loading is not optimum: low mass loading can lead to exposed static sites or high loading where only the surface layer of the electrocatalyst is involved in the HER. As such, electrode preparation and mass loading determine optimum results [84, 115].

The BET surface area method uses gas adsorption-desorption curves to normalise the current density. N_2 gas is used as the gas probe. This method best determines the porous or power-type electrocatalysts [84]. However, this method lacks accuracy because not all adsorption sites are electrocatalytically active; as such, not all intrinsic properties of the catalyst are represented [84, 116]. The ECSA method is generally accepted to measure the specific activity of electrocatalysts by employing the non-Faradic double-layer capacitance measured by the CV method in a selected non-Faradic potential region [84]. Previously in the literature, it has been discussed that determining the surface area is still a big challenge, especially when using non-metal electrocatalysts [110]. There could be inaccurate experimental results between different evaluation methods (the CV and EIS methods). Currently, the ex-situ BET method may be more accurate than the in situ electrochemical methods, which use the non-Faradic double-layer capacitance measurements [84, 110]. This method was used in this study.

2.2.8 Stability

Stability is another parameter that can be used to evaluate the performance of the electrocatalyst in the HER [84]. Two methods can be used to assess the stability of electrocatalysts: the CV method and the potentiostat or galvanostatic electrolysis method [99, 117]. The CV method involves running repeated potential cycles within a fixed potential range, including onset potential; for the electrocatalyst to be stable, there should be no change in the scans [117]. The potentiostat of the galvanostatic electrolysis method involves monitoring the variation in the value of current density or potential. Better stability is obtained when there is a smaller decline

in the value for current density or potential with increasing time at a fixed potential or current [118].

2.2.9 Enhancement of TMDC electrocatalytic activity to produce hydrogen

The performance of the 2D TMDC electrocatalysts depends on various crucial parameters such as atomic-level thickness plane, high surface area, edge effects, topological effects, short ion diffusion distance, improved restacking, efficient charge transfer, and abundant active sites [83, 119-132]. The metal and chalcogenide of the TMDCs will be exposed in the top position of the material, and the active sites are accessed easily by the electrolyte [83]. Bonde and Norskov *et al.* found that the reactive part of the MoS_2 TMDC is in the Mo and S edges, where the S edge has a higher G_{EH}* value [83, 133, 134]. It is known that the basal plane of TMDCs is inert. The large surface area of the TMDCs provides a perfect platform to combine with other nanomaterials to form super active nanocomposites.

Furthermore, introducing defects onto the surface, strain and different heteroatom, and doping the TMDC material to enhance and optimise electrocatalytic activity toward higher HER activity [135]. Although TMDCs electrocatalysts are excellent for HER, their electrocatalytic activity is still inferior to Pt-based electrocatalysts in terms of effectiveness [83]. The primary reasons are minimum access to the active sites, inert basal planes, and low conductivity, which are responsible for low electrocatalytic activity [83]. As such, different approaches have been used to enhance the electrocatalytic activity of TMDC materials toward hydrogen production. Electrocatalytic activity toward HER depends on two parameters: enhanced charge transfer and inheriting other materials' electrocatalytic effect (synergistic effects). Since motivating and manipulating the surface of the TMDC materials, various approaches have been used involving two core features, such as cumulative dynamic sites and elevated electrical conductivity. However, TMDC-based electrocatalysts have shown reduced conductivity, thus restricting the HER kinetics. As such, new approaches to increase electron transportation for HER are of interest [83].

The new approaches include strain engineering, doping, and developing synergetic hybrid materials [83]. Furthermore, TMDCs with few layers are metallic, which is crucial in accelerating electron transfer to enhance electrocatalytic activity [136-141]. Herein, the focus is on the development of synergetic hybrid materials. For example, TMDC materials have been combined with carbon-based materials (including carbon dots, carbon nanotubes, graphene,

and other carbon materials), which have an incredible electron transfer ability and chemical stability [83]. The carbon-based materials prevent agglomeration and improve the charge transfer processes [142-144]. In addition, these increase the overall conductivity of the TMDC hybrid and further improve the electrocatalytic kinetics. Using the solvothermal technique, Dai *et al.* formed MoS_2 nanoparticles on reduced graphene oxide (RGO) sheets [142]. The MoS_2/RGO hybrid resulted in maximum exposure of the MoS_2 edges and showed excellent electrocatalytic activity towards HER compared to bare MoS_2 [142]. The MoS_2/RGO hybrid resulted in a 41 mV/dec Tafel slope and lower impedance at an overpotential of 0.12 V than bare MoS_2. The accelerated electrocatalytic processes towards HER are due to the strong coupling effect between MoS_2 and significantly conducting graphene sheets [142]. Coleman *et al.* also improved charge transfer by forming MoS_2 and single-walled carbon nanotubes [145]. Exposed active sites are reached through the highly conductive channels of the carbon nanotubes [145].

Interfacial engineering of TMDC electrocatalysts to enhance their activity towards HER can be achieved through different approaches such as (i) interfacial bonding, (ii) electrical contact, (iii) changes in morphology, (iv) introduction of defects, (v) change in phases, (vi) composition, and (vi) lattice strain [146-151]. Interfacial engineering may improve the electronic structures of the active sites targeting intermediates such as hydrogen [146-151]. Xu *et al.* proved that interfacial engineering successfully formed ultrathin $Ni(OH)_2/Ni_3S_2$ nanosheets using the synthetic electrodeposition technique [83]. In this case, the Ni_3S_2 electrocatalyst is used in conjunction with the $Ni(OH)_2$ co-electrocatalyst; therefore, the Ni_3S_2 atomic surface configuration is highly regulated, resulting in an efficient enhancement in the different kinetic steps (including the Volmer step, adsorption of OH^-). The resultant overpotential under $Ni(OH)_2/Ni_3S_2$ nanosheet electrocatalyst in an alkaline medium was 50 mV [83]. $Ni(OH)_2/Ni_3S_2$ nanoforest was used in an alkaline electrolyser as a bi-functional electrocatalyst to produce 100 mA/cm^2 with a cell voltage of 1.64 V even though it was stable for 20 h at 1.55 V [152]. Chen *et al.* also developed an effective interfacial engineering technique that formed NiS@MoS_2 core-shell hierarchical microspheres [153]. Essentially, the NiS hierarchical micro-sized spheres have the ultrathin MoS_2 nanosheets formed on their surface. These hierarchical microspheres helped the adsorption of hydrogen intermediates synergistically and enhanced HER activity. They produced a low overpotential of 146 mV in 1.0 M KOH. The process confirms that the core-shell hierarchical microspheres and a multi-

scale method help control the electronic structure of the hybrid materials for the enhanced HER performance [154].

2.3 References

[1] R. Sukanya, D. C. da Silva Alves, C. B. Breslin, *Journal of The Electrochemical Society*, 2022, 169, 064504.

[2] Y. Sim, Y. Chae, S. Kwon, *iScience*, 2022, 25, 105098,

[3] M. S. Sokolikova, P. C. Sherrell, P. Palczynski, V. L. Bemmer, C. Mattevi, *Nat. Commun.*, 2019, 10, 712.

[4] S. A. Han, R. Bhatia, S. W. Kim, *Nano Converg.* 2015, 2, 17.

[5] B. Sipos, A. F. Kusmartseva, A. Akrap, H. Berger, L. Forró, E. Tutĭs, *Nat. Mater*. 2008, 7, 960.

[6] R. Gordon, D. Yang, E. Crozier, D. Jiang, R. Frindt, *Phys. Rev. B*, 2002, 65, 125407.

[7] Q. Tang, D. E. Jiang, *ACS Catal.*, 2016, 6, 4953.

[8] Z. Lai, *Nat. Mater.*, 2021, 20, 1113.

[9] K. F. Mak, J. Shan, *Nat. Photon.*, 2016, 10, 216-226.

[10] M. Bernardi, C. Ataca, M. Palummo, J. C. Grossman, *Nanophotonics*, 2017, 6, 479-493.

[11] M. Chhowalla, H.S. Shin, G. Eda, L. J. Li, K.P. Loh, H. Zhang, *Nat. Chem.*, 2013, 5, 263–275.

[12] K. A. N. Duerloo, Y. Li, E. J, Reed, *Nat. Commun.*, 2014, 5, 4214–4219.

[13] K. Hernandez Ruiz, Z. Wang, M. Ciprian, M. Zhu, R. Tu, L. Zhang, W. Luo, Y. Fan, W. Jiang, *Small Sci.*, 2022, 2, 2100047.

[14] C. Zhang, C. Gong, Y. Nie, K. A. Min, C. Liang, Y. J. Oh, H. Zhang, W. Wang, S. Hong, L. Colombo, et al., *2D Mater.*, 2016, 4, 015026.

[15] S. Jeong, D. Yoo, J. T. Jang, M. Kim, J. Cheon, *J. Am. Chem. Soc.*, 2012, 134, 18233–18236.

[16] Y. Deng, Y. Lai, X. Zhao, X. Wang, C. Zhu, K. Huang, C. Zhu, J. Zhou, Q. Zeng, R. Duan, et al., *J. Am. Chem. Soc.*, 2020, 142, 2948–2955.

[17] W. Fu, Y. Chen, J. Lin, X. Wang, Q. Zeng, J. Zhou, L. Zheng, H. Wang, Y. He, H. He, et al., *Chem. Mater.*, 2016, 28, 7613-7618.

[18] J. Li, B. Zhao, P. Chen, R. Wu, B. Li, Q. Xia, G. Guo, J. Luo, K. Zang, Z. Zhang, et al., *Adv. Mater.*, 2018, 30, 1801043.

[19] X. Xi, L. Zhao, Z. Wang, H. Berger, L. Forro´, J. Shan, K. F. Mak, *Nat. Nanotechnol.*, 2015, 10, 765-769.

[20] E. Navarro-Moratalla, J. O. Island, S. Manas-Valero, E. Pinilla-Cienfuegos, A. Castellanos-Gomez, J. Quereda, G. Rubio-Bollinger, L. Chirolli, J. A. Silva-Guillen, N. Agrait, et al., *Nat. Commun.*, 2016, 7, 11043–11047.

[21] C. Huo, Z. Yan, X. Song, H. Zeng, *Sci. bull.*, 2015, 60, 1994-2008.

[22] Q. Zhang, L. Mei, X. Cao, Y. Tang, Z. Zeng, *J. Mater. Chem. A*, 2020, *8*, 15417-15444.

[23] L. Manamela, J. N. Fru, P. I. Kyesmen, M. Diale, N. Nombona, *Front. Chem.*,2020, 1163.

[24] D. B. Velusamy, R. H. Kim, S. Cha, J. Huh, R. Khazaeinezhad, S. H. Kassani, G. Song, S. M. Cho, S. H. Cho, I. Hwang, *Nat. Commun.*, 2015, 6, 1-11.

[25] D. T. Nguyen, H. A.Ting, Y. H. Su, M. Hofmann, Y. P. Hsieh, *Nanomaterials*, 2021, 11, 601.

[26] C. Backes, D. Hanlon, B. M. Szydlowska, A. Harvey, R. J. Smith, T. M. Higgins, J. N. Coleman, *J. Vis. Exp.*, 2016, 118, e54806.

[27] V. Nicolosi, M. Chhowalla, M. G. Kanatzidis, M. S. Strano, J. N. Coleman, *Science*, 2013, 340, 1226419.

[28] L. Niu, J. N. Coleman, H. Zhang, H. Shin, M. Chhowalla, Z. Zheng, *Small*, 2016, 12, 272-293.

[29] O. V. Yazyev, A. Kis, *Mater. Today*, 2015, 18, 20-30.

[30] E. Varrla, C. Backes, K. R. Paton, A. Harvey, Z. Gholamvand, J. McCauley, J. N. Coleman, *Chem. Mater.*, 2015, 27, 1129-1139.

[31] J. Yao, H. Liu, Q. He, K. Chen, Y. Wu, X. Li, C. Zhang, Z. Wu, and J. Kang, Appl. Surf. Sci., 2022, 572, 151438.

[32] Y. Tian, M. Zheng, Y. Cheng, Z. Yin, J. Jiang, G. Wang, J. Chen, X. Li, J. Qi, and X. Zhang, J. Mater. Chem. C, 2021, 9, 13954.

[33] N. Babu Shinde, B. Deul Ryu, C. H. Hong, B. Francis, S. Chandramohan, S. Kumar Eswaran, G. Behavior, Appl. Surf. Sci., 2021, 568, 150908.

[34] J. Li, S. Kolekar, Y. Xin, P. M. Coelho, K. Lasek, F. A. Nugera, H. R. Gutiérrez, M. Batzill, Chem. Mater., 2021, 33, 8018.

[35] X. Chen, B. Huet, T. H. Choudhury, J. M. Redwing, T. M. Lu, and G. C. Wang, *Appl. Surf. Sci.*, 2021, 567, 150798.

[36] G. Liu, Z. Li, T. Hasan, X. Chen, W. Zheng, W. Feng, D. Jia, Y. Zhou, P. Hu, *J. Mater. Chem. A*, 2017, 5, 1989.

[37] P. Chen, *Mater. Sci. Semicond. Process.*, 2022, 138, 106253.

[38] A. S. Sindhu, N. B. Shinde, S. Harish, M. Navaneethan, S. K. Eswaran, *Chemosphere*, 2022, 287, 132347.

[39] H. Cun, M. Macha, H. Kim, K. Liu, Y. Zhao, T. LaGrange, A. Kis, *Nano Res.*, 2019, 12, 2646-2652.
[40] J. Wu, Y. Liu, Y. Yao, Y. Shao, X. Wu, *J. Alloys Compd.*, 2021, 877, 160317.
[41] H. Tian, C. Fan, G. Liu, Y. Zhang, M. Wang, E. Li, J. Mater. Sci., 2019, 54, 2059.
[42] S. Sengupta, M. Kundu, *ChemistrySelect*, 2020, 5, 14183.
[43] Y. Qi, J. Wu, J. Xu, H. Gao, Z. Du, B. Liu, L. Liu, D. Xiong, *Inorg. Chem. Front*, 2020, 7, 2523.
[44] N. Jeromiyas, C. M. Lin, L. Yu-Chieh, C. H. Chen, V. Mani, R. Arumugam, S. T. Huang, *Inorg. Chem. Front*, 2021, 8, 2871.
[45] S. Shanmugaratnam, D. Velauthapillai, P. Ravirajan, A. A. Christy, Y. Shivatharsiny, Materials *(Basel)*, 2019, 12, 03882.
[46] A. Gowrisankar, A. L. Sherryn, and T. Selvaraju, *Appl. Surf. Sci. Adv.*, 2021, 3, 100054.
[47] R. Fan, X. Chen, Z. Chen, *Chem. Lett.*, 2000, 29, 920-921.
[48] M. Sakthivel, S. Ramaraj, S. M. Chen, T. W. Chen, K. C. Ho, *ACS Appl. Mater. Interfaces*, 2019, 11, 18483.
[49] I. S. Kwon, I. H. Kwak, J. Y. Kim, T. T. Debela, Y. C. Park, J. Park, H. S. Kang, *ACS Nano*, 2021, 15, 5467.
[50] T. Pellegrino, S. Kudera, T. Liedl, A. Muñoz Javier, L. Manna, W. J. Parak, *Small*, 2005, 1, 48-63.
[51] Y. Wang, Y. Xia, *Nano lett.*, 2004, 4 (10), 2047-2050.
[52] N. Chestnoy, T. D. Harris, R. Hull, L. E. Brus, *J. Phys. Chem.*, 1986, 90, 3393-3399.
[53] V. K. LaMer, R. H. Dinegar, *J. Am. Chem. Soc.*, 1950, 72, 4847-4854.
[54] J. Polte, CrystEngComm, 2015, 17, 6809-6830.
[55] T. Li, G. Galli, *J. Phys. Chem. C*, 2007, 111, 16192.
[56] A. Pospischil, M. M. Furchi, T. Mueller, Nat. Nanotechnol., 2014, 9, 257–261.
[57] W. Ostwald, Science Progress, 1896, 4, 419-436.
[58] K. De Nolf, R. K. Capek, S. Abe, M. Sluydts, Y. Jang, J. C. Martins, S. Cottenier, E. Lifshitz, Z. Hens, *J. Am. Chem. Soc.*, 2015, 137, 2495-2505.
[59] N. Mirbagheri, S. Engberg, A. Crovetto, S. B. Simonsen, O. Hansen, Y. M. Lam, J. Schou, *Nanotechnology*, 2016, 27, 185603.
[60] B. R. Bade, S. R. Rondiya, Y. A. Jadhav, M. M. Kamble, S. V. Barma, S. B. Jathar, M. P. Nasane, S. R. Jadkar, A. M. Funde, N. Y. Dzade, *J. Alloys Compd.*, 2021, 854, 157093.
[61] M. Kulpa-Greszta, A. Tomaszewska, A. Dziedzic, R. Pązik, *RSC Adv.*, 2021, 11, 20708-20719.

[62] J. van Embden, A. S. Chesman, J. J. Jasieniak, *Chem. Mater.*, 2015, 27, 2246-2285.
[63] Z. Ndala, N. Shumbula, S. Nkabinde, T. Kolokoto, O. Nchoe, P. Shumbula, Z. N. Tetana, E. C. Linganiso, S. S. Gqoba, N. Moloto, *Nanomaterials*, 2020, 10, 1786.
[64] F. Baletto, R. Ferrando, *Reviews of modern physics*, 2005, 77, 371.
[65] H. Chauhan, Y. Kumar, S. Deka, *Nanoscale*, 2014, 6, 10347-10354.
[66] R. A. Sperling, W. Parak, *Philos. Trans. Royal Soc. A: Math. Phys. Eng. Sci.*, 2010, 368, 1333-1383.
[67] M. S. Bakshi, *Cryst. Growth Des*., 2015, 16, 1104-1133.
[68] L. F. Machogo, R. K. Sithole, N. Phao, T. Kolokoto, S. S. Gqoba, M. Mlambo, M. J. Moloto, P. M. Shumbula, P. S. Mdluli, N. Moloto, *Mater. Sci. Eng. B*, 2021, 263, 114878.
[69] S. Daniels, *Google Patents*, 2021.
[70] S. Daniels, N. L. Pickett, *Google Patents*, 2020.
[71] T. Shan-Shan, W. Xue-Jing, L. Qing-Chuan, H. Xiao-Jun, J. Anal. Chem., 2016, 44, 1447-1457.
[72] J. A. Turner, Science, 1999, 285, 687-689.
[73] Z. Chen, X. Duan, W. Wei, S. Wang, B. Ni, J. mater. Chem. *A*, 2019, 7, 14971-15005.
[74] J. E. Payne, Appl. Energy, 2010, 87, 723-731.
[75] Z. W. Seh, J. Kibsgaard, C. F. Dickens, I. Chorkendorff, J. K. Nørskov, T. F. Jaramillo, Science, 2017, 355, eaad4998.
[76] T. R. Cook, D. K. Dogutan, S. Y. Reece, Y. Surendranath, T. S. Teets, D. G. Nocera, *Chem. Rev.*, 2010, 110, 6474-6502.
[77] H. B. Gray, *Nature Chem.*, 2009, 1, 7.
[78] M. Gong, D. Y. Wang, C. C. Chen, B. J. Hwang, H. Dai, *Nano Res.*, 2016, 9, 28-46.
[79] Y. Y. Liang, Y. G. Li, H. L. Wang, H. J. Dai, *J. Am. Chem. Soc.*, 2013, 135, 2013-2036.
[80] A. J. Byrd, K. K. Pant, R.B. Gupta, *Energy Fuels*, 2007, 21, 3541-3547.
[81] J. Bard, L. R. Faulkner, *Wiley*, 2000, 2nd Edition.
[82] Y. Yan, B. Y. Xia, B. Zhao, X. Wang, *J. Mater. Chem. A*, 2016, 4, 17587-17603.
[83] J. Wang, X. Yue, Y. Yang, S. Sirisomboonchai, P. Wang, X. Ma, A. Abudula, G. Guan, *J. Alloys Compd.*, 2020, 819, 153346.
[84] A. Mondal, A. Vomiero, Adv. Funct. Mater., 2022, 32, 2208994.
[85] K. Zhu, C. Li, Z. Jing, X. Liu, Y. He, X. Lv, Y. Wang, K. Liu, *FlatChem*, 2019, 18, 100140.
[86] S. Trasatti, Electrodes of Conductive Metallic Oxides, *Elsevier Scientific Software*, 1980.

[87] H. Wolfschmidt, O. Paschos, U. Stimmings, Full Cell Science, John Wiley & Sons Inc, Hoboken, New Jersey, 2010.
[88] N. Mahmood, Y. Yao, J. Zhang, L. Pan, X. Zhang, J. Zou, *Adv. Sci.*, 2018, 5, 1700464-1700487.
[89] J. Wang, F. Xu, H. Jin, Y. Chen, Y. Wang, *Adv. Mater.*, 2017, 29.
[90] K. G. dos Santos, C. T. Eckert, E. De Rossi, R. A. Bariccatti, E. P. Frigo, C. A. Lindino, H. J. Alves, *Renewable Sustainable Energy Rev.*, 2017, 68, 563.
[91] J. Mahmood, F. Li, S. M. Jung, M. S. Okyay, I. Ahmad, S. J. Kim, N. Park, H. Y. Jeong, J. B. Baek, *Nat. Nanotechnol.*, 2017, 12, 441.
[92] N. Danilovic, R. Subbaraman, D. Strmcnik, V. Stamenkovic, N. Markovic, J. Serb. *Chem. Soc.*, 2013, 78, 2007.
[93] W. Sheng, M. Myint, J. G. Chen, Y. Yan, *Energy Environ. Sci.*, 2013, 6, 1509.
[94] B. E. Conway, G. Jerkiewicz, *Electrochim. Acta*, 2000, 45, 4075.
[95] X. Li, P. F. Liu, L. Zhang, M. Y. Zu, Y. X. Yang, H. G. Yang, *Chem. Commun.*, 2016, 52, 10566.
[96] B. Liu, Y. F. Zhao, H. Q. Peng, Z. Y. Zhang, C. K. Sit, M. F. Yuen, T. R. Zhang, C. S. Lee, W. J. Zhang, *Adv. Mater.*, 2017, 29, 1606521.
[97] R. Subbaraman, D. Tripkovic, D. Strmcnik, K.-C. Chang, M. Uchimura, A. P. Paulikas, V. Stamenkovic, N. M. Markovic, *Science*, 2011, 334, 1256.
[98] N. Danilovic, R. Subbaraman, D. Strmcnik, K. C. Chang, A. P. Paulikas, V. R. Stamenkovic, N. M. Markovic, *Angew. Chem. Int. Ed. Engl.*, 2012, 51, 12495.
[99] Y. Shi, B. Zhang, *Chem. Soc. Rev.*, 2016, 45, 1529-1541.
[100] Y. Jiao, Y. Zheng, M. Jaroniec, S. Z. Qiao, *Chem. Soc. Rev.*, 2015, 44, 2060-2086.
[101] X. Zou, Y. Zhang, *Chem. Soc. Rev.*, 2015, 44, 5148-5180.
[102] H. Jin, C. Guo, X. Liu, J. Liu, A. Vasileff, Y. Jiao, Y. Zheng, S. Z. Qiao, *Chem. Rev.*, 2018, 118, 6337-6408.
[103] D. Voiry, H. S. Shin, K. P. Loh, M. Chhowalla, *Nat. Rev. Chem.*, 2018, 2, 0105.
[104] J. Li, N. Wu, *Catal. Sci. Technol.*, 2015, 5, 1360-1384.
[105] R. Singh, S. Dutta, *Fuel*, 2018, 220, 607-620.
[106] H. Ahmad, S. K. Kamarudin, L. J. Minggu, M. Kassim, *Renew. Sustain. Energy Rev.*, 2015, 43, 599-610.
[107] C. Acar, I. Dincer, F. Naterer Greg, *Int. J. Energy Res.*, 2016, 40, 1449-1473.
[108] Y. Luo, L. Tang, U. Khan, Q. Yu, H. M. Cheng, X. Zou, B. Liu, *Nat. Commun.*, 2019, 10, 269.

[109] S. Anantharaj, S. R. Ede, K. Sakthikumar, K. Karthick, S. Mishra, S. Kundu, *ACS Catal.*, 2016, 6, 8069-8097.

[110] J. Xie, J. Zhang, S. Li, F. Grote, X. Zhang, H. Zhang, R. Wang, Y. Lei, B. Pan, Y. Xie, *J. Am. Chem. Soc.*, 2013, 135, 17881-17888.

[111] C. Wei, R. R. Rao, J. Peng, B. Huang, I. E. L. Stephens, M. Risch, Z. J. Xu, Y. ShaoHorn, *Adv. Mater.*, 2019, 1806296.

[112] M. A. Lukowski, A. S. Daniel, F. Meng, A. Forticaux, L. Li, S. Jin, J. Am. *Chem. Soc*., 2013, 135, 10274-10277.

[113] A. A. Topalov, S. Cherevko, A. R. Zeradjanin, J. C. Meier, I. Katsounaros, K. J. J. Mayrhofer, *Chem. Sci.*, 2014, 5, 631-638.

[114] J. G. Chen, C. W. Jones, S. Linic, V. R. Stamenkovic, *ACS Catal.*, 2017, 7, 6392-6393.

[115] D. Voiry, M. Salehi, R. Silva, T. Fujita, M. Chen, T. Asefa, V. B. Shenoy, G. Eda, M. Chhowalla, *Nano Lett.*, 2013, 13, 6222-6227.

[116] S. Sun, H. Li, Z. J. Xu, *Joule*, 2018, 2, 1024-1027.

[117] S. Trasatti, O. A. Petrii, *J. Electroanal. Chem.*, 1992, 327, 353-376.

[118] Z. Lai, A. Chaturvedi, Y. Wang, T. H. Tran, X. Liu, C. Tan, Z. Luo, B. Chen, Y. Huang, G. H. Nam, Z. Zhang, Y. Chen, Z. Hu, B. Li, S. Xi, Q. Zhang, Y. Zong, L. Gu, C. Kloc, Y. Du, H. Zhang, *J. Am. Chem. Soc.*, 2018, 140, 8563-8568.

[119] Y. Chen, R. Ren, Z. Wen, S. Ci, J. Chang, S. Mao, J. Chen, *Nano Energy*, 2018, 47, 66-73.

[120] Z. Liu, T. He, Q. Jiang, W. Wang, J. Tang, *Int. J. Hydrogen Energy*, 2022, 47, 29698.

[121] P. Sundara Venkatesh, N. Kannan, M. Ganesh Babu, G. Paulraj, K. Jeganathan, *Int. J. Hydrogen Energy*, 2022, 47, 35123.

[122] X. Geng, W. Wu, N. Li, W. Sun, J. Armstrong, A. Al-hilo, M. Brozak, J. Cui, T. Chen, *Adv. Funct. Mater.*, 2014, 24, 6123.

[123] Z. Lin, B. Xiao, Z. Wang, W. Tao, S. Shen, L. Huang, J. Zhang, F. Meng, Q. Zhang, L. Gu, W. Zhong, *Adv. Funct. Mater.*, 2021, 31, 2102321.

[124] W. Li, L. Zhao, X. Jiang, Z. Chen, Y. Zhang, S. Wang, *Adv. Funct. Mater.*, 2022, 2207727.

[125] K. Mistry, Jalja, R. Lakhani, B. Tripathi, S. Shinde, P. Chandra, *Int. J. Hydrogen Energy*, 2022.

[126] Z. Wang, M. T. Tang, A. Cao, K. Chan, J. K. Norskov, *J. Phys. Chem. C*, 2022, 126, 5151.

[127] S. Li, B. Fei, *Mater. Sci. Technol.*, 2022, 38, 535.

[128] P. Zhang, H. Xiang, L. Tao, H. Dong, Y. Zhou, T. S. Hu, X. Chen, S. Liu, S. Wang, S. Garaj, *Nano Energy*, 2019, 57, 535.

[129] J. K. Norskov, T. Bligaard, A. Logadottir, J. R. Kitchin, J. G. Chen, S. Pandelov, U. Stimming, *J. Electrochem. Soc.*, 2005, 152, J23.

[130] A. B. Laursen, A. S. Varela, F. Dionigi, H. Fanchiu, C. Miller, O. L. Trinhammer, J. Rossmeisl, S. Dahl, *J. Chem. Educ.*, 2012, 89, 1595.

[132] G. Zhao, K. Rui, S. X. Dou, W. Sun, *Adv. Funct. Mater.*, 2018, 28, 1803291.

[133] G. Shao, X. Xue, B. Wu, Y. Lin, M. Ouzounian, T. S. Hu, Y. Xu, X. Liu, S. Li, K. Suenaga, Y. Feng, S. Liu, *Adv. Funct. Mater.*, 2020, 30, 1906069.

[134] J. Bonde, P. G. Moses, T. F. Jaramillo, J. K. Norskov, I. Chorkendorff, *Faraday Discuss.*, 2009, 140, 219.

[135] C. Tsai, K. Chan, F. Abild-Pedersen, J. K. Norskov, *Phys. Chem. Chem. Phys.*, 2014, 16, 13156.

[136] J. Xu, G. Shao, X. Tang, F. Lv, H. Xiang, C. Jing, S. Liu, S. Dai, Y. Li, J. Luo, Z. Zhou, *Nat. Commun.*, 2022, 13, 2193.

[137] L. Lin, P. Sherrell, Y. Liu, W. Lei, S. Zhang, H. Zhang, G. G. Wallace, J. Chen, *Adv. Energy Mater.*, 2020, 10, 1903870.

[138] A. Mondal, A. Paul, D. N. Srivastava, A. B. Panda, *ACS Appl. Nano Mater.*, 2018, 1, 4622.

[139] C. Jian, W. Hong, Q. Cai, J. Li, W. Liu, *Appl. Catal. B*, 2020, 266, 118649.

[140] S. Mao, Z. Wen, S. Ci, X. Guo, K. K. Ostrikov, J. Chen, *Small*, 2015, 11, 414.

[141] K. A. Novčić, C. Iffelsberger, S. Ng, M. Pumera, *Nanoscale*, 2021, 13, 5324.

[142] J. Jang, D. K. Hwang, *J. Korean Phys. Soc.*, 2020, 77, 1008.

[143] Y. Li, H. Wang, L. Xie, Y. Liang, G. Hong, H. Dai, *J. Am. Chem. Soc.*, 2011, 133, 7296.

[144] J. Ye, Z. Yu, W. Chen, Q. Chen, S. Xu, R. Liu, *Carbon*, 2016, 107, 711.

[145] Y. R. Zheng, M. R. Gao, Z. Y. Yu, Q. Gao, H. L. Gao, S. H. Yu, *Chem. Sci.*, 2015, 6, 4594.

[146] D. McAteer, Z. Gholamvand, N. McEvoy, A. Harvey, E. O'Malley, G. S. Duesberg, J. N. Coleman, *ACS Nano*, 2016, 10, 672.

[147] W. Liao, S. Zhao, F. Li, C. Wang, Y. Ge, H. Wang, S. Wang, H. Zhang, *Nanoscale Horiz.*, 2020, 5, 787.

[148] K. Cho, J. Pak, S. Chung, T. Lee, *ACS Nano*, 2019, 13, 9713.

[149] R. Luo, W. W. Xu, Y. Zhang, Z. Wang, X. Wang, Y. Gao, P. Liu, M. Chen, *Nat. Commun.*, 2020, 11, 1011.

[150] Y. Zhao, K. Xu, F. Pan, C. Zhou, F. Zhou, Y. Chai, *Adv. Funct. Mater.*, 2017, 27, 1603484.

[151] J. Peng, X. Chen, W.-J. Ong, X. Zhao, N. Li, *Chem*, 2019, 5, 18.

[152] C. A. Chen, C. L. Lee, P. K. Yang, D. S. Tsai, C. P. Lee, *Catalysts*, 2021, 11, 151.

[153] Q. Xu, H. Jiang, H. Zhang, Y. Hu, C. Li, *Appl. Catal. B.*, 2019, 242, 60.

[154] Z. Chen, X. Liu, P. Xin, H. Wang, Y. Wu, C. Gao, Q. He, Y. Jiang, Z. Hu, S. Huang, *J. Alloys Compd.*, 2021, 853, 157352.

Chapter 3

Activating the inert two-dimensional $NbSe_2$ surface by decorating with Ni and Pt-based nanoparticles to enhance the electrocatalytic activity to produce hydrogen

3.1. Introduction

The drastic climate changes caused by burning fossil fuels have made it a pressing matter to develop sustainable energy systems [1]. Climate change effects can be reduced by using hydrogen gas as a clean fuel. Hydrogen is regarded as the best energy carrier. It is a lightweight molecule with a higher energy density than any fossil fuels. It is sustainable, environmentally friendly, and non-toxic such that when combined with oxygen from the air the only by-product is water. Water splitting is the most attractive and promising technique for hydrogen production due to its environmental friendliness [1-3]. Water splitting is achieved by two half-reactions, namely, the hydrogen evolution reaction (HER) at the cathode and the oxygen evolution reaction at the anode. Herein, we focus on HER.

Efficient electrocatalysts are required to promote the water-splitting process. Currently, the most efficient electrocatalysts are noble metal-based such as Pt [1, 4, 5] and at times Ru [6] for HER in proton exchange membrane cells and alkaline cells. Pt is said to be the most efficient electrocatalyst because it exhibits a low overpotential [1]. In recent years, there has been a consideration of using earth-abundant materials that have the potential to match the performance of the expensive noble metal-based electrocatalysts [7-10]. More specifically, transition metal dichalcogenides (TMDCs) are rapidly emerging as alternative cost-effective electrocatalysts for Pt-based systems [8-15]. Especially the diselenides because they have uniquely interesting physiochemical properties (such as high surface area and good chemical

stability) [16-18] and they can be modified using different transition metals to enhance their catalytic activity [1, 10, 19, 20]. 2D materials are restricted by the density of their catalytic sites and the inert basal plane [21]. As such, a new field in research has been opened in the integration of 2D and non-2D materials to improve their activity [22-27]. Ideally, such materials should provide a synergy that is larger than the sum of the counterparts [22, 28, 29]. Different methodologies have been used to synthesise these hybrid nanomaterials where the more stable 2D material is first synthesised, and then the non-2D is introduced [22]. In this study, two synthetic methods were used: ex-situ and in-situ methods. Both methods involved the formation of the 2D $NbSe_2$ using the heat-up colloidal method first [30], followed by the formation of the 0D nanomaterials using the same heat-up colloidal synthesis method and then the two were combined in the ex-situ method. Whereas, in the in-situ method the 2D material was combined with the metal salts and heated up in a furnace for the hybrid formation. Cases such as the formation of hybrid nanomaterials suggest that the decoration of the 2D $NbSe_2$ in-plane using transition metal-based nanoparticles, may achieve the electrocatalytic activity enhancement goal. Herein, the electrochemical performance of decorated $NbSe_2$ using transition metal-based nanoparticles (Pt, Ni, as well as Pt and Ni combined) towards HER was evaluated.

3.2. Methodology

3.2.1 Chemicals

Niobium(V) chloride ($NbCl_5$, 99%), selenourea (SU) (98%), oleylamine (OLA) (70%), hexane (95%), ethanol (96%), sodium borohydride ($NaBH_4$, ≥ 98%), potassium hydroxide (KOH, 90%), isopropanol (≥ 99.5%), Nafion (5 wt%), nickel(II) bis(acetylacetonate) ($Ni(acac)_2$, 95%), and platinum(II) bis(acetylacetonate) ($Pt(acac)_2$, 97%) were all purchased from Sigma-Aldrich.

3.2.2 Synthesis of $NbSe_2$

The synthesis of 2D $NbSe_2$ nanomaterial was done following the Kolokoto *et al.* heat-up colloidal synthesis procedure where the optimum conditions were using $NbCl_5$ and SU in OLA for 120 min at 320 ℃ under N_2 flow [30].

3.2.3 Decoration of $NbSe_2$ using the ex-situ method

In the ex-situ synthetic method, the ratio of the reducing agent $NaBH_4$ to metal precursor was 1:1, this mixture was added to a degassed OLA in a three-necked round bottom flask. Table 1 contains the reaction conditions used for each sample.

Table 1: Summary of the reaction conditions for the synthesis of Ni and Pt nanoparticles

Sample	Metal precursor	Capping agent	Concentration (M)	Temperature (℃)	Time (min)
1	$Ni(acac)_2$	OLA	0.0500	280	320
2	$Pt(acac)_2$	OLA	0.0234	300	120

The readily synthesised nanoparticles were washed with hexane, followed by distilled water to remove excess/unreacted $NaBH_4$, and then dried and ready for characterisation. Once dried, the transition metal-based nanoparticles (20% wt.), Ni or Pt, were mixed with the $NbSe_2$ and added into 1 mL of ethanol. The mixture was sonicated for 60 min then placed onto a shaker at 180 rpm for 24 h. The mixture was then washed with hexane, dried, and ready for characterisation.

3.2.4 Decoration of $NbSe_2$ using the in-situ method

In the in-situ synthesis method, 20% wt of the metal source ($Ni(acac)_2$ or $Pt(acac)_2$) was mixed with the readily synthesised $NbSe_2$ and placed on a cylindrical steel reactor. The reactor was attached to an Ar gas line and loaded into a tubular furnace. The furnace was ramped at 2.5 $°C.min^{-1}$ until it reached 100 ℃ then held for 30 min at the same temperature to remove moisture. Then further ramped up at 2.5 $℃. min^{-1}$ until it reached 350 ℃ and held for 120 min. The furnace and reactor were cooled to room temperature overnight, and the product was ready for characterisation. The same synthetic procedure was used for the decoration of $NbSe_2$ using 10% wt. $Pt(acac)_2$ and 10% wt. $Ni(acac)_2$ (mixed metals).

3.2.5 Characterisation of the pristine $NbSe_2$ and the hybrid nanomaterials

The structure and phase of the powdered materials were determined using the Bruker MeasSrv (D2-205530)/D2-205530 diffractometer using secondary graphite monochromated Cu$K\alpha$ radiation (λ = l 1.54184 Å) at 30 kV/30 mA. Measurements were taken using a glancing angle of incidence detector at an angle of 2°, for 2θ values over 10 – 90° in steps of 0.026° with a

step time of 37 s, and at room temperature. X-ray photoelectron spectroscopy (XPS) measurements were performed with a Thermo ESCAlab 250Xi using monochromatic Al Kα (1486.7 eV) X-rays at a power of 300 W with a spot size of 900 mm. An FEI Spirit 120 kV transmission electron microscope (TEM) was operated at an accelerated voltage of 200 kV with a beam spot size of 20–100 nm in TEM mode and was also used to study the morphology of the samples. The samples were dispersed in hexane and drop-casted onto a lacey carbon copper grid. The solvent was then evaporated at room temperature.

3.2.6 Electrochemical characterisation

The Biologic SP 300 potentiostat was used to investigate the electrochemical performance of HER in a three-electrode system. The measurements were carried out in an alkaline solution of 0.1 M of KOH. The Ag/AgCl electrode was used as a reference electrode, the Pt wire as a counter electrode, and lastly, the working electrode was made up of the hybrid nanomaterials thin film on a glassy carbon electrode with a surface area of 0.07065 cm^2. For comparison, the electrochemical performance of pristine $NbSe_2$, as well as Pt/C, loaded onto the glassy carbon electrode were also measured. The inks were formed by dissolving 2.2 mg of the sample and 1.6 mg of Vulcan in a mixture of 20 μL Nafion (5 wt%) and 400 μL isopropanol, and then sonicated for 1 h. The thin films were formed by drop-casting about 10 uL of ink onto the glassy carbon electrode and left to dry at room temperature. The electrolyte was purged with argon for 30 min. This was followed by cyclic voltammetry (CV) measurements where the potential of the working electrode was swept between -0.2 – 0.5 V vs. RHE for 20 cycles at 100 mV/s. This process activates the surface of the electrocatalyst. The double layer was measured within the potential window of -0.2 – 0.4 V at various scan rates: 10, 15, 20, 25, 30, and 40 mV/s. The linear sweep voltammetry (LSV) was conducted at a scan rate of 2 mV/s. The electrochemical impedance spectroscopy measurements were recorded at a potential of -0.836 V vs RHE and a frequency range between 0.2 Hz and 100 kHz. The working electrode potentials vs Ag/AgCl were converted to the RHE scale using the equation below:

$$E_{RHE} = E_{Ag/AgCl} + 0.059pH + 0.0197$$

where E_{RHE} is the measured potential and pH = 13.

3.3. Results and discussion

3.3.1 Synthesis of $NbSe_2$

The XRD pattern of $NbSe_2$ resulted in the formation of 2H-$NbSe_2$ (PDF 01-070-5612) with some impurities denoted by '*' due to excess Se (Fig. 1a). The same results were obtained by Kolokoto *et al.* under the same reaction conditions [30]. The TEM image shown in Fig. 1b indicates that $NbSe_2$ had a sheet-like morphology, and this is consistent with the morphology of the layered materials [30]. Evident from the TEM image was the crimpling up of the nanosheets forming nanoflowers.

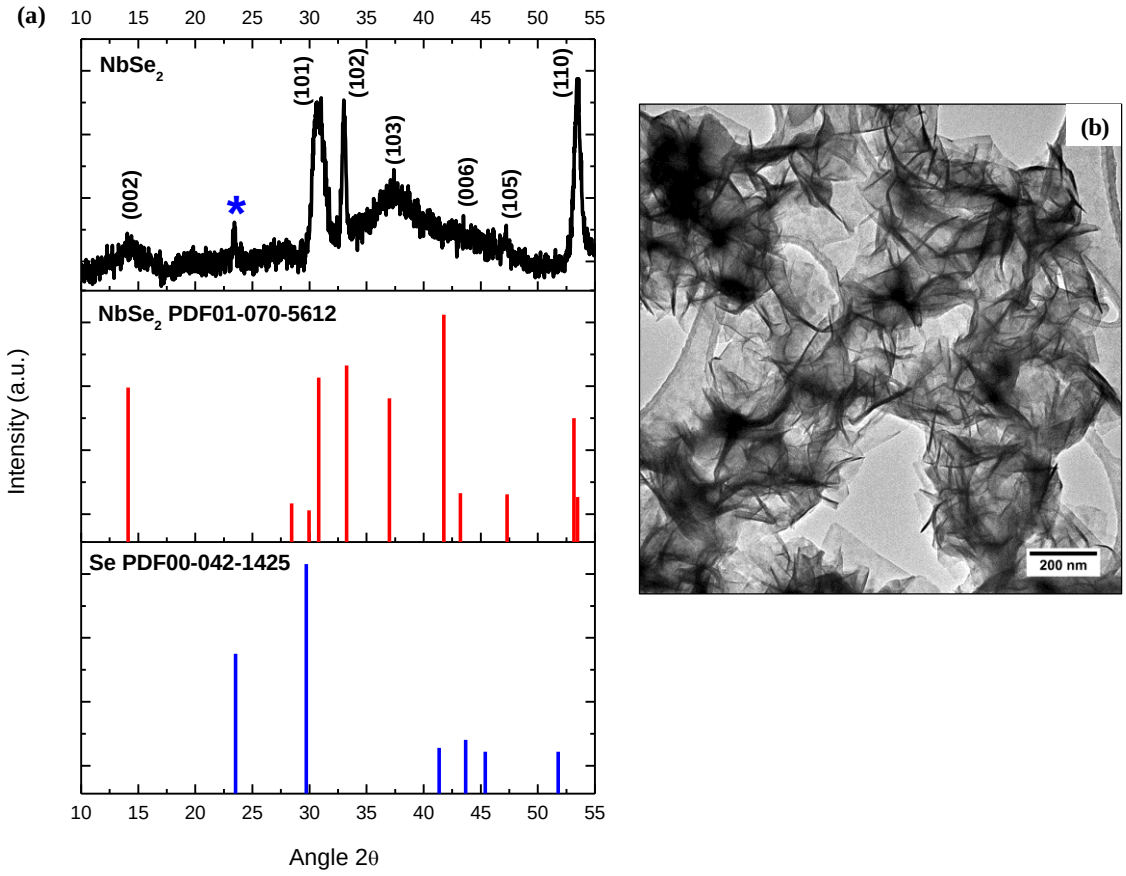

Fig.1: (a) XRD pattern and (b) TEM image of $NbSe_2$ nanoflowers; '*' represents the (100) plane of Se.

3.3.2 Decoration of $NbSe_2$ using Ni-based nanoparticles

Two methods were used to synthesise the Ni-decorated $NbSe_2$, namely, in-situ and ex-situ. The TEM results shown in Fig. 2 indicate that both materials were made of $NbSe_2$ 2D nanosheets with Ni-based nanoparticles on the surface of the sheets. The Ni-based nanoparticles were smaller in size and monodispersed evenly on the surface of the nanosheets in the in-situ method

(Fig. 2a) compared to the ex-situ method (Fig. 2b) that were more polydispersed with uneven distribution. Fig. S1 shows the TEM image of the polydispersed platelets of Ni-based nanoparticles that were used to decorate $NbSe_2$ in the ex-situ method.

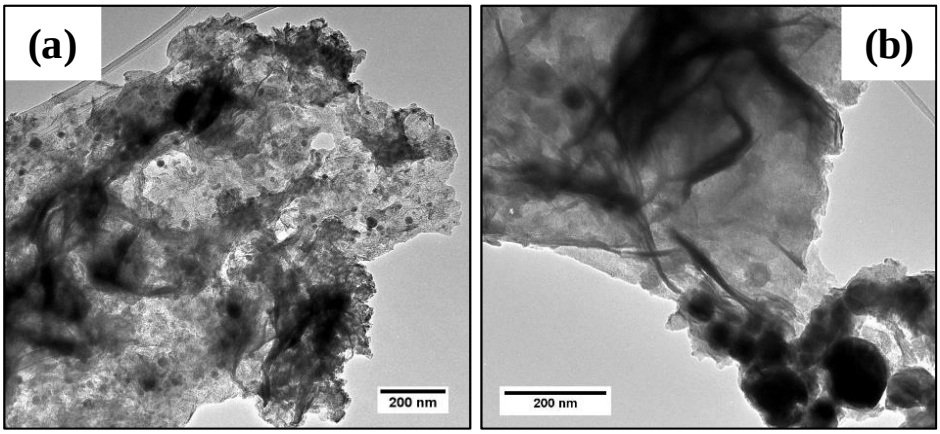

Fig. 2: TEM images of Ni-decorated $NbSe_2$ nanomaterials using the (a) in-situ method and (b) ex-situ method.

X-ray photoelectron spectroscopy (XPS) analysis was performed to further investigate the surface compositions and valency of the as-prepared in-situ and ex-situ Ni-decorated $NbSe_2$ nanomaterials. The XPS survey spectra of both nanomaterials in Fig. 3 contained the following species Ni, Nb, Se, C, and O, where O was due to the oxidation of the samples and C due to the capping agent used in the synthesis [31]. Fig. 4a shows the Ni 2p XPS spectrum of the in-situ sample. The Ni $2p_{1/2}$ was deconvoluted into peaks contributed by Ni^{2+} at 873 eV, Ni^{3+} at 875 eV, and satellite peak denoted as 'sat.' at 880 eV [32-35]. Similarly, the Ni^{2+}, Ni^{3+}, and satellite peaks can also be seen from Ni $2p_{3/2}$ at 856, 857, and 862 eV, respectively. The satellite peaks further provide evidence for the presence of Ni^{2+} [34,36]. The Ni $2p_{1/2}$ and Ni $2p_{3/2}$ peaks of the ex-situ sample were deconvoluted into peaks due to Ni^{2+}, Ni^{3+}, and satellite at 873, 875, and 879 eV ($2p_{1/2}$) and 856, 857, and 862 eV ($2p_{3/2}$), respectively. The presence of the Ni^{2+} peak in both samples indicated the formation of NiO [32]. The presence of Ni^{3+} indicates the formation of $Ni(OH)_2$. Fingerle *et al.* reported that Ni^{3+} ions can undergo surface reduction to Ni^{2+} ions, the unstable nature of Ni^{3+} leads to the formation of $Ni(OH)_2$ [32, 37]. In addition, the coexistence of a mixed valence of Ni^{2+} and Ni^{3+} is similar to the $Ni_{0.5}Se$ ($NiSe_2$) results that were previously reported [38-42]. Fig. S2c and d show the O1s spectra of both the ex-situ and in-situ samples. The O1s peak from the ex-situ sample was deconvoluted to two peaks: C-O at 532 eV and C=O at 533 eV. In this case, the C-O peak is attributed to O^{2-} from the N-O lattice [32, 43]. Whereas the C=O peak at higher binding energy indicates surface adsorbed oxygen (O_2) through the capping agent used to synthesise $NbSe_2$, this can be attributed to defective

sites [32, 44, 45]. Similarly, the O1s peak of the in-situ sample was deconvoluted into three peaks, metal oxide at 530 eV, C-O at 532 eV, and C=O at 533 eV. Compared to the ex-situ O1s spectrum, the in-situ O 1s spectra has an additional metal oxide peak which can be attributed to NiO (since the ratio is small compared to the other two peaks) [32]. Fig. S2a and b show the C 1s XPS spectra of the in-situ and ex-situ samples consisting of C-C (sp^2 and sp^3), C-O, O-C=O, and C=O. Fig. 4c and d show the in-situ and ex-situ Se 3d core level spectra. The spectra were deconvoluted into two peaks, $3d_{3/2}$ at 53.8 eV and 3d5/2 (53.0 eV) and they were both attributed to the $NbSe_2$ [47, 48]. However, the Se peaks in the ex-situ sample were more pronounced compared to the in-situ sample. Fig. 4e and f show the Nb 3d XPS spectra for the ex-situ and in-situ nanomaterials. The spectra contained three peaks Nb^{4+} $3d_{5/2}$ (203.0 eV), Nb^{5+} $3d_{5/2}$ (206.9 eV) and Nb^{5+} $3d_{3/2}$ (209.3 eV). The Nb^{4+} peak corresponds to $NbSe_2$ whereas the Nb^{5+} peaks correspond to Nb_2O_5 [30]. These results were in agreement with the work reported by Boscher *et al.* [30, 46].

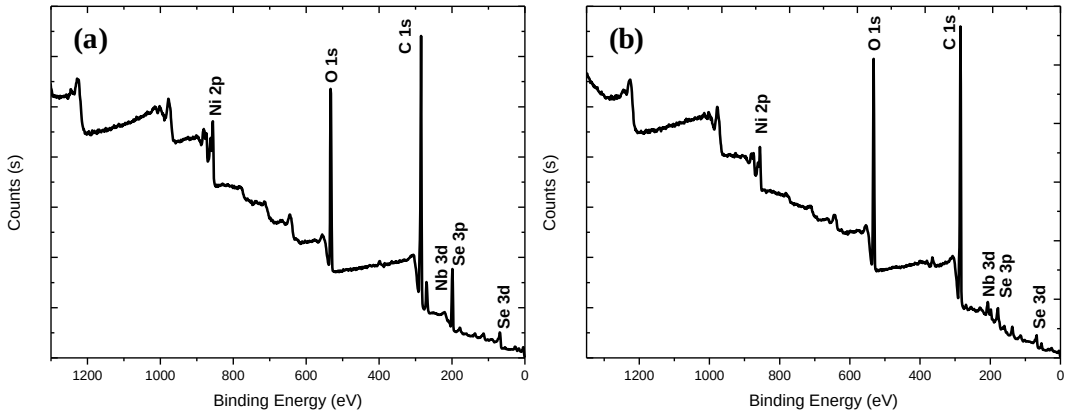

Fig. 3: XPS survey spectra of Ni-decorated $NbSe_2$ nanomaterials when varying the synthetic method (a) in-situ and (b) ex-situ.

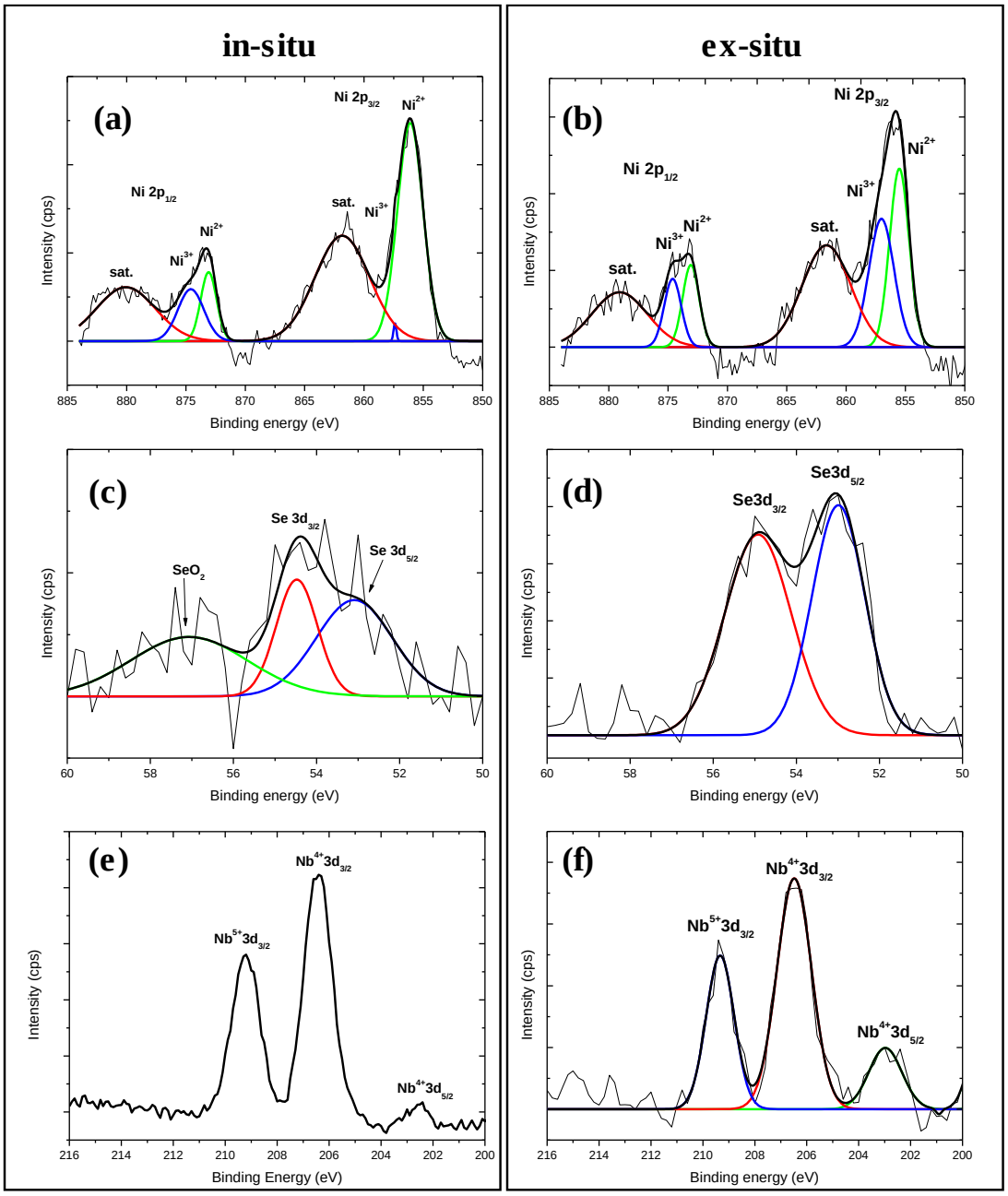

Fig. 4: (a) and (b) Ni 2p, (c) and (d) Se 3d, (e) and (f) Nb 3d XPS core-level spectra for the in-situ and ex-situ Ni-decorated $NbSe_2$ nanomaterials.

The phase, composition, and crystallinity of the in-situ and ex-situ Ni-decorated $NbSe_2$ samples were confirmed using XRD (shown in Fig. 5). These samples were compared to the pristine 2D $NbSe_2$. Fig. 5a shows that the in-situ sample consisted of $NbSe_2$. In addition, $Ni_{0.5}Se$ ($NiSe_2$) (COD #1537617) peaks were observed at 30.3, 33.6, 51.2° 2θ denoted by '$' and $Ni(OH)_2$ (COD #1011134) at 33.2° 2θ denoted by 'x'. Some overlapping of $Ni_{0.5}Se$ and $Ni(OH)_2$ peaks

with the $NbSe_2$ peak were observed due to a mixture of the materials. This is consistent with the XPS results.

Fig. 5b shows the ex-situ sample consists of cubic Ni nanoparticles with an Fm-3m space group denoted by '♦' (PDF 01-077-8341). The observed diffraction planes were (111) and (200) corresponding to 44.7° 2θ and 52.1° 2θ respectively. In addition, hexagonal $NbSe_2$ (PDF 01-070-5612) with a P63/mmc space group was also observed. This is consistent with the TEM image in Fig. 2b where Ni nanoparticles are observed on the surface of the $NbSe_2$ nanoflowers. In addition, the ex-situ sample also had Se peaks (PDF 00-042-1425, space group = P3121) at 23.5 and 45.4° 2θ denoted by '*', as well as NiO (COD #1010093) peak at 43.5° 2θ denoted by '•'. This is consistent with the XPS results above, where the expected peaks of $NbSe_2$ were identified with additional NiO peaks.

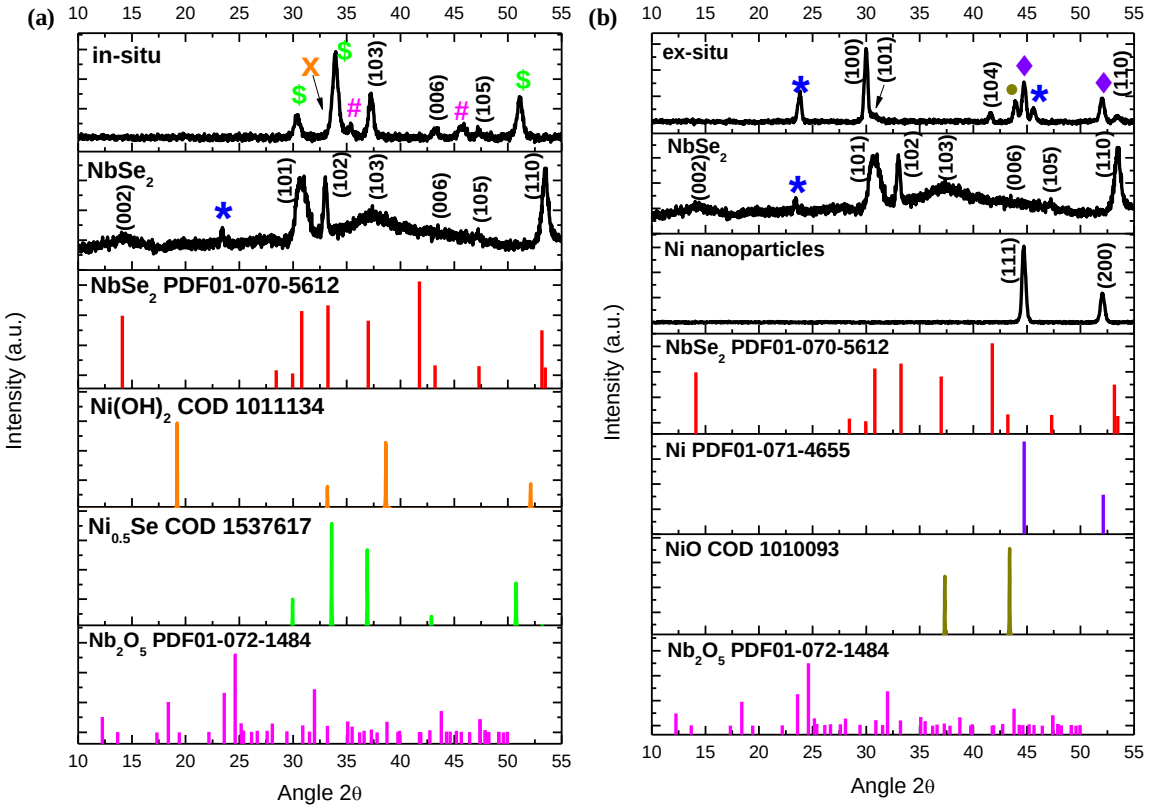

Fig. 5: XRD pattern of the Ni-decorated $NbSe_2$ nanomaterials formed using the (a) in-situ and (b) ex-situ method; where Se, $Ni_{0.5}Se$, $Ni(OH)_2$, NiO, Ni, and Nb_2O_5 peaks are denoted by '*', '$', 'x', '•', '♦', and '#', respectively.

The XRD pattern of the ex-situ samples showed the presence of excess Se, suggesting no bonding between the Ni and Se was formed during the decoration of $NbSe_2$. Whereas the in-situ samples showed no excess Se instead $Ni_{0.5}Se$ was present. Deng *et al.* used the extended X-ray absorption fine structure (EXAFS) technique to confirm that the Pt-S bond is more likely to occur than a Pt-Pt bond or Pt particles in the Pt-MoS_2 structure [49-51]. The in-situ method involved a dry mixture of the metal salts along with the as-synthesised $NbSe_2$ nanomaterial, then heated up under N_2 gas for some time. Heating the metal$(acac)_2$ salts causes the 'acac' to dissociate leaving the metal with a 2+ oxidation state to bond with the excess/vacant Se on the edges of the $NbSe_2$ layers. Hence the even distribution of the nanoparticles on the surface of the nanosheets and the formation of $Ni_{0.5}Se$. The ex-situ method resulted in Ni/NiO-$NbSe_2$ hybrid nanomaterial while the in-situ method resulted in a made-up of $Ni_{0.5}Se$/$Ni(OH)_2$-$NbSe_2$ hybrid nanomaterial. As such, this confirms the theory suggested by Sinha *et al.* that the formation of in-situ samples results in covalent bonds being formed i.e., $Ni_{0.5}Se$ [11, 12, 22].

3.3.3 Decoration of $NbSe_2$ using Pt

The Pt-decorated $NbSe_2$ samples were synthesised similarly to the Ni-decorated samples. TEM analysis showed that both the in-situ (Fig. 6a) and ex-situ (Fig. 6b) samples were made up of 2D nanosheets with Pt nanoparticles dispersed on the surface of the nanosheets. The distribution of the Pt nanoparticles on the surface of the nanosheets was similar to the Ni-decorated $NbSe_2$ samples formed using the in-situ and ex-situ methods. The Pt nanoparticles before the decoration process in the ex-situ were agglomerated (shown in Fig. S1). Additionally, the ex-situ method results in a random distribution of particles (a similar trend is observed in the Ni-decorated $NbSe_2$ ex-situ sample). As such, clusters of Pt nanoparticles are formed.

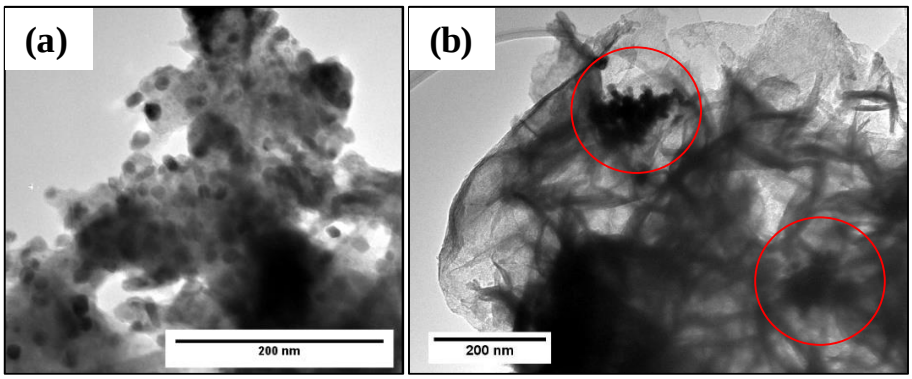

Fig. 6: TEM images of Pt-decorated $NbSe_2$ nanomaterials using the (a) in-situ and (b) ex-situ method.

Fig. 7 shows the XPS survey spectra of both the in-situ and ex-situ samples. Both the spectra contained the expected species Pt, Nb, Se, C, and O, where O is due to oxidation of the samples and C the capping agent used in the synthesis [31]. The Pt 4f XPS spectrum has three possible chemical states namely, metallic Pt^0 with binding energies at 71.5 and 74.8 eV, Pt^{2+} (PtO) at 72.9 and 76.2 eV, and Pt^{4+} ($PtSe_2$ or PtO_2) at 73.6 or 74.2, respectively [47, 54]. Fig. 8a shows the Pt 4f XPS spectrum of the in-situ sample. The in-situ sample showed the presence of two Pt^{2+} peaks at 72.3 ($4f_{7/2}$) and 75.5 eV ($4f_{5/2}$). These were attributed to PtO [53], this was also confirmed by the presence of the metal oxide in the O 1s spectrum (Fig. S3c). Fig. 8b shows the Pt 4f XPS spectrum of the ex-situ sample. The spectrum is deconvoluted into two peaks contributed by Pt^0 ($4f_{7/2}$) at 70.4 eV and Pt^{4+} ($4f_{5/2}$) at 73.4 eV. This indicates the presence of metallic Pt which is consistent with the Pt nanoparticles used to decorate $NbSe_2$ in the ex-situ method and Pt^{4+} for PtO_2. The oxide is further confirmed by the presence of the metal oxide in the O 1s XPS spectrum (Fig. S3d). Furthermore, Fig. 8e and f show that both the in-situ and ex-situ Nb 3d XPS spectra have three peaks composed of Nb^{4+} $3d_{5/2}$ (203.0 eV), Nb^{5+} $3d_{5/2}$ (206.9 eV) and Nb^{5+} $3d_{3/2}$ (209.3 eV). The Nb^{4+} peak corresponds to $NbSe_2$ whereas the Nb^{5+} peaks correspond to Nb_2O_5 [30]. And lastly, the Se 3d XPS spectrum for both samples were fitted to two characteristic peaks of Se^{2-} at 53.8 eV ($3d_{3/2}$) and 53.0 eV ($3d_{5/2}$) [47, 48]. This confirms the presence of $NbSe_2$ nanomaterial within both the in-situ and ex-situ samples.

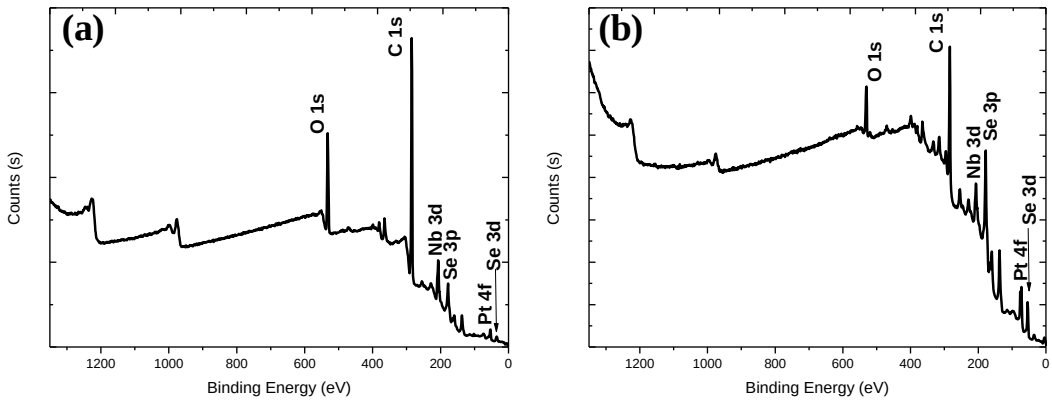

Fig. 7: XPS survey spectra of Pt-decorated $NbSe_2$ nanomaterials when varying the synthetic method (a) in-situ and (b) ex-situ.

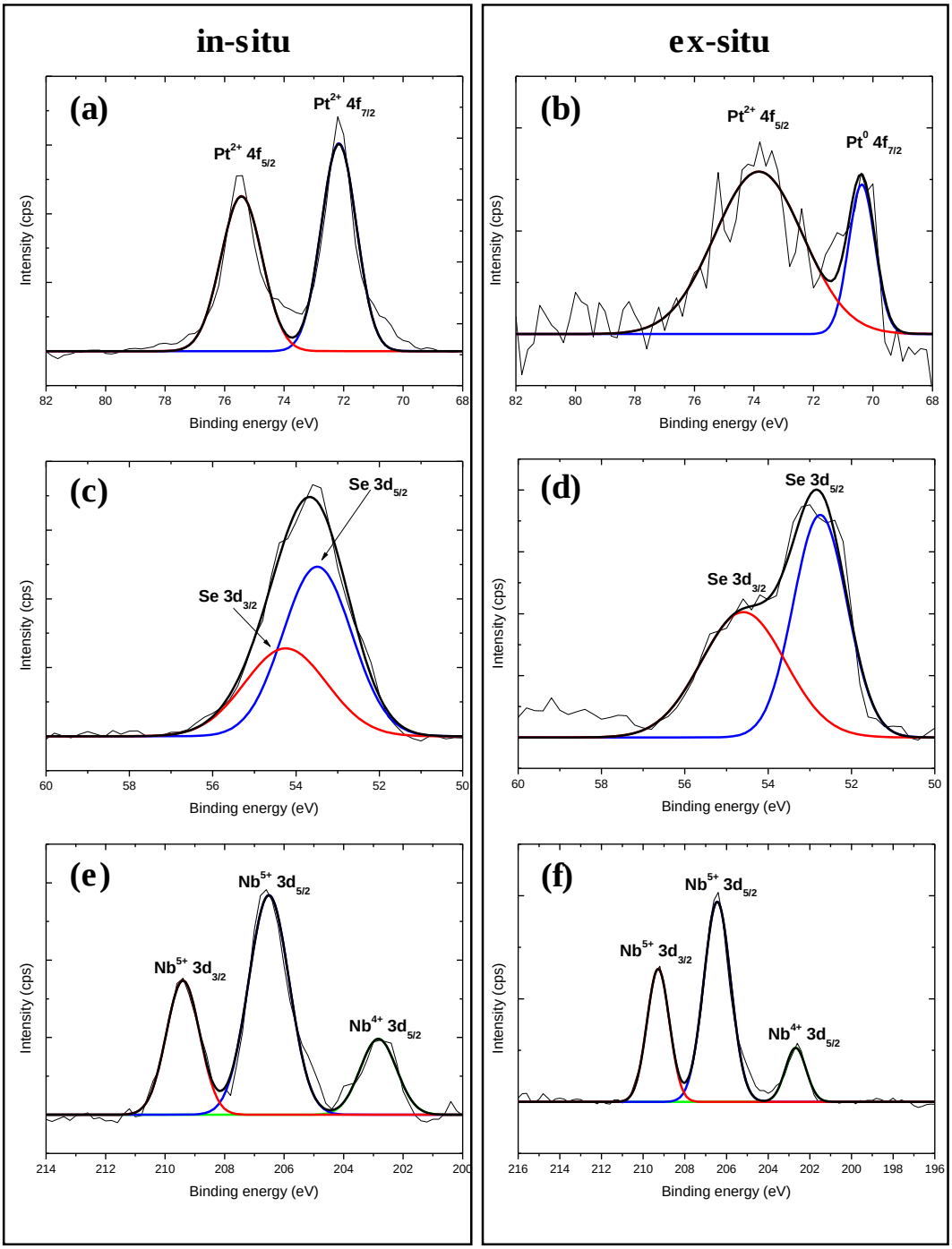

Fig. 8: (a) and (b) Pt 4f, (c) and (d) Se 3d, (e) and (f) Nb3d XPS core-level spectra for the in-situ and ex-situ Pt-decorated $NbSe_2$ nanomaterials.

XRD was used to confirm the phase, composition, and crystallinity of the in-situ and ex-situ Pt-decorated $NbSe_2$ nanomaterials. Fig. 9a shows that the in-situ sample contains the hexagonal $NbSe_2$ (PDF 01-070-5612) and PtO (COD #1522314) denoted by 'ϕ'. These results are consistent with the XPS results above. In addition, no excess Se peaks were observed which is in agreement with the XPS results where the Se $3d_{3/2}$ peak in the in-situ sample was not as

prominent as the one in the ex-situ sample. Fig. 9b shows that the ex-situ sample contains hexagonal $NbSe_2$ (PDF 01-070-5612) with a P63/mmc space group and cubic Pt (PDF 01-087-0640) nanoparticles with a Fm-3m space group denoted by 'α'. This confirms the results obtained from the TEM analysis. There were also additional peaks of Se (PDF 00-042-1425, space group = P3121) at 23.5 and 52.0° 2θ denoted by '*', as well as PtO_2 (COD #1537410) peaks at 41.6 and 43.9° 2θ denoted by 'β' due to oxidation on the surface of the nanomaterial. Both in-situ and ex-situ samples have some oxidation on the surface due to the presence of Nb_2O_5.

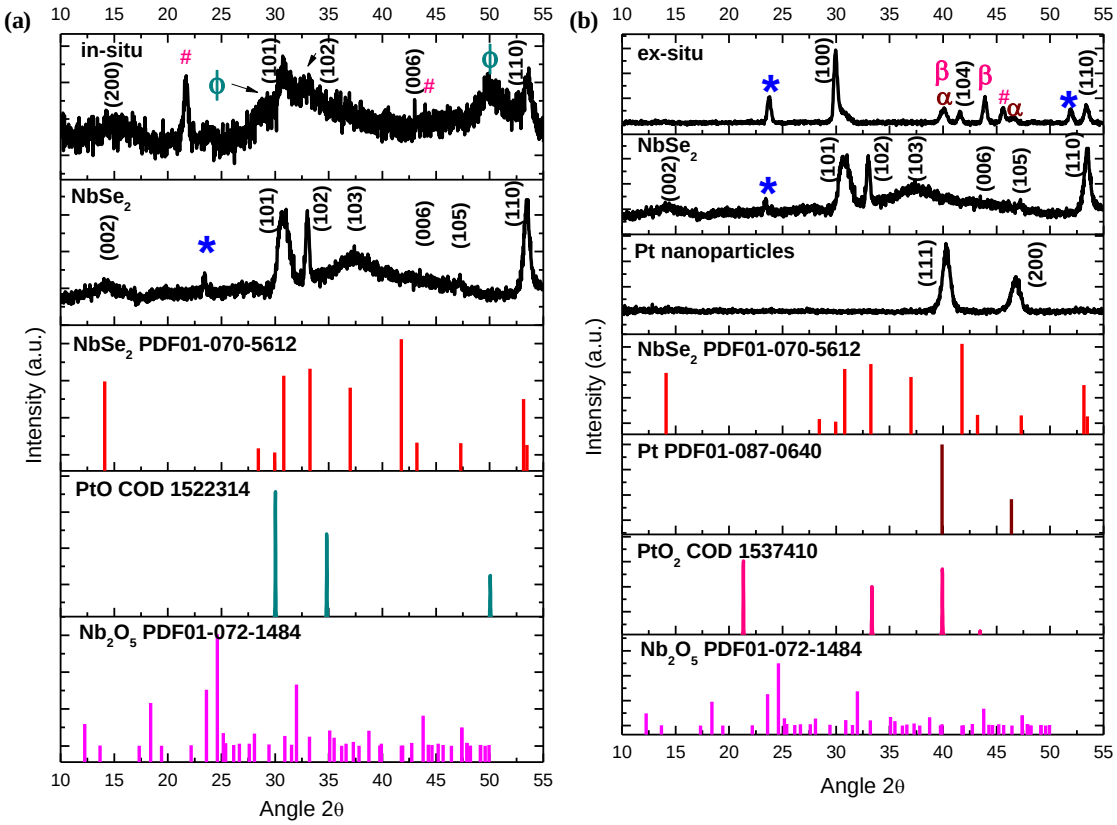

Fig. 9: XRD patterns of the Pt-decorated $NbSe_2$ nanomaterials using the (a) in-situ and (b) ex-situ method; where PtO, Pt, PtO_2, Nb_2O_5, and Se peaks are denoted by 'ϕ', 'α', 'β', '#', and '*', respectively.

Like the Ni-decorated in-situ sample, the Pt-decorated $NbSe_2$ in-situ sample resulted in a metal oxide (PtO) on the surface of $NbSe_2$ and the product being a PtO-$NbSe_2$ binary hybrid nanomaterial as well. The ex-situ sample, on the other hand, resulted in 0D Pt nanoparticles onto the surface of 2D $NbSe_2$ with some surface oxidation (PtO_2 and Nb_2O_5) instead. Therefore, also forms a Pt/PtO_2-$NbSe_2$ binary hybrid material. As such, this confirms Sinha *et al.* theory.

They predicted that the formation of ex-situ samples resulted in the weak van der Waals forces between the 0D and 2D material and covalent bonds in in-situ samples [11, 12, 22].

3.3.4 Decoration of $NbSe_2$ using Pt and Ni

$NbSe_2$ was also decorated by 10% wt. Pt / 10% wt. Ni using only the in-situ method. Fig. 10a shows the TEM analysis of the nanomaterial and it was made up of 2D $NbSe_2$ nanoflowers with particles on the surface. XPS analysis was performed to further understand the surface compositions and valence of the as-prepared nanomaterial. Fig. 10b shows the XPS survey of the samples with the following species C, O, Nb, Se, Ni, and Pt detected. Fig. 10c shows the Pt 4f core-level spectrum has two Pt^{2+} peaks at 72.6 ($4f_{7/2}$) and 75.9 eV ($4f_{5/2}$) assigned to PtO [53]. Fig. 10d shows the Ni 2p core-level spectrum, where the Ni $2p_{1/2}$ was deconvoluted to two peaks, satellite (denoted as 'sat.') at 880 eV and Ni^{2+} at 873 eV. In addition, the Ni $2p_{3/2}$ was also deconvoluted into the satellite and Ni^{2+} peaks at 861 and 856 eV, respectively. Ni^{2+} indicates the formation of NiO [32]. Fig. S4b shows the O 1s XPS spectrum further confirming the presence of metal oxides due to PtO and NiO. Fig. 10e and f show the Nb 3d and Se 3d XPS spectra containing two peaks each found in the pristine $NbSe_2$ sample, respectively.

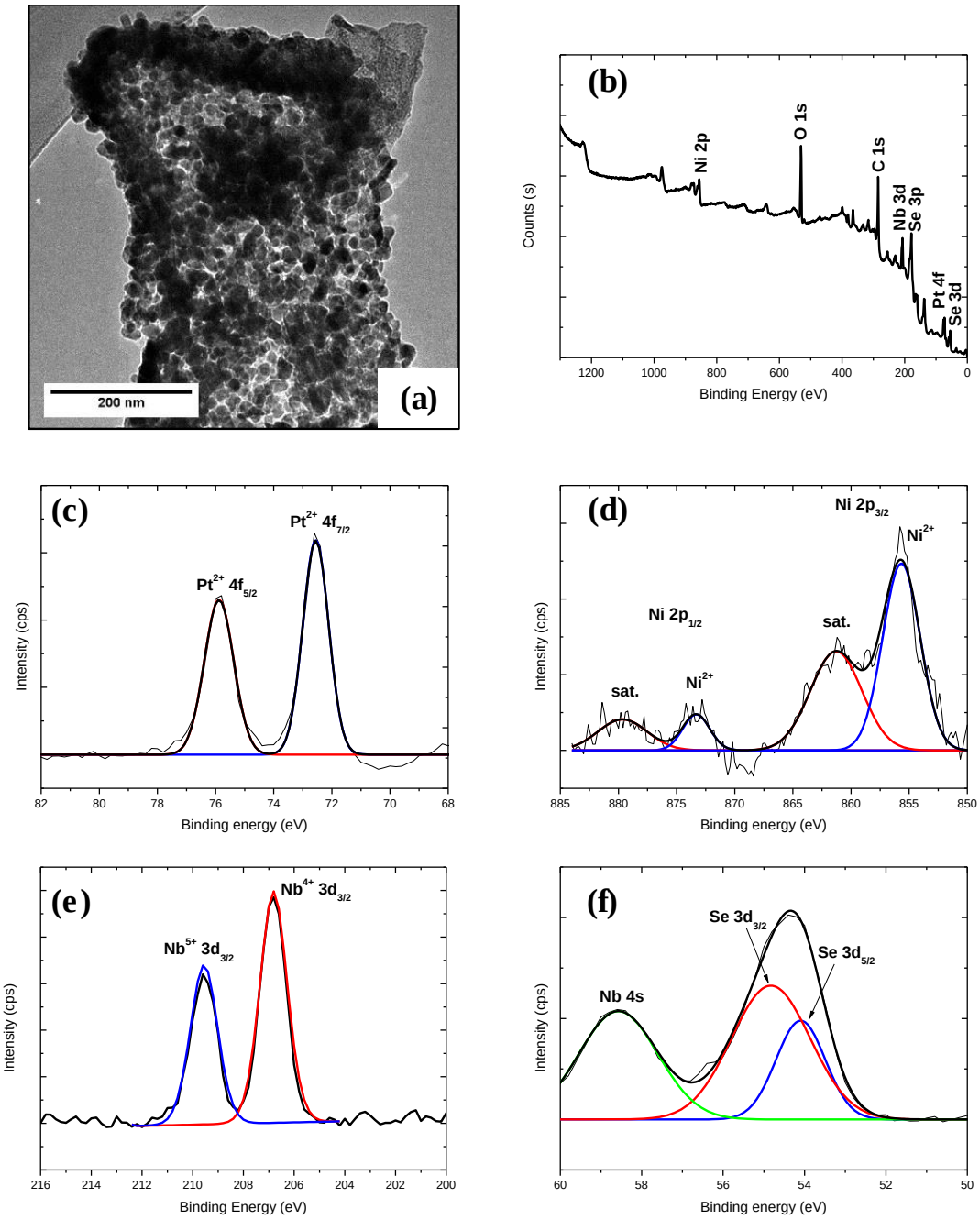

Fig. 10: (a) TEM image, XPS (b) survey spectrum, and XPS (c) Pt 4f, (d) Ni 2p, (e) Nb 3d, (f) Se 3d core-level spectra of $NbSe_2$ decorated by 10% wt. Pt / 10% wt. Ni (* denotes Se, $ denotes Ni, x denotes NiO and # denotes Nb_2O_5).

Fig. 11 shows the XRD pattern of the 10% wt. Pt / 10% wt. Ni decorated $NbSe_2$ nanomaterial, this technique was used to investigate the samples' phase, composition, and crystallinity. The XRD pattern shows the presence of $NbSe_2$ (PDF 01-070-5612) peaks namely, (100), (102), (103), (006), and (105). In addition, the sample also showed the presence of NiO (COD #1010093) peaks at 37.3 and 43.3° 2θ denoted by '•', and PtO (COD #1522314) peaks at 30.2

and 50.1 ° 2θ denoted by 'ϕ'. The sample also showed some oxidation due to Nb_2O_5 (PDF 01-072-1484), denoted by '#'. These results are in agreement with the XPS results. As such, the decoration of $NbSe_2$ using 10% wt. Pt / 10% wt. Ni resulted in the formation of PtO/NiO-$NbSe_2$ hybrid nanomaterial.

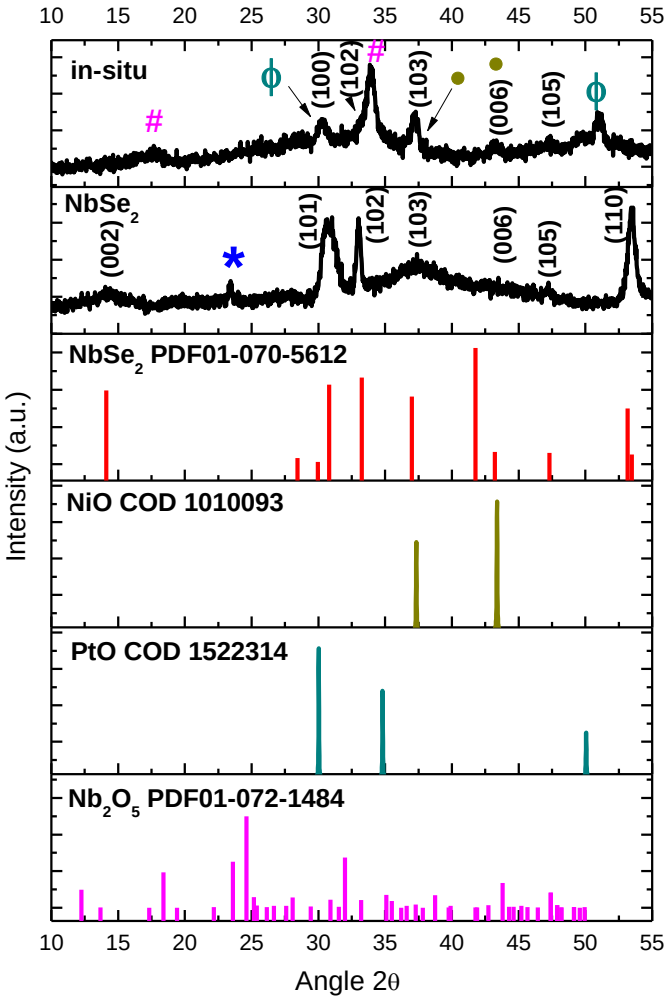

Fig. 11: XRD pattern of the $NbSe_2$ decorated by 10% wt. Pt / 10% wt. Ni nanomaterial using the in-situ method; where Se, NiO, PtO, and Nb_2O_5 peaks are denoted by '*', •', 'ϕ', and '#', respectively.

3.4. Electrochemical characterisation

The HER activity of the $NbSe_2$ was evaluated. Fig. 12a shows the LSV polarisation curve at a scan rate of 2 mV/s. As expected, the Pt/C electrocatalyst exhibited the highest activity with an onset potential (97 mV) compared to $NbSe_2$ (686 mV). At more negative potentials, the H_2 bubbles increased vigorously at the surface of the electrode causing the current density to

increase sharply [31]. To deliver a current density of 10 mA/cm^2, $NbSe_2$ exhibited a much lower overpotential of 839 mV. Fig. 12b shows the Tafel plots calculated from the fitted polarisation curves. The Tafel slope was calculated from the Tafel equation shown below:

$$\eta = b \log j + a$$

where η is the overpotential, b is the Tafel slope, and a is the Tafel constant. The Tafel slope reveals the intrinsic activity of the electrocatalyst as well as the reaction mechanism [31]. The value of the Tafel slope is determined by the rate-limiting step of HER [55]. The measured Tafel slope for Pt/C is 77 mV/dec which was approximately two-fold the reported value of 30.6 mV/dec [56]. This illustrated that the HER process was dominated by the Volmer - Heyrovsky mechanism [57, 58]. Fig. 12(b) has the Tafel slope of $NbSe_2$ = 301 mV/dec which was higher than Pt/C at the value of 289 mV/dec, revealing a low catalytic activity. In this case, the rate-determining step was the Volmer step [47]. As such, this motivated us to enhance the activity of $NbSe_2$ by forming hybrids.

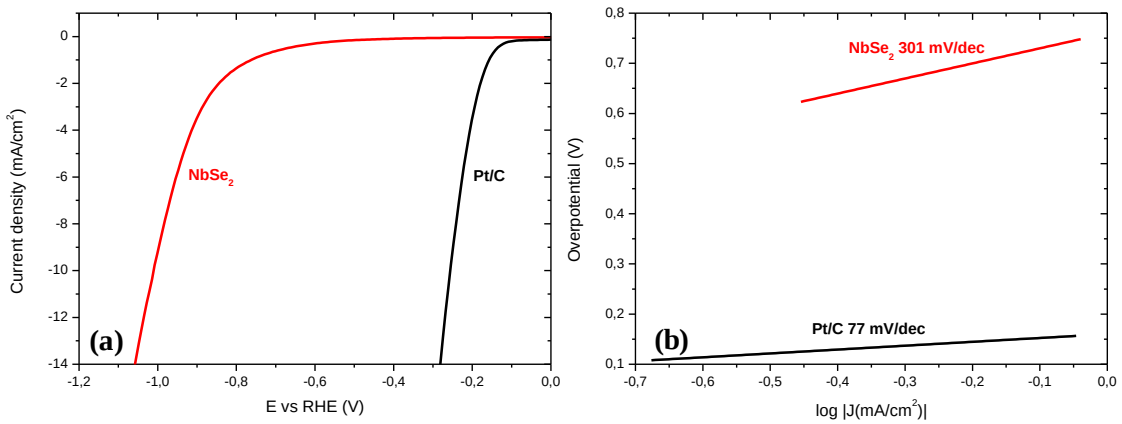

Fig. 12: (a) Polarisation curves of $NbSe_2$ nanomaterial and Pt/C, and (b) Tafel plots of $NbSe_2$ nanomaterial and Pt/C.

The HER activity of Ni-decorated $NbSe_2$ nanoflowers was evaluated. Fig. 13a shows that the $Ni_{0.5}Se/Ni(OH)_2$-$NbSe_2$ (in-situ) and Ni/NiO-$NbSe_2$ (ex-situ) samples exhibit a superior HER performance compared with $NbSe_2$ with extremely lower overpotentials of 795 mV and 741 mV (to deliver a current density of 10mA/cm^2), respectively. In addition, Fig. 13b shows that the $Ni_{0.5}Se/Ni(OH)_2$-$NbSe_2$ and Ni/NiO-$NbSe_2$ Tafel slopes are consistent with the overpotential trend with the value of 140 and 118 mV/dec, respectively.

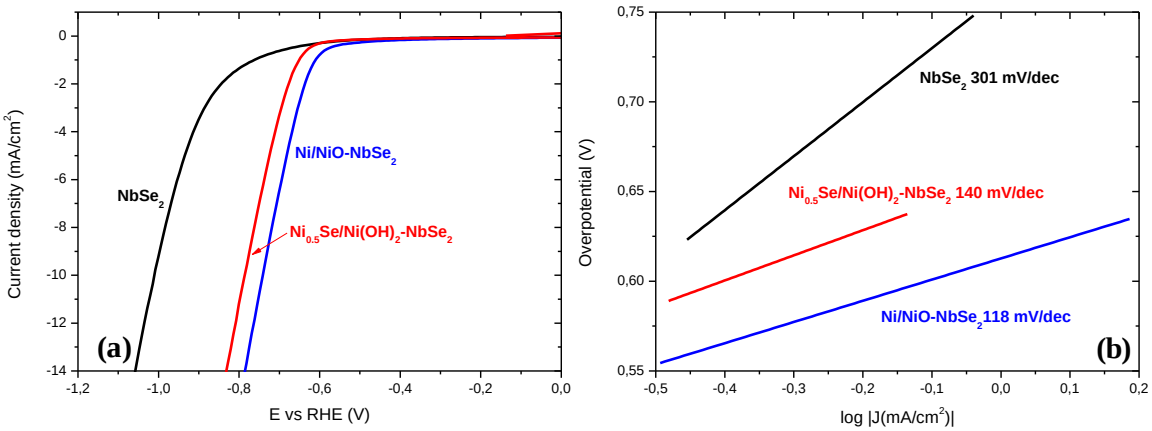

Fig. 13: (a) Polarisation curves, and (b) Tafel plots of the Ni-decorated $NbSe_2$ nanomaterials compared with the pristine $NbSe_2$.

For the Pt decorated $NbSe_2$, Fig. 14a shows the polarisation curves of PtO-$NbSe_2$ (in-situ) and Pt/PtO_2-$NbSe_2$ (ex-situ) nanomaterials, they resulted in much lower overpotentials of 551 and 501 mV compared to $NbSe_2$ (to deliver a current density of 10mA/cm^2), respectively. Fig. 14b shows the same trend was observed with the Tafel slopes of 67 and 60mV/dec for PtO-$NbSe_2$ and Pt/PtO_2-$NbSe_2$ nanomaterials, respectively.

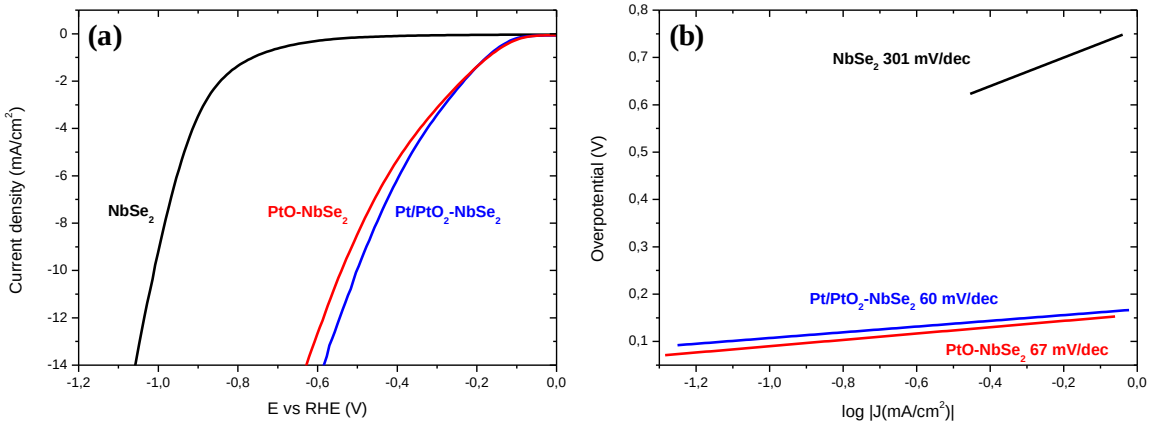

Fig. 14: (a) Polarisation curves, and (b) Tafel plots of the Pt-decorated $NbSe_2$ nanomaterials compared with bare $NbSe_2$.

Lastly, $NbSe_2$ nanoflowers was decorated with 10% wt. Pt / 10 % wt. Ni. Fig. 15a shows a further improvement in the HER performance with an overpotential of 398 mV to produce a current density of 10 mA/cm^2 compared to the pristine $NbSe_2$. The same was observed with the Tafel slope of 69 mV, shown in Fig. 15b.

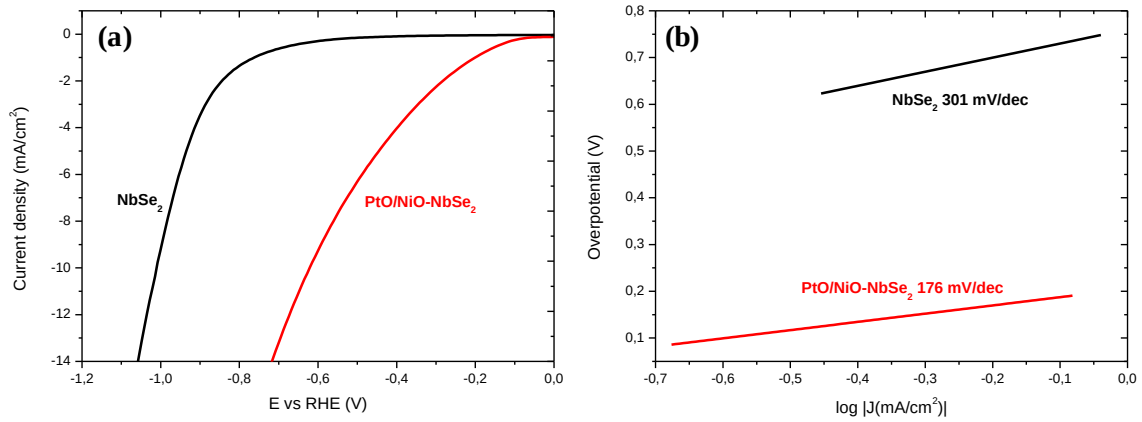

Fig. 15: (a) Polarisation curves, and (b) Tafel plots of $NbSe_2$ decorated with 10% wt. Pt /10% wt. Ni nanomaterial compared with bare $NbSe_2$.

Another significant factor is the exchange current density (j_0) which reveals the electrochemical rate of the reaction of the catalyst at equilibrium i.e., how fast the reaction occurs intrinsically. The exchange current density can be calculated from the Tafel equation when the overpotential is equal to zero [31, 47]. The higher the exchange current density, the better the electrocatalyst performance in the generation of H_2 [47, 59]. Table 2 indicates that Pt/PtO_2-$NbSe_2$ nanomaterial has the highest exchange current density and $NbSe_2$ with the lowest exchange current density compared to the other nanomaterials. The trend shows that the Ni-decorated $NbSe_2$ electrocatalysts (Ni/NiO-$NbSe_2$ > $Ni_{0.5}Se$/$Ni(OH)_2$-$NbSe_2$) have similar exchange current density values. Moreover, the Pt-decorated $NbSe_2$ electrocatalysts (Pt/PtO_2-$NbSe_2$ > PtO-$NbSe_2$) also have similar current density values. And lastly, the $NbSe_2$ decorated with 10% wt Pt and 10% wt Ni electrocatalysts (PtO/NiO-$NbSe_2$) exchange current density value was somewhere in between the Ni- and Pt-decorated electrocatalysts. This trend is consistent with the LSV and Tafel slope results. However, Pt/C was expected to have the highest exchange current density value compared to all the electrocatalysts, but the value lies slightly below the Pt-decorated $NbSe_2$ electrocatalysts. The tailing of the LSV may be the reason for this trend. The exchange current density trend was as follows: Pt/PtO_2-$NbSe_2$ > PtO-$NbSe_2$ > Pt/C > PtO/NiO-$NbSe_2$> Ni/NiO-$NbSe_2$ > $Ni_{0.5}Se$/$Ni(OH)_2$-$NbSe_2$> $NbSe_2$.

Table 2: Electrocatalytic parameters of decorated $NbSe_2$ electrocatalysts in comparison to bare $NbSe_2$ and Pt/C electrocatalyst

Sample	**η (mV)**	**η_{10} (mV)**	**b (mV/dec)**	**j_0 (mA/cm^2)**	**R_{ct} (Ohm)**	**C_{dl} (mF/cm^2)**
$NbSe_2$	686	1017	301	0.579	202	3.00
Ni/NiO-$NbSe_2$	562	741	118	0.637	96	3.03
$Ni_{0.5}Se$/$Ni(OH)_2$-$NbSe_2$	615	795	140	0.632	196	3.56
Pt/PtO_2-$NbSe_2$	97	501	60	1.459	59	11.5
PtO-$NbSe_2$	97	551	67	1.300	35	14.4
PtO/NiO-$NbSe_2$	157	617	176	0.754	64	3.62
Pt/C	97	256	77	0.846	n/a	n/a

To investigate the HER kinetics, EIS measurements were conducted at an applied overpotential of 1.4 V. The equivalence circuit shown in Fig. 16c was fitted to the Nyquist plots. The Nyquist plots also indicate whether there is an improvement in the performance of the electrocatalyst [47]. This improvement is identified by a smaller R_{ct} value which is favourable to fast charge transfer kinetics [31]. Fig. 16a shows the Nyquist plots, the trend R_{ct} was as follows: Pt/PtO_2-$NbSe_2$ < PtO-$NbSe_2$ < PtO/NiO-$NbSe_2$ < Ni/NiO-$NbSe_2$ < $Ni_{0.5}Se$/$Ni(OH)_2$-$NbSe_2$ < $NbSe_2$. Furthermore, it has been reported that there is a proportional relationship between the electrochemically active surface area (ECSA) and the number of active sites which can be calculated using the electrochemical double-layer capacitance (C_{dl}) [31, 60]. Fig. 16b shows the linear relationship between the current density and the potential scan rate, where the slope is C_{dl}. Ideally, the trend of the C_{dl} values is in agreement with the inverse of the R_{ct} trend. This is in agreement with the results presented in Table 2. Fig. S5 shows the CVs of all the synthesised nanomaterials in this study at different scan rates (10, 15, 20, 25, 30, 40 mV/s). The CVs show the regular rectangular feature of an electrical double-layer capacitor. ECSA can be calculated by dividing the C_{dl} value of the electrocatalyst by the specific capacitance (Cs) from the literature [61]. For Cs, various values ranging from 20 – 80 μF/cm^2 are reported where most researchers use the median value of 40 μF/cm^2 [61-64]. The ECSA values of the electrocatalysts in this study are summarised in Table S1. where a Cs value of 40 μF/cm^2 was used in the calculations. Pt/PtO_2-$NbSe_2$ electrocatalyst has the highest ECSA value of 70.6 cm^2 and $NbSe_2$ with the lowest value of 14.7 cm^2. Stability studies were performed on the Pt/PtO_2-$NbSe_2$ electrocatalyst since it was the best-performing electrocatalyst by performing the

chronoamperometry studies. Fig. 16d shows the chronoamperometry profile, when a potential of 500 mV was applied the current density drastically decreased. After ~1 h, the current density gradually increases for a further 2 h. This is an indication that the Pt/PtO_2-$NbSe_2$ continues to generate more current the longer it is used.

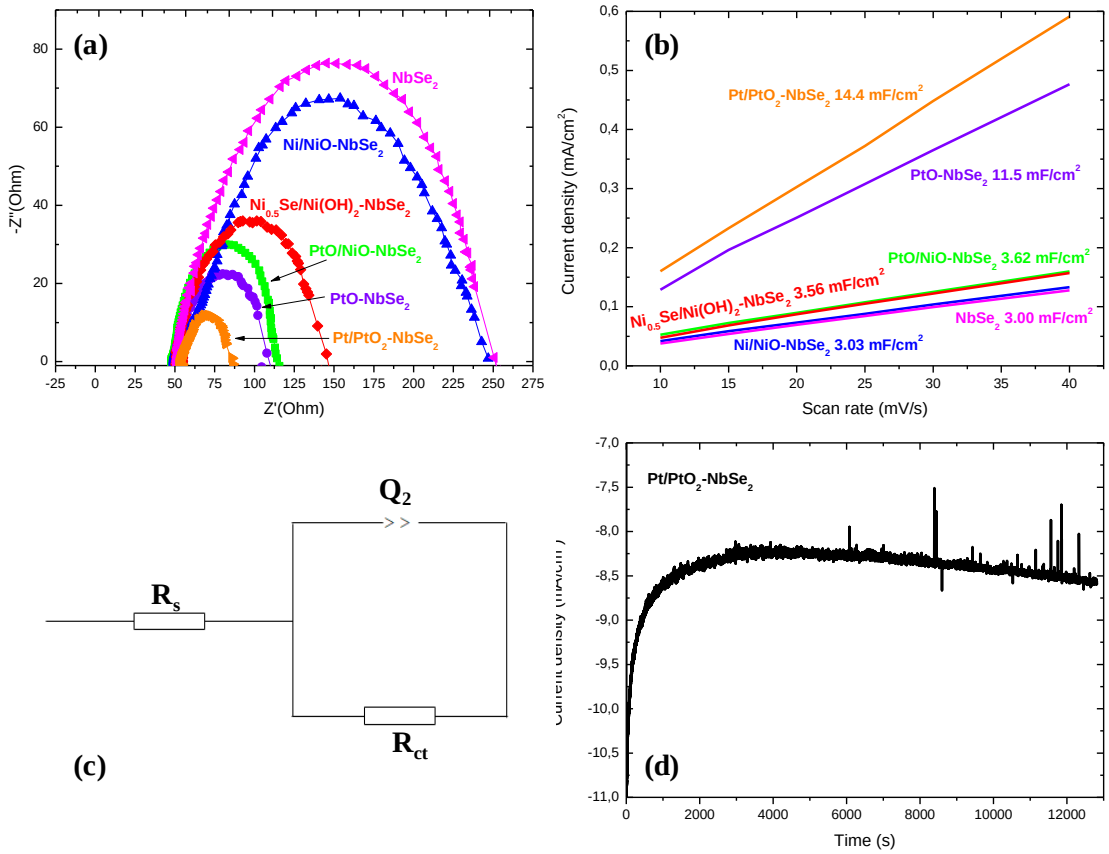

Fig. 16: (a) Nyquist plots, and (b) exchange current density (j_0) of $NbSe_2$ compared to the resultant nanomaterials after the decoration of $NbSe_2$, (c) equivalence circuit fitted to the Nyquist plots nanomaterials synthesised, and (d) Chronoamperometry for Pt/PtO-$NbSe_2$ nanomaterial at 500 mV vs RHE applied potential and 13 000 s time scale.

Decorating 2D $NbSe_2$ nanoflowers with Ni- and Pt-based nanomaterials showed an enhancement in the electrocatalytic activity of $NbSe_2$ significantly. According to the volcano plot used to show the electrocatalytic activity of transition metals, Pt has the highest exchange current density indicating the highest activity [65, 66]. Therefore, the results obtained in the polarisation curves followed the trend in the volcano plot, with Pt-decorated $NbSe_2$ (Pt/PtO_2-$NbSe_2$ > PtO-$NbSe_2$) nanomaterials having a superior activity than Ni-decorated $NbSe_2$ (Ni/NiO-$NbSe_2$ > $Ni_{0.5}Se$/$Ni(OH)_2$-$NbSe_2$) nanomaterials. More specifically, the ex-situ samples seemed to have superior activity compared to the in-situ samples. The ex-situ samples

contained metallic nanoparticles; therefore, it is expected for them to be favoured in this case; following the volcano plot trend. Furthermore, 20% wt. of Pt was used in Pt-decorated $NbSe_2$ ex-situ and in-situ nanomaterials as compared to the other electrocatalysts where either a reduced amount of Pt was used (10% wt.) or none (20% wt. Ni). Minimal research has been done on the performance of $NbSe_2$ electrocatalysts for hydrogen production, especially under alkaline conditions. However, a more recent study by Luo *et al.* reported a ten times improvement of overpotential (@ 10 mA/cm^2) from $NbSe_2$ to $Pt_3Nb_2Se_8$ [67]. Herein, Pt/PtO_2-$NbSe_2$ hybrid nanomaterial showed double the improvement as compared to $NbSe_2$. The presence of the oxide inhibited the improvement.

3.5. Conclusion

2D TMDCs have been extensively studied in the electrocatalytic HER, however, due to their active sites being only on the edges, the activity of pure 2D TMDCs is not satisfactory i.e., MoS_2, WS_2, $MoSe_2$ and WSe_2. Therefore, in this study, the enhancement of the catalytic activity for in-plane $NbSe_2$ was investigated. Normally, high overpotentials are required in alkaline solutions due to the sluggish kinetics of the HER and this remains a challenge in the development of active and stable HER electrocatalysts in alkaline media. According to the results obtained, the Pt/PtO_2-$NbSe_2$ electrocatalyst (resulted from decorated $NbSe_2$ with Pt using the ex-situ method) presented the lowest overpotential at a current density of 10 mA/cm^2, Tafel slope, exchange current density, and R_{ct}, as well as the highest C_{dl} and ECSA. This is an indication that this process worked and has the potential to produce electrocatalysts that are comparable to Pt. We observed that the metallic Pt nanoparticles contributed best to the enhancement of $NbSe_2$ as the Pt/PtO_2-$NbSe_2$ electrocatalyst was the only catalyst that possessed zero-valent platinum as confirmed by the XPS results.

3.6. References

[1] R. Sukanya, D. C. da Silva Alves, C. B. Breslin, *J. Electrochem. Soc.*, 2022 169, 064504.

[2] J. Zhu, L. Hu, P. Zhao, L. Y. S. Lee, K.-Y. Wong, *Chem. Rev.*, 2020, 120, 851.

[3] S. Dresp, F. Dionigi, M. Klingenhof, P. Strasser, *ACS Energy Lett.*, 2019, 4, 933.

[4] Q. Cheng, C. Hu, G. Wang, Z. Zou, H. Yang, L. Dai, *J. Am. Chem. Soc.*, 2020, 142, 5594.

[5] Y. Yao et al., *J. Am. Chem. Soc.*, 2019, 141, 19964.

[6] S.-Y. Bae, J. Mahmood, I.-Y. Jeon, J.-B. Baek, *Nanoscale Horizons*, 2020, 5, 43.

[7] Q. Lu, Y. Yu, Q. Ma, B. Chen, H. Zhang, *Adv. Mater.*, 2016, 28, 1917.

[8] F. Wang, T. A. Shifa, X. Zhan, Y. Huang, K. Liu, Z. Cheng, C. Jiang, and J. He, *Nanoscale*, 2015, 7, 19764.
[9] H. Zhou et al., *Nat. Commun.*, 2016, 7, 12765.
[10] Q. Xiong, Y. Wang, P.-F. Liu, L.-R. Zheng, G. Wang, H.-G. Yang, P.-K. Wong, H. Zhang, H. Zhao, *Adv. Mater.*, 2018, 30, 1801450.
[11] X. Wang, A. Vasileff, Y. Jiao, Y. Zheng, S. Z. Qiao, *Adv. Mater.*, 2019, 31, 1803625.
[12] X. Y. Zhang, H. P. Li, X. L. Cui, Y. Lin, *J. Mater. Chem.*, 2010, 20, 2801.
[13] Y. Jiao, Y. Zheng, K. Davey, and S.-Z. Qiao, *Nat. Energy*, 2016, 1, 16130.
[14] X. Lu, W. L. Yim, B. H. R. Suryanto, C. Zhao, *J. Am. Chem. Soc.*, 2015, 137, 2901.
[15] T. Y. Chen, Y. H. Chang, C. L. Hsu, K. H. Wei, C. Y. Chiang, L. J. Li, *Int. J. Hydrogen Energy*, 2013, 38, 12302.
[16] R. Sukanya, T. N. Barwa, Y. Luo, E. Dempsey, C. B. Breslin, *Sustain.*, 2022, 14, 4079.
[17] S. Manzeli, D. Ovchinnikov, D. Pasquier, O. V. Yazyev, A. Kis, *Nat. Rev. Mater.*, 2017, 2, 17033.
[18] L. Sun, M. Gao, Z. Jing, Z. Cheng, D. Zheng, H. Xu, Q. Zhou, J. Lin, *Chem. Eng. J.*, 2022, 429, 132187.
[19] Y. Sun, K. Xu, Z. Wei, H. Li, T. Zhang, X. Li, W. Cai, J. Ma, H. J. Fan, Y. Li, *Adv. Mater.*, 2018, 30, 1802121.
[20] V. D. Nithya, *Int. J. Hydrogen Energy*, 2021, 46, 36080.
[21] Z. B. Ndala, S. S. Nkabinde, N. P. Shumbula, O. A. Makgae, T. Kolokoto, M. Ek, S. S. Gqoba, C. E. Linganiso, P. S. Mdluli, N. Moloto, *Appl. Sur. Sci.*, 612, 2023, 155971.
[22] S. Sinha, H. Kim, A.W. Robertson, *Mater. Today A.*, 2021, 12, 100169.
[23] K. S. Novoselov, A. Mishchenko, A. Carvalho, A. H. Castro Neto, *Science*, 2016, 353.
[24] M. Y. Li, C. H. Chen, Y. Shi, L. J. Li, *Mater. Today*, 2016, 19, 322e335.
[25] Q. Zeng, Z. Liu, *Adv. Electron. Mater.*, 2018, 4, 1700335.
[26] J. Sun, Y. Choi, Y. J. Choi, S. Kim, J. Park, S. Lee, J. H. Cho, *Adv. Mater.*, 2019, 31, 1803831.
[27] Y. T. Liu, X. D. Zhu, L. Pan, *Small*, 2018, 14, 1803632.
[28] P. T. Yin, S. Shah, M. Chhowalla, K. B. Lee, *Chem. Rev.*, 2015, 115, 2483e2531.
[29] B. Luo, G. Liu, L. Wang, *Nanoscale*, 2016, 8, 6904e6920.
[30] T. Kolokoto, V. Mashindi, R. Kadzutu-Sithole, Lerato F. E. Machogo-Phao, Z. B. Ndala, N. P. Shumbula, S. S. Nkabinde, G. N. Ngubeni, S. S. Gqoba, K. P. Mubiayi, N. Moloto, *RSC Adv.*, 2021, 11, 31159–31173.

[31] J. Zhang, Y. Wang, C. Zhang, H. Gao, L. Lv, L. Han, Z. Zhang, *ACS Sustainable Chem. Eng*. 2018, 6, 2231−2239.

[32] N. K. M. Safeer, C. Alex, R. Jana, A. Datta, N. S. John, *J. Mater. Chem. A*, 2022.

[33] B. Zhao, X. K. Ke, J. H. Bao, C. L. Wang, L. Dong, Y. W. Chen, H. L. Chen, *J. Phys. Chem. C*, 2009, 113, 14440–14447.

[34] M. A. Airo, F. Otieno, L. Mxakaza, A. Ipadeola, R. S. Kadzutu-Sithole, L. F. E. Machogo-Phao, C. Billing, M. J. Moloto, N. Moloto, *RSC advances*, 10 (65), 2020, 39509−39520.

[35] K. He, Z. Cao, R. Liu, Y. Miao, H. Ma, Y. Ding., *Nano Res*. 9, 2016, 1856–1865.

[36] T. Sun, L. Xu, Y. Yan, A. A. Zakhidov, R. H. Baughman, J. Chen, *ACS Catal*., 2016, 6, 1446–1450.

[37] M. Fingerle, S. Tengeler, W. Calvet, T. Mayer, W. Jaegermann, *J. Electrochem. Soc*., 2018, 165, H3148– H3153.

[38] X. Zheng, X. Han, H. Liu, J. Chen, D. Fu, J. Wang, C. Zhong, Y. Deng, W. Hu, *ACS Appl. Mater. Interfaces*, 2018, 10, 13675−13684.

[39] S. Anantharaj, J. Kennedy, S. Kundu, *ACS Appl. Mater. Interfaces*, 2017, 9, 8714−8728.

[40] I. H. Kwak, H. S. Im, D. M. Jang, Y. W. Kim, K. Park, Y. R. Lim, E. H. Cha, J. Park, *ACS Appl. Mater. Interfaces*, 2016, 8, 5327−5334.

[41] K. Xu, H. Ding, H. Lv, S. Tao, P. Chen, X. Wu, W. Chu, C. Wu, Y. Xie, *ACS Catal.* 2017, 7, 310−315.

[42] K. Xu, H. Ding, K. Jia, X. Lu, P. Chen, T. Zhou, H. Cheng, S. Liu, C. Wu, Y. Xie, Angew. Chem., Int. Ed. 2016, 55, 1710−1713.

[43] M. A. Peck, M. A. Langell, Chem. Mater., 2012, 24, 4483– 4490.

[44] A. F. Carley, S. Rassias, *Surf. Sci.*, 1983, 135, 35–51.

[45] H. A. E. Hagelin-Weaver, J. F. Weaver, G. B. Hoflund, G. N. Salaita, *J. Electron Spectrosc. Relat. Phenom.*, 2004, 134, 139–171.

[46] D. Boscher, C. J. Carmalt, I. P. Parkin, Eur. *J. Inorg. Chem.*, 2006, 1255–1259.

[47] Z. B. Ndala, N. P. Shumbula, S. Nkabinde, T. Kolokoto, S. Gqoba, C. Linganiso, N. Moloto, *Journal of Electroanalytical Chemistry*, 2022, 918, 116464.

[48] E.P. Mukhokosi, S.B. Krupanidhi, K.K. Nanda, *Sci. Rep.*,2017, 1, 1–10.

[49] J. Deng, H. Li, J. Xiao, Y. Tu, D. Deng, H. Yang, H. Tian, J. Li, P. Ren, X. Bao, *Energy Environ. Sci.*, 2015, 274404286.

[50] J. R. Chang, S. L. Chang, *J. Catal.*, 1998, 176, 42–51.

[51] J. H. Pazmino, C. S. Bai, J. T. Miller, F. H. Ribeiro, W. N. Delgass, *Catal. Lett.*, 2013, 143, 1098–1107.

[52] B. Yue, Y. Ma, H. Tao, L. Yu, G. Jian, X. Wang, X. Wang, Y. Lu, Z. Hu, *J. Mater. Chem.*, 2008, 18, 1747–1750.

[53] M. Gao, Z. Lin, J. Jiang, C. Cui, Y. Zheng, S. Yu, Chem. Eur. J. 2012, 18, 8423 – 8429.

[54] J. D. Cooper, V. P. Vitullo, D. L. Whalen, *J. Am. Chem. Soc.*, 1971, 93, 6296.

[55] Y. Li, H. Wang, L. Xie, Y. Liang, G. Hong, H. Dai, *J. Am. Chem. Soc.*, 2011, 133, 7296−7299.

[56] X. Wang, Y. V. Kolen'ko, X. Q. Bao, K. Kovnir, L. Liu, *Angew. Chem., Int. Ed.*, 2015, 54, 8188−8192.

[57] B. Conway, B. Tilak, *Electrochim. Acta*, 2002, 47, 3571−3594.

[58] N. Pentland, J. M. Bockris, E. Sheldon, *J. Electrochem. Soc.*, 1957, 104, 182−194.

[59] J. Yang, A.R. Mohmad, Y. Wang, R. Fullon, X. Song, F. Zhao, I. Bozkurt, M. Augustin, E.J. Santos, H.S. Shin, *Nat. Mater.*, 2019, 12, 1309–1314.

[60] C. Z. Yuan, Y. F. Jiang, Z. Wang, X. Xie, Z. K. Yang, A. B. Yousaf, A. W. Xu, *J. Mater. Chem. A*, 2016, 4, 8155−8160.

[61] P. Connor, J. Schuch, B. Kaiser, W. Jaegermann, *Z. Phys. Chem.*, 2020, 234, 979–994.

[62] C. C. L. McCrory, S. Jung, J. C. Peters, T. F. Jaramillo, *J. Am. Chem. Soc.*, 2013, 135, 16977.

[63] R. Boggio, A. Carugati, S. Trasatti, *J. Appl. Electrochem.*, 1986, 17, 828.

[64] M. J. Gira, K. P. Tkacz, J. R. Hampton, *Nano Converg.*, 2016, 3, 6.

[65] S. Gupta, M. K. Patel, A. Miotello, N. Patel, *Adv. Funct. Mater.*, 2020, 30, 1906481.

[66] W. Han, M. Li, Y. Ma, J. Yang, *Frontiers in Chemistry*, 2020, 8, 592915.

[67] M. Luo, T. Wu, S. Xu, R. Wang, F. Huang, *Chem. Commun.*, 2022, 58, 6204-6207.

Chapter 3

Supplementary information

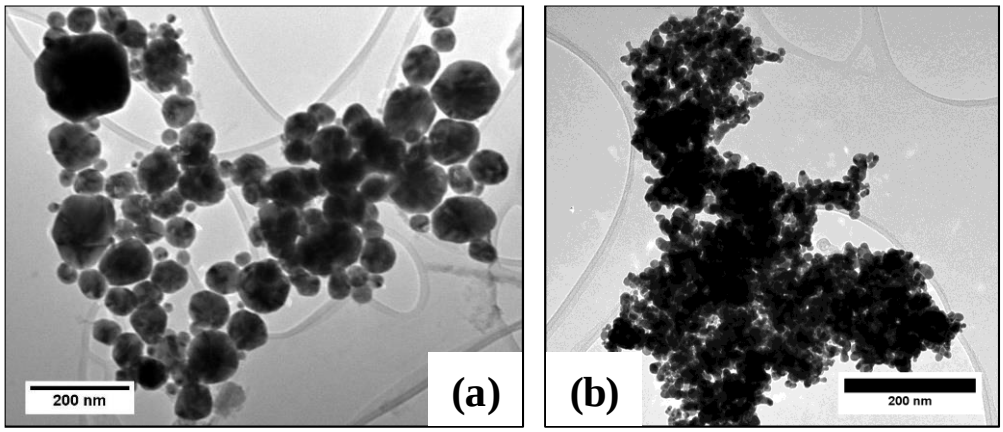

Fig. S1: TEM images of (a) Ni and (b) Pt nanoparticles used in the ex-situ method to produce $NiNbSe_2$ and $PtNbSe_2$, respectively.

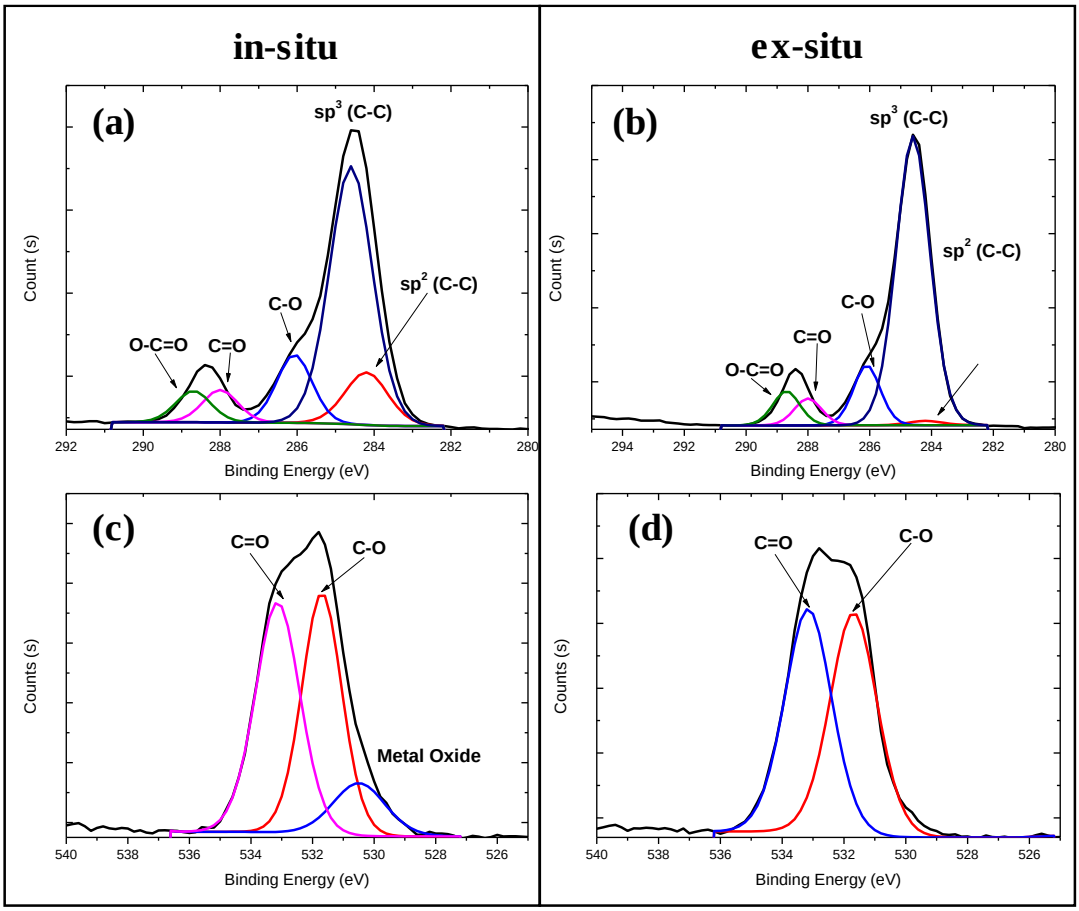

Fig. S2: (a) and (b) C1s, (c) and (d) O1s XPS core-level spectra of Ni-decorated $NbSe_2$ in-situ and ex-situ nanomaterials.

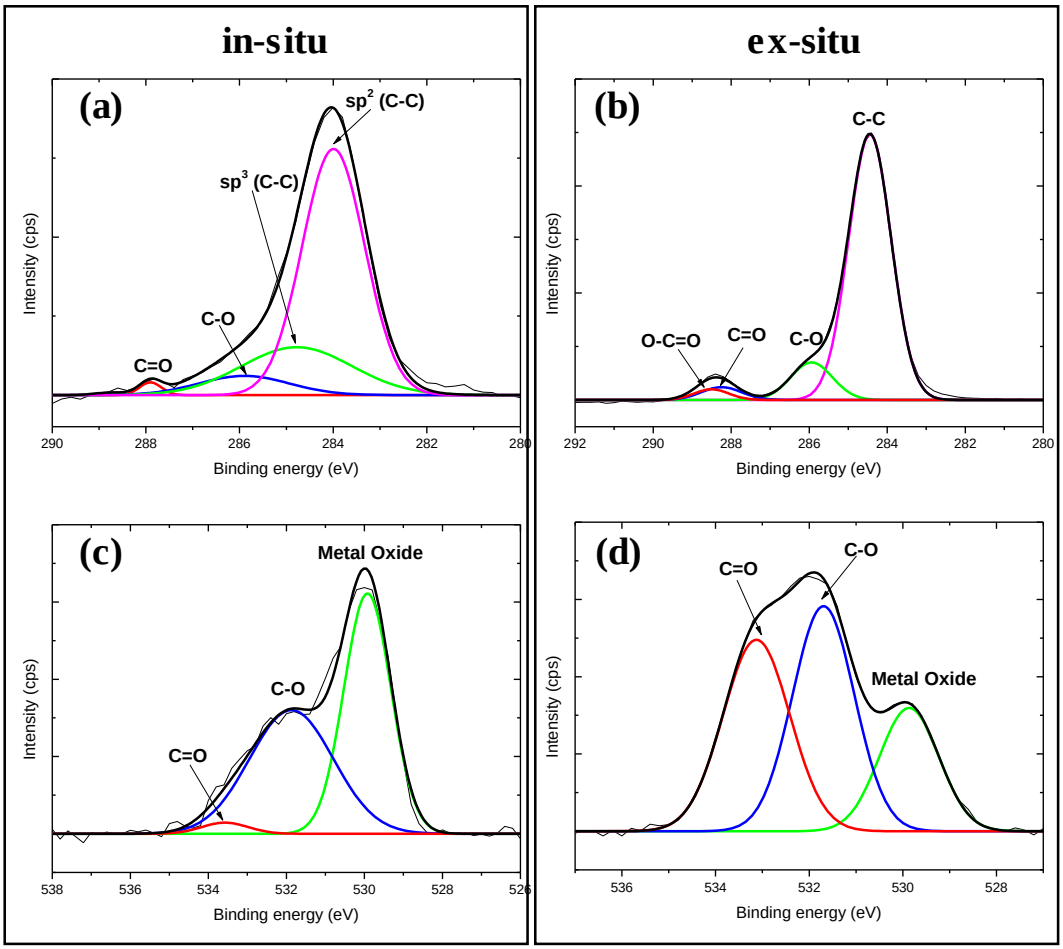

Fig. S3: (a) and (b) C1s, (c) and (d) O1s XPS core-level spectra of Pt-decorated $NbSe_2$ nanomaterials using the in-situ and ex-situ method.

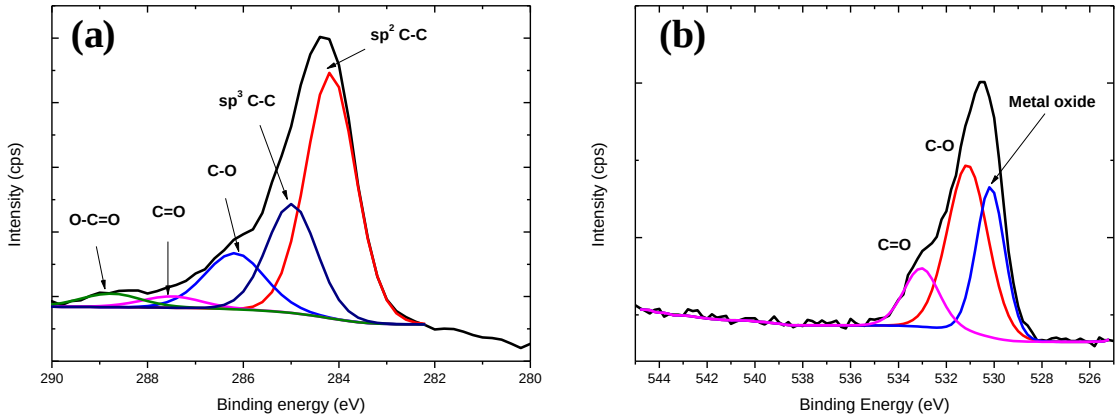

Fig. S4: (a) C1s and (b) O1s XPS core-level spectra of $NbSe_2$ decorated with 10% wt. Pt / 10% wt. Ni.

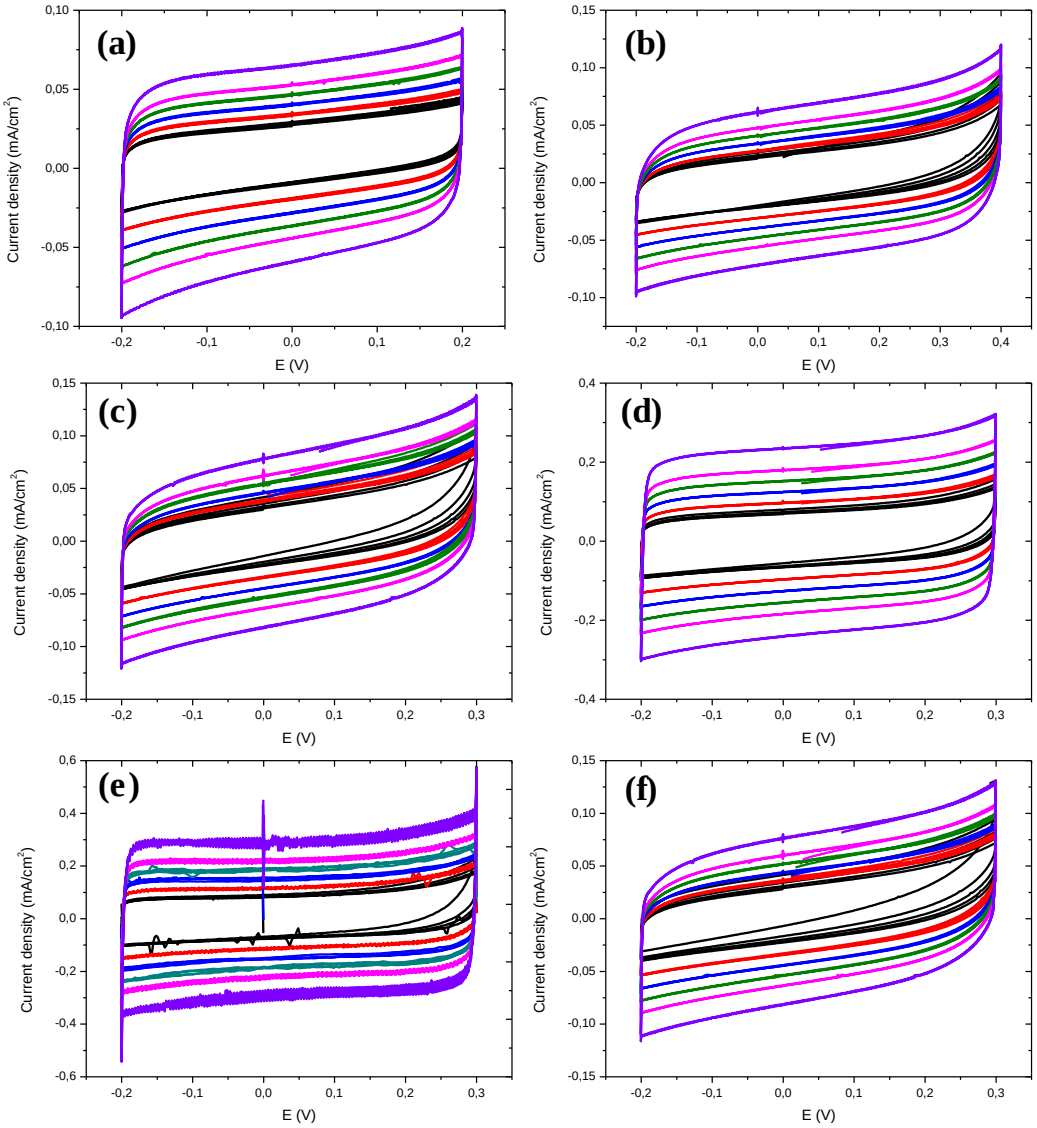

Fig. S5: (a) $NbSe_2$, (b) Ni/NiO-$NbSe_2$, (c) $Ni_{0.5}Se$/$Ni(OH)_2$-$NbSe_2$, (d) Pt/PtO_2-$NbSe_2$, (e) PtO-$NbSe_2$, (f) PtO/NiO-$NbSe_2$.

Table S1: ECSA of the decorated $NbSe_2$ in comparison to bare $NbSe_2$ calculated using electrochemical double-layer capacitance (C_{dl}) and specific capacitance (Cs) of 40 μF/cm^2

Sample	**ECSA (cm^2)**
$NbSe_2$	14.7
Ni/NiO-$NbSe_2$	17.4
$Ni_{0.5}Se$/Ni(OH)$_2$-$NbSe_2$	14.8
Pt/PtO_2-$NbSe_2$	70.6
PtO-$NbSe_2$	56.4
PtO/NiO-$NbSe_2$	17.7

Chapter 4

Co and Co/Pt decorated $NbSe_2$ as electrocatalysts for the hydrogen evolution reaction

4.1. Introduction

Considering the adverse effects of fossil fuels on the environment, it is urgent to explore abundant, environmentally friendly, sustainable, and renewable energy sources [1]. Many energy conversion technologies have been extensively used due to elevated efficiency and that they are environmentally-friendly, such as (i) proton exchange membrane fuel cells, (ii) water electrolyser, and (iii) unitised regenerative cells [2, 3]. The water electrolyser technology is of interest in this study, and the electrochemical processes play a crucial role in this system (oxygen evolution reaction (OER) at the anode and hydrogen evolution reaction (HER) at the cathode) [4-6]. Noble metal-based electrocatalysts (Pt, Ir, and Ru) are the most efficient [1]. However, the cost and limited resources of noble metals are issues that are unavoidable for widespread commercial applications [7]. As such, it is crucial to reduce the usage of noble metals or completely replace the noble metals with abundant, cheap, and highly reactive materials [1]. In the past, various non-noble metals have been used as alternatives to noble metal electrocatalysts, including transition metals (oxides, phosphides, chalcogenides, hydroxides, double perovskites, among others.) [8-14], nanocarbon hybrids [15], metal-free carbon-based materials [7, 16]. Transition metal dichalcogenides (TMDCs) as electrocatalysts in hydrogen production have been intensively researched due to their surface area, abundant edge states, and tunable electronic properties [17-22]. The large surface area is due to their atomically thin nature, thus providing more exposed catalytic active sites [23-26]. Furthermore, they provide a pathway for the formation of heterostructures with superior HER activity [27]. However, some TMDCs are not active enough due to poor intrinsic activity, low density of active sites, weak conductivity, or inert basal plane [28]. The inert basal plane can be used as a functional substrate to enhance the electrocatalytic activity of hybrid materials. As such, various strategies have been created to modulate the physiochemical and electronic properties of TMDC-based electrocatalysts and use their functional substrates to obtain fast reaction kinetics [28-35].

Co has emerged as an attractive non-noble metal for electrochemical reactions because of its catalytic performance and low prices of 72.82 – 48.07 €/kg [1]. Co is the 32nd most abundant element within Earth's crust. Recently, researchers discovered that Co-containing compounds supported on carbon-based materials enhance electrocatalyst activity with rich exposed active sites, high surface area and electrical conductivity, and fast mass transport [1, 36-41]. Qiao *et al.* formed a novel 2D Co-BDC/MoS_2 hybrid nanosheets through a facile sonication-assisted solution technique, resulting in good electrocatalytic activity and stability towards alkaline HER [6, 42]. In this case, the metallic 1T-MoS_2 and defects activated the inert basal plane by providing more active sites [6, 42]. Due to structural similarities between $NbSe_2$ and MoS_2, the HER electrocatalytic activity of $NbSe_2$ can also be enhanced using the same ideas. Herein, the focus was on the decoration of $NbSe_2$ using Co, and mixed metals of Pt and Co (10% wt each) towards HER were evaluated.

4.2. Methodology

4.2.1 Chemicals

Niobium(V) chloride ($NbCl_5$, 99%), selenourea (SU) (98%), oleylamine (OLA) (70%), hexane (95%), ethanol (96%), sodium borohydride ($NaBH_4$, ≥ 98%), potassium hydroxide (KOH, 90%), isopropanol (≥ 99.5%), Nafion (5 wt%), cobalt(II) bis(acetylacetonate) ($Co(acac)_2$, 95%), and platinum(II) bis(acetylacetonate) ($Pt(acac)_2$, 97%) were all purchased from Sigma-Aldrich.

4.2.2 Synthesis of $NbSe_2$

The 2D $NbSe_2$ nanoflowers were synthesised following the Kolokoto *et al.* heat-up colloidal synthesis procedure where the optimum conditions were using $NbCl_5$ and SU in OLA for 120 min at 320 ℃ under N_2 flow [43].

4.2.3 Decoration of $NbSe_2$ using the ex-situ method

In the ex-situ synthetic method, the reducing agent $NaBH_4$ and Co precursor ($Co(acac)_2$) in a 1:1 ratio was added to a degassed OLA in a three-necked round bottom flask. The reaction was carried out at 280 °C for 120 min. The readily synthesised nanoparticles were washed with hexane, followed by distilled water to remove excess/unreacted $NaBH_4$, and then dried and ready for characterisation. Once dried, the Co nanoparticles (20% wt) were mixed with the $NbSe_2$ and added to 1 mL of ethanol. The mixture was sonicated for 60 min then placed onto

a shaker at 180 rpm for 24 h. The mixture was then washed with hexane, dried, and ready for characterisation.

4.2.4 Decoration of $NbSe_2$ using the in-situ method

In the in-situ synthesis method, 10% wt. Co /10% wt. Pt ($M(acac)_2$, where M = Co or Pt) were mixed with the readily synthesised $NbSe_2$ and placed on a cylindrical steel reactor. The reactor was attached to an Ar gas line and loaded into a tubular furnace. The furnace was ramped at 2.5 °C.min^{-1} until it reached 100 °C, then held for 30 min at the same temperature to remove moisture. Then further ramped up at 2.5 °C. min^{-1} until it reached 350 °C and held for 120 min. The furnace and reactor were cooled to room temperature overnight, and the product was ready for characterisation.

4.2.5 Characterisation of the pristine $NbSe_2$ and the hybrid nanomaterials

The structure and phase of the powdered materials were determined using the Bruker MeasSrv (D2-205530)/D2-205530 diffractometer using secondary graphite monochromated CuKα radiation (λ = l 1.54184 Å) at 30 kV/30 mA. Measurements were taken using a glancing angle of incidence detector at an angle of 2°, for 2θ values over 10 – 90° in steps of 0.026° with a step time of 37 s, and at room temperature. X-ray photoelectron spectroscopy (XPS) measurements were performed with a Thermo ESCAlab 250Xi using monochromatic Al Kα (1486.7 eV) X-rays at a power of 300 W with a spot size of 900 mm. An FEI Spirit 120 kV transmission electron microscope (TEM) was operated at an accelerated voltage of 200 kV with a beam spot size of 20–100 nm in TEM mode and was also used to study the morphology of the samples. The samples were dispersed in hexane and drop-casted onto a lacey carbon copper grid. The solvent was then evaporated at room temperature.

4.2.6 Electrochemical characterisation

The Biologic SP 300 was used to investigate the electrochemical performance of HER in a three-electrode system. The measurements were performed in an alkaline solution of 0.1 M of KOH. The Ag/AgCl electrode was used as a reference electrode, the Pt wire as a counter electrode, and the working electrode made up of the hybrid nanomaterials' thin film on a glassy carbon electrode with a surface area of 0.07065 cm^2. The electrochemical performance of pristine $NbSe_2$ and Pt/C loaded onto the glassy carbon electrode was also measured for comparison. The thin films were formed by drop-casting about 10 uL of ink onto the glassy carbon electrode and left to dry at room temperature. The inks were formed by dissolving 2.2

mg of the sample and 1.6 mg of Vulcan in a mixture of 20 μL Nafion (5 wt.%) and 400 μL isopropanol and then sonicated for 1 h. The electrolyte was purged with argon for 30 min. This was followed by cyclic voltammetry (CV) measurements where the working electrode's potential was swept between -0.2 – 0.5 V vs RHE for 20 cycles at 100 mV/s. This process activates the surface of the electrocatalyst. The double layer was measured within the potential window of -0.2 – 0.4 V at various scan rates: 10, 15, 20, 25, 30, and 40 mV/s. The linear sweep voltammetry (LSV) was conducted at a scan rate of 2 mV/s. The electrochemical impedance spectroscopy measurements were recorded at a potential of -0.836 V vs RHE and a frequency range between 0.2 Hz and 100 kHz. The working electrode potentials vs Ag/AgCl were converted to the RHE scale using the equation below:

$$E_{RHE} = E_{Ag/AgCl} + 0.059pH + 0.0197$$

, where E_{RHE} is the measured potential and pH = 13.

4.3. Results and discussion

4.3.1 Decoration of $NbSe_2$ using Co-based nanoparticles

Two techniques were used to synthesise Co-decorated $NbSe_2$, namely the in-situ and ex-situ methods. The structure and morphology of the $NbSe_2$ sample were characterised in Chapter 3. Fig. 1 shows that the in-situ (Fig. 1a) and ex-situ (Fig. 1b) Co-decorated $NbSe_2$. The morphology was made up of 2D $NbSe_2$ nanosheets with Co nanoparticles on the surface of the sheets. The Co nanoparticles on the surface of the nanosheets in the in-situ method (Fig. 1a) are smaller in size and monodispersed compared to the ex-situ method (Fig. 1b) that were unevenly distributed and polydispersed with minor agglomeration. Fig. S1 shows the TEM image of polydispersed Co nanoplates used to decorate $NbSe_2$ in the ex-situ method.

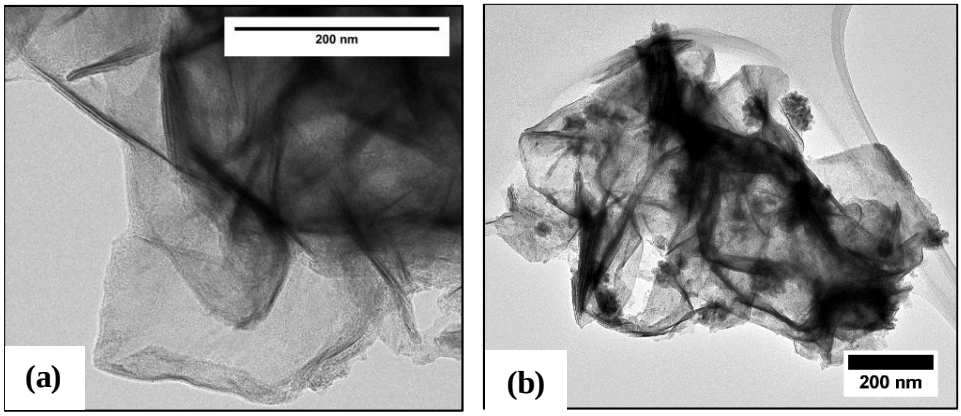

Fig. 1: TEM images of Co-decorated $NbSe_2$ nanomaterials using the (a) in-situ method and (b) ex-situ method.

X-ray photoelectron spectroscopy (XPS) analysis was performed to investigate further the surface compositions and valency of the as-prepared in-situ and ex-situ Co-decorated $NbSe_2$ nanomaterials. The XPS survey spectra of both nanomaterials in Fig. 2 contained the following species Co, Nb, Se, C, and O, where O was due to the oxidation of the samples and C due to the capping agent used in the synthesis [44]. Fig. 3a shows the Co 2p core-level spectrum of the in-situ sample, which decomposed into two distinct peaks and two weal satellites. The spin-orbit was assigned to Co oxides corresponding to Co $2p_{1/2}$ and Co $2p_{3/2}$ located at 795.9 and 780.8 eV, respectively. The Co $2p_{1/2}$ was deconvoluted into peaks contributed by Co^{2+} at 799.7 eV, Co^{3+} at 796.5 eV, and satellite peak denoted as 'sat.' at 804.8 eV [45]. Similarly, the Co^{2+}, Co^{3+}, and satellite peaks can also be seen from Co $2p_{3/2}$ at 782.5, 780.6, and 788.2 eV, respectively. The satellite peaks near two spin doublet peaks further provide evidence of cobalt oxides [45-47]. Furthermore, Kong *et al.* synthesised $CoSe_2$ grown on carbon fiber paper and obtained similar results where the electron-binding energies of Co $2p_{3/2}$ were located at 778.4 eV and Co $2p_{1/2}$ at 793.3 eV without satellite peaks, which corresponds to Co^{2+} in $CoSe_2$ [48-50]. However, Smyrnioti *et al.* synthesised Co_3O_4 nanoparticles with similar XPS results. They noted that the energy difference of 15.1 eV between the Co $2p_{3/2}$ and Co $2p_{1/2}$ splitting is characteristic of the Co_3O_4 cubic phase [45]. The Co $2p_{1/2}$ and Co $2p_{3/2}$ peaks of the ex-situ sample were deconvoluted into peaks due to Co^{2+}, Co^{3+}, and satellite at 797.8, 796.4, and 804 eV ($2p_{1/2}$); and 782.4, 780.6, and 786.4 eV ($2p_{3/2}$), respectively (shown in Fig. 3b). The presence of the Co^{2+} peak in both samples indicated the formation of $CoSe_2$ [48-50]. In addition, a Co^0 peak located at 777.9 eV corresponds to the Co nanoparticles used to decorate $NbSe_2$ in the ex-situ method. The presence of the Co $2p_{1/2}$, Co $2p_{3/2}$, and satellite peaks further indicates Co_3O_4 oxide [45]. Fig. S2c and d show the O1s spectra of both the ex-situ and in-situ

samples. The O1s peak from the ex-situ and in-situ samples was deconvoluted to three peaks: C-O at 532 eV, C=O at 533 eV, and metal oxide at 530 eV. In this case, the C-O peak is attributed to O^{2-} from the oxygen lattice of Co_3O_4 [45]. The C=O peak at higher binding energy indicates adsorbed oxygen (O_2) onto the surface through the capping agent used to synthesise $NbSe_2$; this can be attributed to defective sites [45, 51-53]. Fig. S2a and b show the C 1s XPS spectra of the in-situ and ex-situ samples consisting of C-C (sp^3), C-O, O-C=O, and C=O. Fig. 3c and d show the Nb 3d XPS spectra for the in-situ and ex-situ nanomaterials, respectively. The spectra of the in-situ sample contained three peaks Nb^{4+} $3d_{3/2}$ (206.0 eV), Nb^{5+} $3d_{5/2}$ (206.9 eV) and Nb^{5+} $3d_{3/2}$ (209.3 eV). The Nb^{4+} peak can be attributed to $NbSe_2$, whereas the Nb^{5+} peaks to Nb_2O_5 [43]. Boscher *et al.* obtained the same results [43, 54]. The spectra of the ex-situ sample contained four peaks Nb^{4+} $3d_{3/2}$ (203.0 eV), Nb^{4+} $3d_{5/2}$ (206.0 eV), Nb^{5+} $3d_{5/2}$ (206.9 eV) and Nb^{5+} $3d_{3/2}$ (209.3 eV). Similarly, the Nb^{4+} peaks correspond to the $NbSe_2$ and Nb^{5+} to Nb_2O_5. Fig. 3e and f show the in-situ and ex-situ Se 3d core level spectra. The spectra were deconvoluted into two peaks, $3d_{3/2}$ at 53.8 eV and $3d_{5/2}$ (53.0 eV), corresponding to the $NbSe_2$ and or $CoSe_2$ [48, 49, 54, 55].

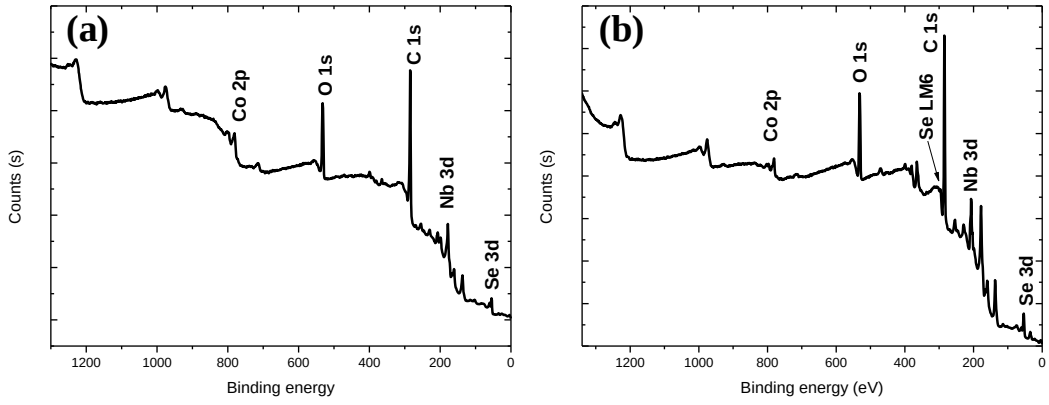

Fig. 2: XPS survey spectra of Co-decorated $NbSe_2$ nanomaterials when varying the synthetic method (a) in-situ and (b) ex-situ.

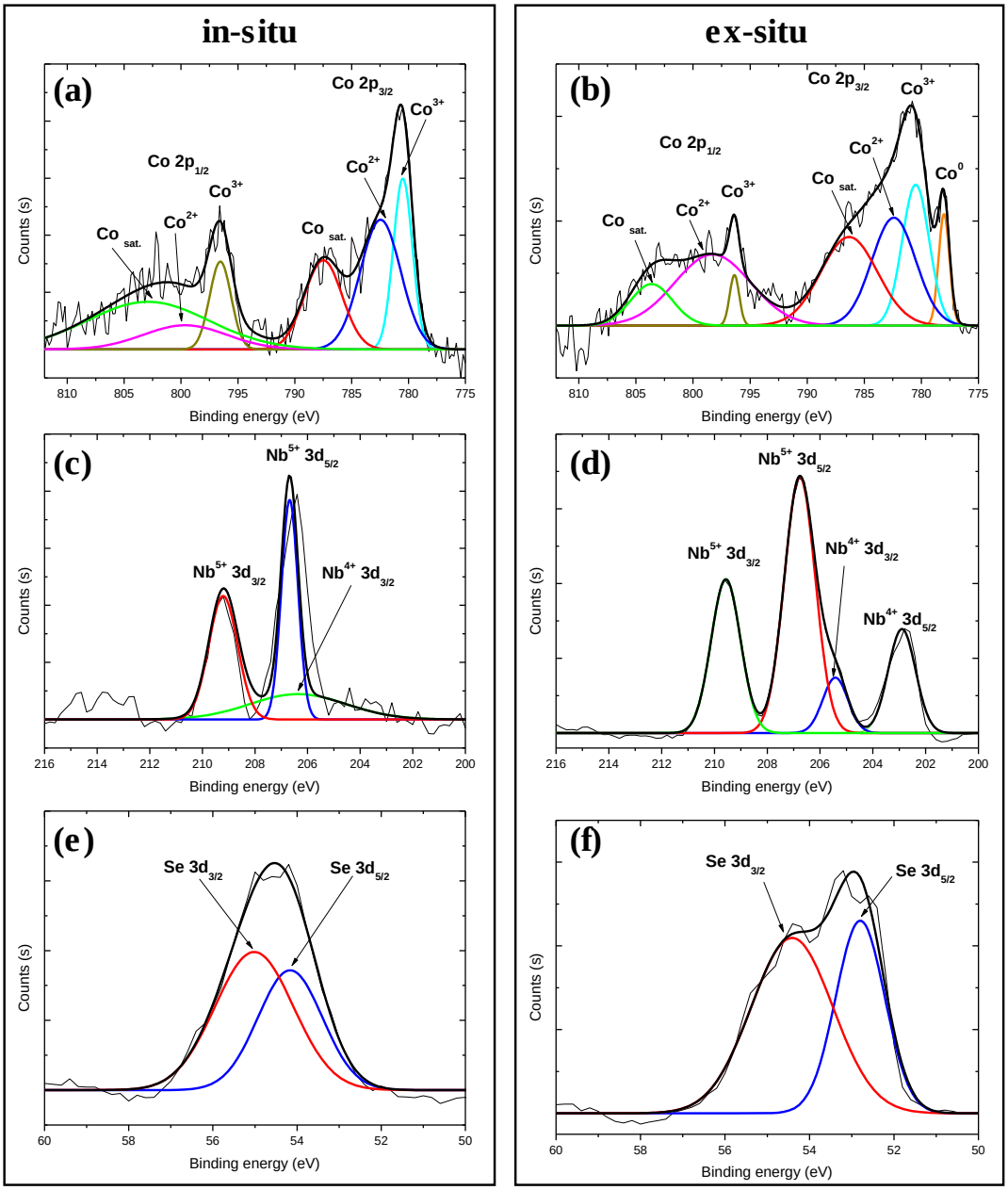

Fig. 3: (a) and (b) Co 2p, (c) and (d) Nb 3d, (e) and (f) Se 3d XPS core-level spectra for the in-situ and ex-situ Co-decorated $NbSe_2$ nanomaterials.

Fig. 4 shows the XRD patterns of the in-situ and ex-situ Co-decorated $NbSe_2$ samples further to confirm their phase, composition, and crystallinity. These samples were compared to the pristine 2D $NbSe_2$. Fig. 4a shows that the in-situ sample consists of $NbSe_2$. In addition, Co_3O_4 (COD #1526734) peaks were observed at 31.4, 45.0 ° 2θ denoted by '∀' and $CoSe_2$ (COD #9012536) peaks at 34.3, and 51.8 ° 2θ denoted by 'ϕ'. Some overlapping of Co_3O_4 and $CoSe_2$ peaks with the $NbSe_2$ peak was observed due to a mixture of the materials. This is consistent with the XPS results. Fig. 5b shows that the ex-situ sample consists of cubic Co nanoparticles

with an Fm-3m space group denoted by '♦' (PDF 00-001-1259). The observed diffraction planes were (100) and (101), corresponding to 41.8 and 51.4 ° 2θ, respectively. In addition, hexagonal $NbSe_2$ (PDF 01-070-5612) with a P63/mmc space group was also observed. This corresponds to the TEM image in Fig. 1b, where Co nanoparticles are observed on the surface of the $NbSe_2$ nanoflowers. In addition, the ex-situ sample also had Se peaks (PDF 00-042-1425, space group = P3121) at 23.5 and 51.4 ° 2θ denoted by '*' and Co_3O_4 (COD #1526734) peak at 45.0° 2θ denoted by '∀' overlapping with the Nb_2O_5 peak. This corresponds to the XPS results above, where the expected peaks of $NbSe_2$ were identified with additional Co_3O_4 and Co peaks.

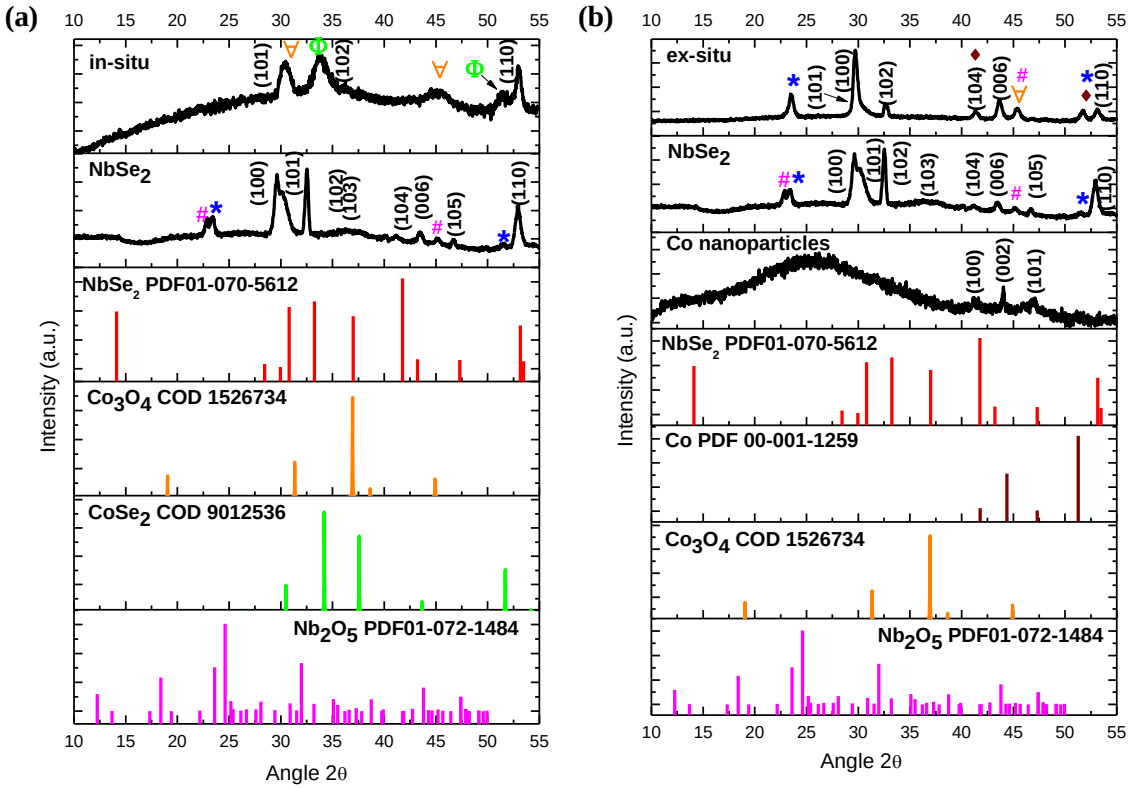

Fig. 4: XRD pattern of the Co-decorated $NbSe_2$ nanomaterials formed using the (a) in-situ and (b) ex-situ method; where Se, Co_3O_4, Co, and Nb_2O_5 peaks are denoted by '*', '∀', '♦', and '#', respectively.

The ex-situ method resulted in Co/Co_3O_4-$NbSe_2$ hybrid nanocrystals, while the in-situ method resulted in Co_3O_4/$CoSe_2$-$NbSe_2$ hybrid nanomaterial. Both the ex-situ and in-situ samples contain Co_3O_4. In addition, the ex-situ sample's XRD pattern showed the presence of excess Se, suggesting that no bonding was formed between the Co and Se during the decoration of

$NbSe_2$. Whereas the in-situ sample showed no excess Se; instead, $CoSe_2$ was present. During the in-situ process, the heated $Co(acac)_2$ salt caused the 'acac' to dissociate and the Co^{2+} ions to bond with the excess/vacant Se on the edges of the $NbSe_2$ layers. Hence the even distribution of the nanoparticles on the surface of the nanosheets and the formation of $CoSe_2$.

4.3.2 Decoration of $NbSe_2$ using Co/Pt

$NbSe_2$ was also decorated with 10% wt. Pt/10% wt. Co using only the in-situ method. Fig. 5a shows the TEM image of the resultant sample. The sample was made up of 2D $NbSe_2$ nanoflowers with particles on the surface. Fig. 5b shows the TEM image at a higher magnification of 50 nm.

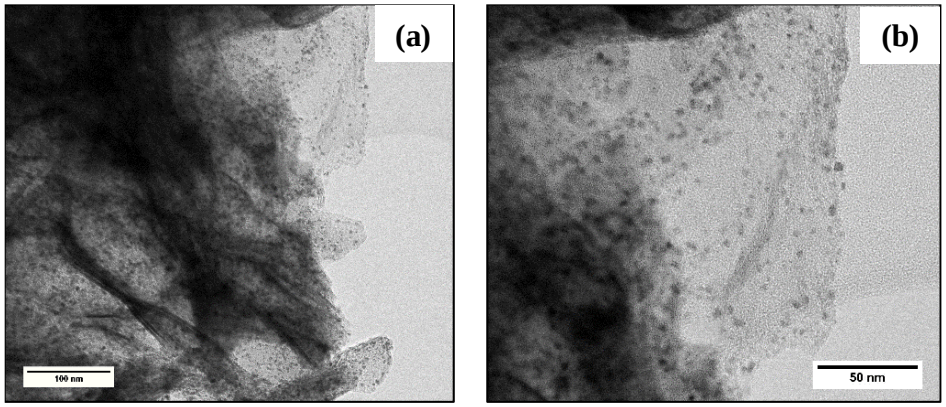

Fig. 5: TEM images of (a) $NbSe_2$ decorated with 10% wt. Pt / 10% wt. Co nanomaterial; ((b) same image at a higher magnification).

XPS analysis was performed to understand the composition and valency of the nanomaterial. Fig. 6a shows the XPS survey spectrum of the nanomaterial with the following species C, O, Nb, Se, Co, and Pt present. The Pt 4f XPS spectrum is known to have three possible chemical states, namely, metallic Pt^0 with binding energies at 71.5 and 74.8 eV, Pt^{2+} (PtO) at 72.9 and 76.2 eV, and Pt^{4+} ($PtSe_2$ or PtO_2) at 73.6 or 74.2, respectively [56, 57]. Fig. 5b shows the Pt 4f core-level spectrum has two peaks Pt^{2+} at 71.9 ($4f_{5/2}$) assigned to PtO and Pt^{4+} at 74.0 eV ($4f_{5/2}$) assigned to PtO_2 [58]. Fig. 6c shows the Co 2p core-level spectrum, where the Co $2p_{1/2}$ was deconvoluted to three peaks, satellite (denoted as 'sat.') at 803.0 eV, Co^{2+} at 798.8 eV and Co^{3+} at 794.7 eV. In addition, the Co $2p_{3/2}$ was also deconvoluted into the satellite and Co^{3+} peaks at 785.8 and 780.2 eV, respectively. Co $2p_{3/2}$ and Co $2p_{1/2}$ indicate the formation of Co_3O_4 and $CoSe_2$ [45, 48-50]. In addition, there is a Co^0 peak that can be attributed to metallic Co Fig. S3a shows the O 1s XPS spectrum, further confirming the presence of metal oxides due to PtO,

PtO_2, and Co_3O_4. Fig. 6d and e show the Nb 3d XPS spectra containing four peaks and Se 3d XPS spectra containing two peaks in the pristine $NbSe_2$ sample, respectively.

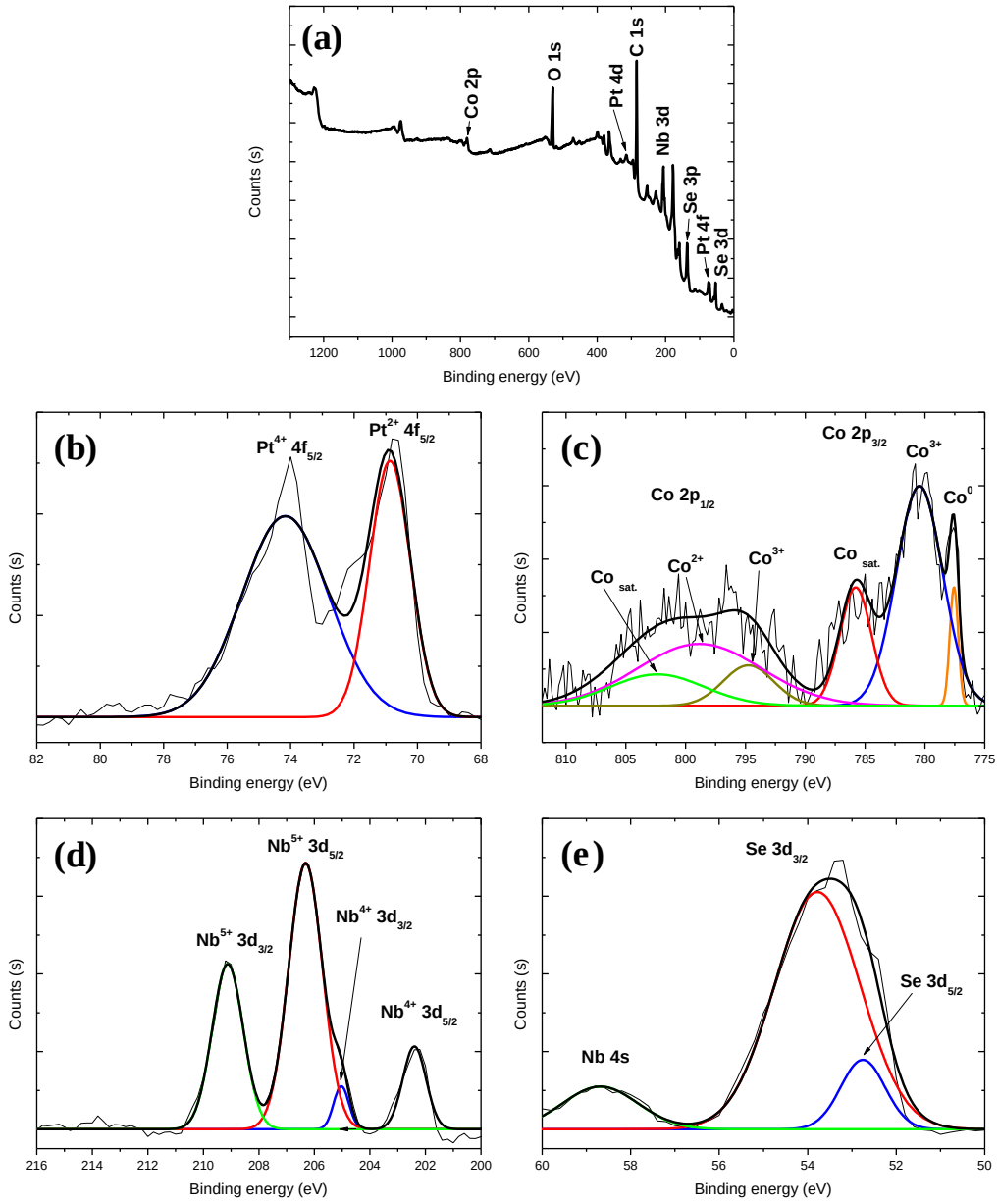

Fig. 6: XPS (a) survey spectrum, (b) Pt 4f, (c) Co 2p, (d) Nb 3d, (e) Se 3d core-level spectra.

XRD analysis of the $NbSe_2$ decorated with 10% wt. Pt / 10% wt. Co nanomaterial was performed to investigate the samples' phase, composition, and crystallinity. Fig. 7 shows the XRD pattern containing $NbSe_2$ (PDF 01-070-5612) peaks, namely, (100), (101), (102), (105), and (110). In addition, the sample also showed the presence of $CoSe_2$ (COD #9012536) peak at 34.1° 2θ denoted by 'ϕ', Co_3O_4 (COD #1526734) peak at 44.8° 2θ denoted by '$\forall$', PtO_2 (COD #1537410) peak at 40.0° 2θ denoted by 'β', and PtO (COD #1522314) peak at 33.6° 2θ

denoted by 'α'. These results are in agreement with the XPS results without metallic Co peaks. As such, the decoration of $NbSe_2$ using 10% wt. Pt / 10% wt. Co resulted in $Co_3O_4/CoSe_2/PtO/PtO_2$-$NbSe_2$ (COS/PTO-$NbSe_2$) hybrid nanomaterial.

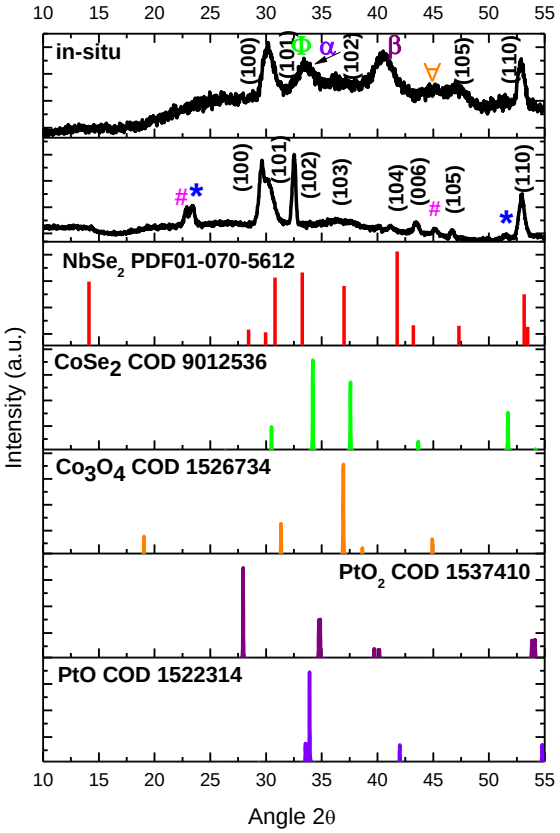

Fig. 7: XRD pattern of the $NbSe_2$ decorated by 10% wt. Pt /10% wt. Co nanomaterial using the in-situ method; where Co_3O_4, $CoSe_2$, PtO, and PtO_2 peaks are denoted by '∀', 'ϕ', 'α', and 'β', respectively.

4.4. Electrochemical characterisation

The HER activity of pristine $NbSe_2$ was evaluated in Chapter 3. This study assessed and compared the Co-decorated $NbSe_2$ electrocatalysts' HER activity to the pristine $NbSe_2$. Fig. 8a shows the LSV polarisation curves of Co/Co_3O_4-$NbSe_2$ (ex-situ) and $Co_3O_4/CoSe_2$-$NbSe_2$ (in-situ) electrocatalysts. Co/Co_3O_4-$NbSe_2$ and $Co_3O_4/CoSe_2$-$NbSe_2$ exhibited superior HER activity compared to pristine $NbSe_2$ with a lower overpotential of 707 and 964 mV (to deliver current density of 10 mA/cm^2), respectively. Fig. 8b shows the Tafel slopes of Co/Co_3O_4-$NbSe_2$ and $Co_3O_4/CoSe_2$-$NbSe_2$. The Tafel slope was calculated using the Tafel equation shown below:

$$\eta = b \log j + a$$

where η is the overpotential, b is the Tafel slope, and a is the Tafel constant. The intrinsic property of the electrocatalyst and the reaction mechanism can be determined from the Tafel slope value [51]. The Tafel slope of Co/Co_3O_4-$NbSe_2$ corresponds to the overpotential trend of 120 mV/dec. However, the Tafel slope of $Co_3O_4/CoSe_2$-$NbSe_2$ was expected to be lower than pristine $NbSe_2$, but the value lies higher than $NbSe_2$ due to the tailing effect of the LSV polarisation curve.

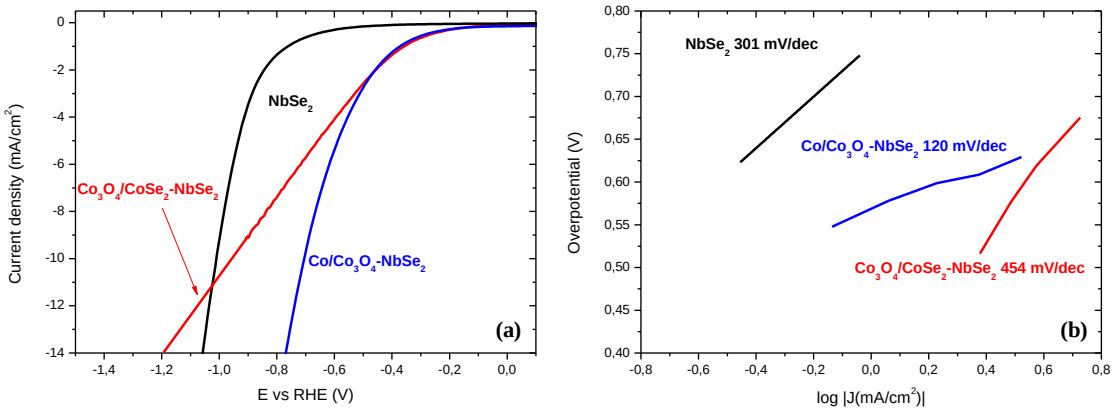

Fig. 8: (a) Polarisation curves and (b) Tafel plots of the Co-decorated $NbSe_2$ nanomaterials compared with the pristine $NbSe_2$.

Furthermore, $NbSe_2$ was decorated with 10% wt. Pt / 10% wt. Co. Fig. 9a shows an improvement in the HER activity with an overpotential of 769 mV (to produce a current density of 10 mA/cm^2) compared to pristine $NbSe_2$. Fig. 9b shows the same was obtained with a Tafel slope of 294 mV/dec.

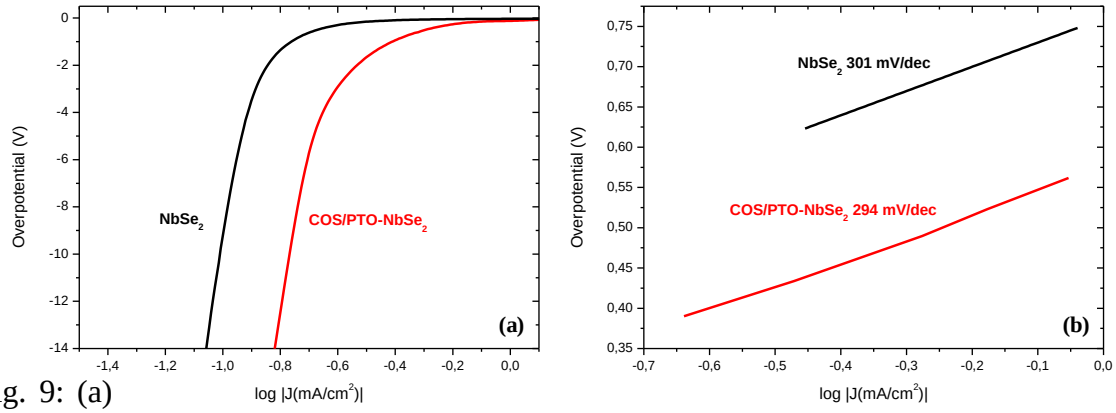

Fig. 9: (a) Polarisation curves and (b) Tafel plots of $NbSe_2$ decorated with 10% wt. Pt / 10% wt. Co nanomaterial compared with bare $NbSe_2$.

Exchange current density (j_0) is another significant parameter which reveals the electrochemical rate of reaction of the electrocatalyst at equilibrium [56, 59]. The exchange current density can be calculated from the Tafel equation when the overpotential equals zero. The exchange current density is directly proportional to the electrocatalyst performance in the generation of H_2 [56, 59]. Table 2 indicates that $Co_3O_4/CoSe_2$-$NbSe_2$ electrocatalyst has the lowest exchange current density. The trend is consistent with the LSV and Tafel slope results. However, Co/Co_3O_4-$NbSe_2$ was expected to be higher than the exchange current density of $NbSe_2$, but the value lies slightly above $NbSe_2$. The $NbSe_2$ decorated with 10% wt Pt /10% wt Co has an exchange current density value somewhere between Co/Co_3O_4-$NbSe_2$ and $Co_3O_4/CoSe_2$-$NbSe_2$. The exchange current density trend was as follows: Pt/C > $NbSe_2$ > Co/Co_3O_4-$NbSe_2$ > COS/PTO-$NbSe_2$ > $Co_3O_4/CoSe_2$-$NbSe_2$.

Table 2: Electrocatalytic parameters of decorated $NbSe_2$ electrocatalysts in comparison to pristine $NbSe_2$ and Pt/C electrocatalyst

Sample	**η (mV)**	**η_{10} (mV)**	**b (mV/dec)**	**j_0 (mA/cm^2)**	**R_{ct} (Ohm)**	**C_{dl} (mF/cm^2)**
$NbSe_2$	686	1017	301	0.579	202	3.00
$Co_3O_4/CoSe_2$-$NbSe_2$	432	964	454	0.320	91	4.2
COS/PTO-$NbSe_2$	359	769	294	0.370	81	15.6
Co/Co_3O_4-$NbSe_2$	323	707	120	0.540	52	21.2

Pt/C	97	256	77	0.846	n/a	n/a

To evaluate the HER kinetics, EIS measurements were performed at an applied potential of 1.4 V. Fig. 10a shows the Nyquist plots fitting the equivalence circuit shown in Fig. 10c. The smaller the R_{ct} value, the better the charge transfer kinetics of the electrocatalyst [44]. The R_{ct} trend was as follows: Co/Co_3O_4-$NbSe_2$ < COS/PTO-$NbSe_2$ < $Co_3O_4/CoSe_2$-$NbSe_2$ < $NbSe_2$. Fig. 10b shows the linear relationship between the current density and potential scan rate, where the slope is electrochemical double-layer capacitance (C_{dl}). Indeed, the trend of C_{dl} is the reverse of R_{ct}, indicated in Table 2. Fig. S4 of the CVs of all the electrocatalysts in this study at different scan rates (10, 15, 20, 25, 30, 40 mV/s). The CVs show the expected rectangular feature of an electrical double-layer capacitor. In addition, the electrochemically active surface area (ECSA) of the electrocatalysts in this study was also calculated by dividing the C_{dl} value of the electrocatalyst by the specific capacitance (Cs) from the literature and summarised in Table S1. (a Cs value of 40 $\mu F/cm^2$ was used in the calculations) [60]. Co/Co_3O_4-$NbSe_2$ electrocatalyst has the highest ECSA value of 104 cm^2, and $NbSe_2$ with the lowest value of 14.7 cm^2. Stability studies were performed on the Co/Co_3O_4-$NbSe_2$ electrocatalyst, which was the best-performing electrocatalyst, by conducting the chronoamperometry studies. Fig. 10a showed the chronoamperometry profile when a potential of 500 mV was applied, and the current density drastically increased. After ~ 30 min, the current density gradually increased for a further ~ 1.5 h. Therefore, Co/Co_3O_4-$NbSe_2$ electrocatalyst continues to generate more current the longer it is used.

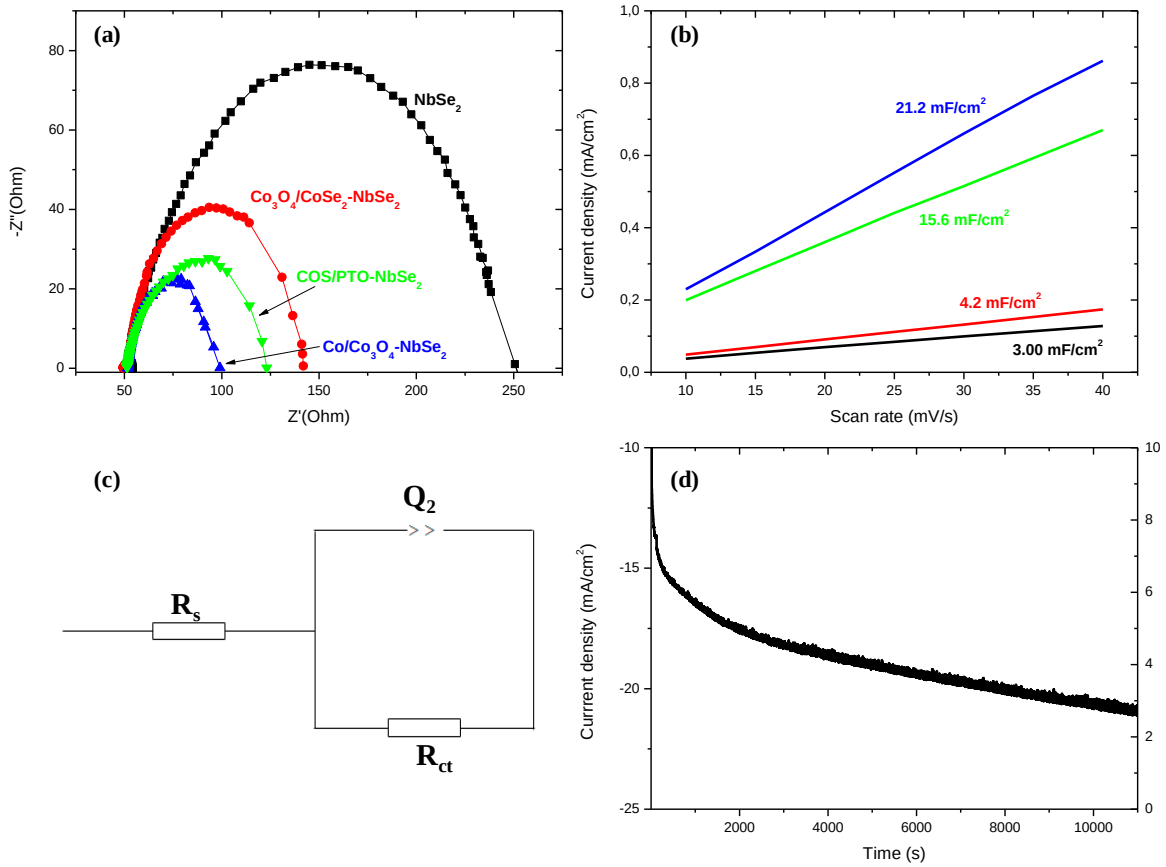

Fig. 10 (a) Nyquist plots, and (b) exchange current density (j_0) of $NbSe_2$ compared to the resultant nanomaterials after the decoration of $NbSe_2$, (c) equivalence circuit fitted to the Nyquist plots nanomaterials synthesised, and (d) Chronoamperometry for Co/Co_3O_4-$NbSe_2$ nanomaterial at 500 mV vs RHE applied potential and 11 000 s time scale.

Decoration of $NbSe_2$ with Co and a mixture of Pt and Co metals nanomaterials resulted in a significant enhancement in the electrocatalytic activity of $NbSe_2$ toward hydrogen production. The Co-decorated $NbSe_2$ ex-situ sample was the best-performing electrocatalyst compared to the in-situ sample and the 10% wt. Pt / 10% wt. Co sample. The ex-situ sample contained metallic nanoparticles; therefore, according to the volcano plot, it is expected to have superior HER activity. COS/PTO-$NbSe_2$ resulted in an electrocatalytic activity somewhere between Co/Co_3O_4-$NbSe_2$ and $Co_3O_4/CoSe_2$-$NbSe_2$ because only 10 % wt Pt was used. The results were consistent with the volcano plot with the following trend: Co/Co_3O_4-$NbSe_2$ < COS/PTO-$NbSe_2$ < $Co_3O_4/CoSe_2$-$NbSe_2$ < $NbSe_2$. More specifically, the ex-situ sample had superior activity compared to the in-situ samples. Tahira *et al.* formed a Co_3O_4-CuO nanocomposite where Cu was incorporated into Co_3O_4 nanowires [48]. They reported that Cu activated Co_3O_4 to form a

highly efficient electrocatalyst toward HER [48]. Kong *et al.* also reported that $CoSe_2$ showed one of the best HER performances compared to the first-row transition-metal chalcogenides due to the partially filled e_g band within $CoSe_2$ [61]. As such, forming heterostructures with $NbSe_2$ and Co, Co_3O_4, $CoSe_2$, or Pt oxides has enhanced the HER activity.

4.5. Conclusion

This study indicates that incorporating Co- and Pt-based materials into $NbSe_2$ nanoflowers have resulted in highly efficient electrocatalysts toward HER. This is due to the synergistic effects which result in highly active electrocatalysts. According to the results obtained, Co/Co_3O_4-$NbSe_2$ (ex-situ) had the lowest overpotential at a current density of 10 mA/cm^2, Tafel slope, exchange current density, and R_{ct}, as well as the highest C_{dl} and ECSA. We observed that the metallic Co nanoparticles contributed best to the enhancement of $NbSe_2$ as the Co/Co_3O_4-$NbSe_2$ electrocatalyst was the only catalyst with zero-valent Co, as confirmed by the XPS results. Therefore, the heterostructures of $NbSe_2$ nanoflowers worked.

4.6. References

[1] H. Zhong, C. A. Campos-Roldán, Y. Zhao, S. Zhang, Y. Feng, N. Alonso-Vante, *Catalysts*, 2018, 8, 559.

[2] S. Park, Y. Y. Shao, J. Liu, Y. Wang, *Energy Environ. Sci.*, 2012, 5, 9331–9344.

[3] L. Carrette, K.A. Friedrich, U. Stimming, Fuel Cells, 2001, 1, 5–39.

[4] Y. Jiao, Y. Zheng, M. Jaroniec, S.Z. Qiao, *Chem. Soc. Rev.*, 2015, 44, 2060-2086.

[5] N.T. Suen, S.F. Hung, Q. Quan, N. Zhang, Y.J. Xu, H.M. Chen, *Chem. Soc. Rev.*, 2017, 46, 337-365.

[6] X. Ge, A. Sumboja, D. Wuu, T. An, B. Li, F.W.T. Goh, T.S.A. Hor, Y. Zong, Z. Liu, *ACS Catal.*, 2015, 5, 4643-4667.

[7] L.M. Dai, Y.H. Xue, L. T. Qu, H. J. Choi, J. B. Baek, Chem. Rev. 2015, 115, 4823–4892.

[8] Q. Liu, J. T. Jin, J.Y. Zhang, *ACS Appl. Mater. Interfaces*, 2013, 5, 5002–5008.

[9] M. Gong, Y. G. Li, Wang, H. L., Y. Y.Liang, J. Z. Wu, J. G. Zhou, J. Wang, T. Regier, F. Wei, H.J. Dai, *J. Am. Chem. Soc.*, 2013, 135, 8452–8455.

[10] A. Q. Zhao, J. Masa, W. Xia, A. Maljusch, M. G. Willinger, G. Calavel, K. P. Xie, R. Schlogl, W. Schuhmann, M. Muhlert, *J. Am. Chem. Soc.*, 2014, 136, 7551–7554.

[11] R. F. Xie, G. L. Fan, Q. Ma, L. Yang, F. Li, *J. Mater. Chem. A*, 2014, 2, 7880–7889.

[12] A. Sumboja, T. An, H. Y. Goh, M. Lubke, D. P. Howard, Y. Xu, A. D. Handoko, Y. Zong, Z. Liu, *ACS Appl. Mater. Interfaces*, 2018, 10, 15673–15680.

[13] S. S. Pramana, A. Cavallaro, C. Li, A. D. Handoko, K. W. Chan, R. J. Walker, A. Regoutz, J. S. Herrin, B. S. Yeo, D. J. Payne, *et al.*, *J. Mater. Chem. A*, 2018, 6, 5335–5345.

[14] M. Lübke, A. Sumboja, L. McCafferty, C. F. Armer, A. D., Handoko, Y. H. Du, K. McColl, F. Cora, D. Brett, Z. L. Liu, *et al.*, *ChemistrySelect*, 2018, 3, 2613–2622.

[15] G. Jia, Y. Hu, Q. Qian, Y. Yao, S. Zhang, Z. Li, Z. Zou, *ACS Appl. Mater. Interfaces*, 2016, 8, 14527–14534.

[16] Z. Yang, Z. Yao, G. Li, G. Y. Fang, H. G. Nie, Z. Liu, X. M. Zhou, X. A. Chen, S. M. Huang, *ACS Nano*, 2012, 6, 205–211.

[17] Q. Zhu, Y. Qu, D. Liu, K. W. Ng, H. Pan, *ACS Appl. Nano Mater.*, 2020, 3, 6270-6296.

[18] H. Li, Y. Shi, M. H. Chiu, L. J. Li, *Nano Energy*, 2015, 18, 293-305.

[19] F. Wang, Z. Wang, Q. Wang, F. Wang, L. Yin, K. Xu, Y. Huang, J. J. N. He, *Nanotechnology*, 2015, 26, 292001.

[20] B. Peng, P. K. Ang, K. P. Loh, *Nano Today*, 2015,10, 128-137.

[21] C. Tan, H. Zhang, *Chem. Soc. Rev.*, 2015, 44, 2713-2731.

[22] R. Lv, H. Terrones, A. L. Elías, N. Perea-López, H. R. Gutiérrez, E. Cruz-Silva, L. P. Rajukumar, M. S. Dresselhaus, M. Terrones, *Nano Today*, 2015, 10, 559-592.

[23] P. Prabhu, V. Jose, J. M. Lee, *Matter*, 2020, 2, 526-553.

[24] D. Voiry, J. Yang, M. Chhowalla, Adv. Mater., 2016, 28, 6197-6206.

[25] Z. Guan, C. S. Lian, S. Hu, S. Ni, J. Li, W. Duan, *J. Phys. Chem. C*, 2017, 121, 3654-3660.

[26] Z. Guan, S. Ni, S. Hu, *J. Phys. Chem. C*, 2018, 122, 6209-6216.

[27] K. S. Novoselov, A. Mishchenko, A. Carvalho, A. H. Castro Neto, *Science*, 2016, 353, aac9439.

[28] Y. Chen, G. Zhao, W. Sun, *Materials for Renewable and Sustainable Energy*, 2020, 9, 2-11.

[29] G. Chen, C. Xu, X. Huang, J. Ye, L. Gu, G. Li, Z. Tang, B. Wu,
H. Yang, Z. Zhao, Z. Zhou, G. Fu, N. Zheng, *Nat. Mater.*, 2016, 15, 564.

[30] C. H. Choi, M. Kim, H. C. Kwon, S. J. Cho, S. Yun, H. T. Kim, K. J. J. Mayrhofer, H. Kim, M. Choi, *Nat. Commun.*, 2016, 7, 10922.

[31] L. Han, S. Dong, E. Wang, *Adv. Mater.*, 2016, 28, 9266–9291.

[32] C. Tang, H. F. Wang, X. Chen, B. Q. Li, T. Z. Hou, B. Zhang, Q. Zhang, M. M. Titirici, F. Wei, *Adv. Mater.*, 2016, 28, 6845–6851.

[33] D. Strmcnik, P. P. Lopes, B. Genorio, V. R. Stamenkovic, N. M. Markovic, *Nano Energy*, 2016, 29, 29–36.

[34] Z. W. Seh, J. Kibsgaard, C. F. Dickens, I. Chorkendorff, J. K. Nørskov, T. F. Jaramillo, Science., 2017, 355, eaad4998.
[35] K. S. Novoselov, A. Mishchenko, A. Carvalho, A. H. Castro Neto, A.H., 2016, 353, aac943.
[36] X. F. Dai, J. L. Qiao, X. J. Zhou, J. J. Shi, P. Xu, L. Zhang, J. J. Zhang, *Int. J. Electrochem. Sci.*, 2013, 8, 3160-3175.
[37] S. Zhao, B. Rasimick, W. Mustain, H. Xu, *Appl. Catal. B*, 2017, 203, 138-145.
[38] S. Y. Liu, L. J. Li, H. S. Ahnb, A. Manthiram, *J. Mater. Chem. A*, 2015, 3, 11615-11623.
[39] Z. S. Wu, W. C. Ren, L. Wen, L. B. Gao, J. P. Zhao, Z. P. Chen, G. M. Zhou, F. Li, H. M. Cheng, *ACS Nano*, 2010, 4, 3187-3194.
[40] N. P. Subramanian, S. P. Kumaraguru, H. Colon-Mercado, H. Kim, B. N. Popov, T. Black, *D.A. Chen, J. Power Sources*, 2006, 157, 56-63.
[41] M. Khan, M.N. Tahir, S. F. Adil, H. U. Khan, M. R. H. Siddiqui, A.A. Al-Warthan, W. Tremel, *J. Mater. Chem. A*, 2015, 3, 18753-18808.
[42] D. Zhu, J. Liu, Y. Zhao, Y. Zheng, S. Z. Qiao, *Small*, 2019, 15, 1805511.
[43] T. Kolokoto, V. Mashindi, R. Kadzutu-Sithole, Lerato F. E. Machogo-Phao, Z. B. Ndala, N. P. Shumbula, S. S. Nkabinde, G. N. Ngubeni, S. S. Gqoba, K. P. Mubiayi, N. Moloto, *RSC Adv.*, 2021, 11, 31159-31173.
[44] J. Zhang, Y. Wang, C. Zhang, H. Gao, L. Lv, L. Han, Z. Zhang, *ACS Sustainable Chem. Eng*. 2018, 6, 2231-2239.
[45] M. Smyrnioti, T. Loannides, *Intech Open Science*, Chapter 3, 50-66.
[46] C. Wang, C. Zhang, W. Hua, Y. Guo, G. Lu, S. Gil, A. Giroir-Fendler, *Chemical Engineering Journal.*, 2017, 315, 392-402.
[47] Q. Huang, J. Zhang, Z. He, P. Shi, X. Qin, W. Yao, *Chemical Engineering Journal*, 2017, 313, 1088-1098.
[48] D. Kong, H. Wang, Z. Lu, Y. Cui, *J. Am. Chem. Soc.*, 2014, 136, 4897-4900.
[49] J. Yang, G. H. Cheng, J. H. Zeng, S. H. Yu, X. M. Liu, Y. T. Qian, *Chem. Mater.*, 2001, 13, 848-853.
[50] H.v an der Heide, R. Hemmel, C. F. van Bruggen, C. J. Haas, *Solid State Chem.*, 1980, 33, 17-25.
[51] N. K. M. Safeer, C. Alex, R. Jana, A. Datta, N. S. John, *J. Mater. Chem. A*, 2022.
[52] A. F. Carley, S. Rassias, *Surf. Sci.*, 1983, 135, 35–51.
[53] H. A. E. Hagelin-Weaver, J. F. Weaver, G. B. Hoflund, G. N. Salaita, *J. Electron Spectrosc. Relat. Phenom.*, 2004, 134, 139–171.

[54] D. Boscher, C. J. Carmalt, I. P. Parkin, Eur. *J. Inorg. Chem.*, 2006, 1255–1259.

[55] E.P. Mukhokosi, S.B. Krupanidhi, K.K. Nanda, *Sci. Rep.*,2017, 1, 1–10.

[56] Z. B. Ndala, N. P. Shumbula, S. Nkabinde, T. Kolokoto, S. Gqoba, C. Linganiso, N. Moloto, *Journal of Electroanalytical Chemistry*, 2022, 918, 116464.

[57] J. D. Cooper, V. P. Vitullo, D. L. Whalen, *J. Am. Chem. Soc.*, 1971, 93, 6296.

[58] M. Gao, Z. Lin, J. Jiang, C. Cui, Y. Zheng, S. Yu, Chem. Eur. J. 2012, 18, 8423 – 8429.

[59] J. Zhang, Y. Wang, C. Zhang, H. Gao, L. Lv, L. Han, Z. Zhang, *ACS Sustainable Chem. Eng*. 2018, 6, 2231−2239.

[60] P. Connor, J. Schuch, B. Kaiser, W. Jaegermann, *Z. Phys. Chem.*, 2020, 234, 979–994.

[61] D. S. Kong, J. J. Cha, H. T. Wang, H. R. Lee, Y. *Cui, Energy Environ. Sci.*, 2013, 6, 3553-3558.

Chapter 4

Supplementary information

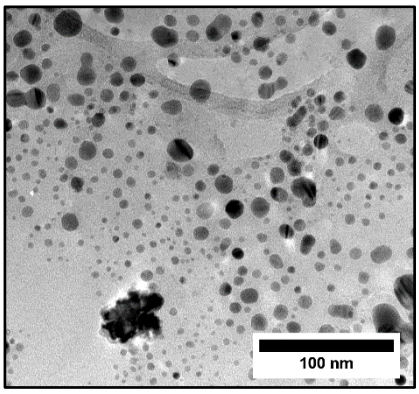

Fig. S1: TEM images of Co nanoparticles used in the ex-situ method to produce Co/Co_3O_4-$NbSe_2$.

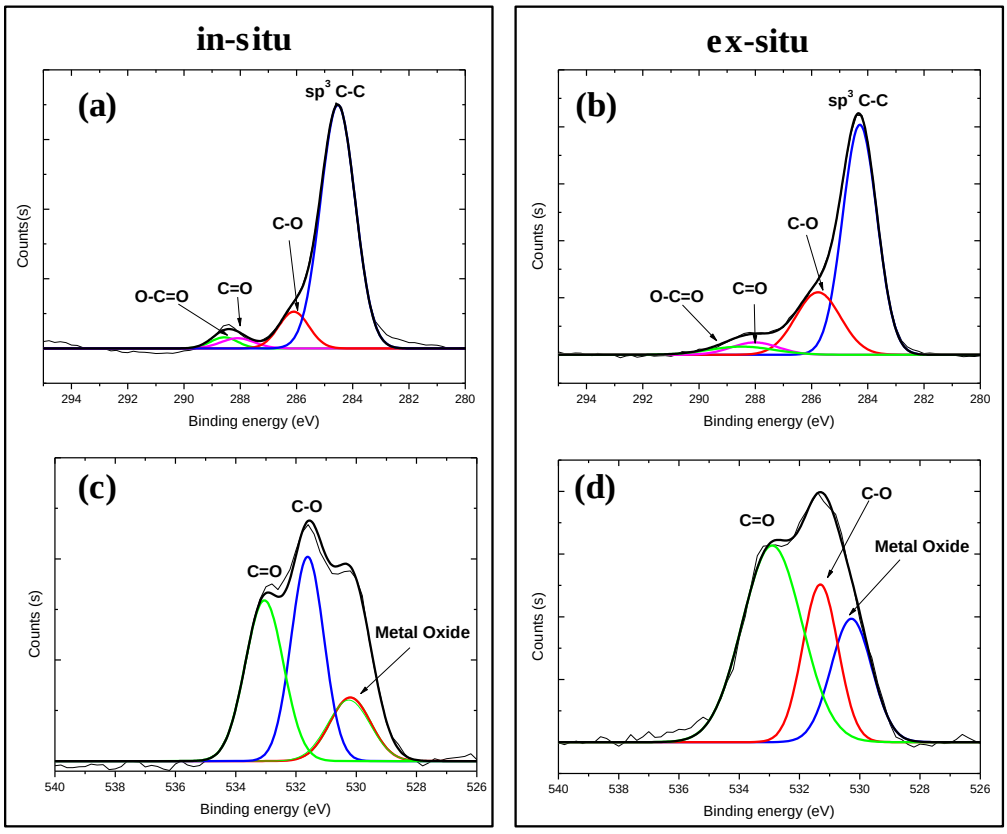

Fig. S2: (a) and (b) C1s, (c) and (d) O1s XPS core-level spectra of Co-decorated $NbSe_2$ in-situ and ex-situ nanomaterials.

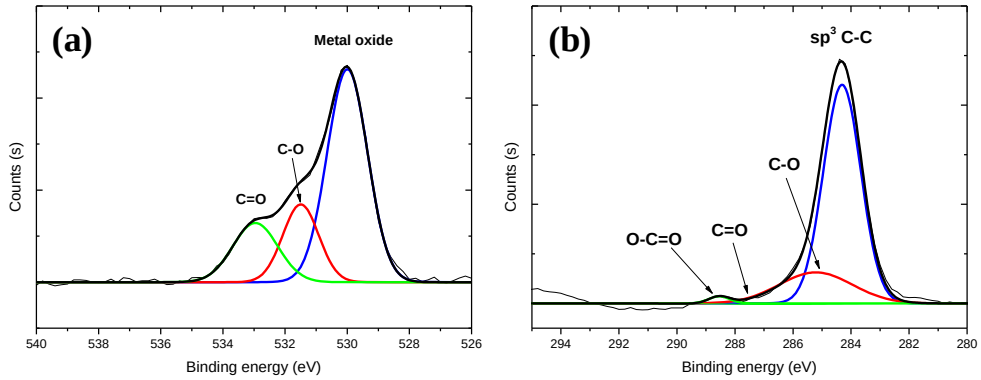

Fig. S3: (a) C1s and (b) O1s XPS core-level spectra of Co-decorated $NbSe_2$ in-situ and ex-situ nanomaterials.

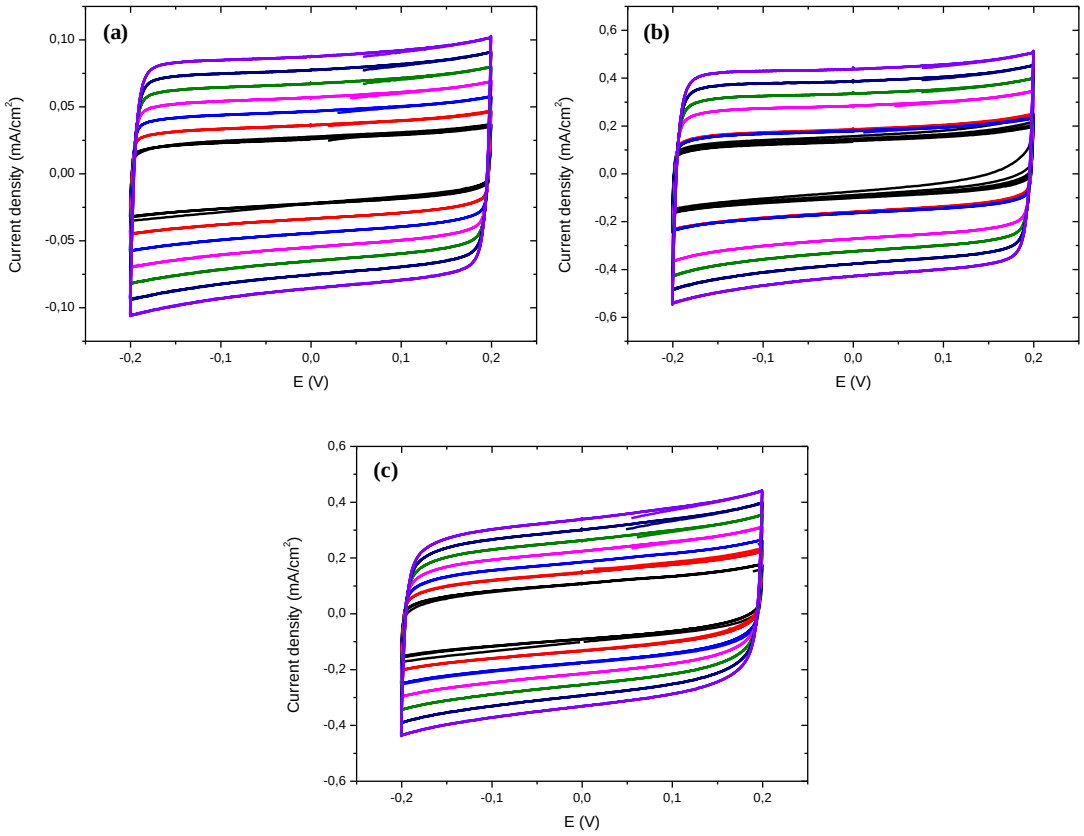

Fig. S4: (a) $Co_3O_4/CoSe_2$-$NbSe_2$, (b) Co/Co_3O_4-$NbSe_2$, (c) COS/PTO-$NbSe_2$.

Table S1: ECSA of the decorated $NbSe_2$ in comparison to bare $NbSe_2$ calculated using electrochemical double-layer capacitance (C_{dl}) and specific capacitance (Cs) of 40 μF/cm^2

Sample	**ECSA (cm^2)**
$NbSe_2$	14.7
Co_3O_4/$CoSe_2$-$NbSe_2$	20.6
COS/PTO-$NbSe_2$	76.4
Co/Co_3O_4-$NbSe_2$	104

Chapter 5

Electrochemical enhancement towards HER of 2D-$TaSe_2$ through decoration with Co, Ni and Pt-based nanocrystals

5.1. Introduction

There has been a tremendous drive to find energy sources that are alternatives to fossil fuels and that will have minimum impact on the environment. Hydrogen as an energy carrier has received much attention from researchers as a suitable alternative owing to its zero emission of greenhouse gases and high energy density [1-2]. The most popular way of producing hydrogen currently is the steam reforming process that converts natural gas (methane) into hydrogen at high-temperature conditions (450 -1000 °C). The drawback with steam reforming is its contribution to global greenhouse gas emissions through the generation of carbon monoxide and carbon dioxide, as well as the high temperature and pressure required for operation. To circumvent greenhouse gas emissions, carbon capture and storage are sometimes used [3-6]. However, an alternative to steam reforming, electrocatalytic hydrogen evolution reaction (HER) is amongst the promising processes that have the potential to produce hydrogen without polluting the environment [7]. However, the HER requires high overpotentials for the cathodic reaction. To lower the overpotential, an electrocatalyst is needed. While Pt is the most efficient electrocatalyst, alternatives are needed that are less expensive and that can ease or reduce the complete reliance on platinum as a catalyst [8]. Transition metal dichalcogenides (TMDCs) have attracted interest for hydrogen (HER) [9-11]. TMDCs are typically categorised into semiconducting and metallic materials from different compositions and crystal structures [12]. Semiconductors such as MoS_2 and $MoSe_2$ have been widely studied. Recently, metallic 2H-TMDCs from group 5 (e.g. Ta, Nb, V) are of interest for the HER study due to their intrinsic basal plane activity beyond that of metal or chalcogen edges [13-15]. Group 5 TMDCs' electrocatalytic activity originates from their unsaturated chalcogen edges and highly active surface basal planes, whereas group 6 TMDCs' activity originates from chalcogen- or metal-unsaturated edges only [16]. This has been confirmed by density functional theory calculations. The catalytic properties of their basal planes could make these materials suitable for scalability.

To date, 2H-TaS_2 nanoplatelets synthesized by chemical vapour deposition have displayed record-high surface HER activity (e.g., $\eta_{10} < 60$ mV with a loading of the catalyst <60 μg cm^{-2}) among all of the reported TMDCs [17]. In this work, the electrochemical performance of $TaSe_2$ was evaluated. In order to improve the performance, $TaSe_2$ was decorated with small amounts of Co, Ni and Pt (20% wt) for hybrid formation.

5.2. Methodology

5.2.1 Chemicals

Tantalum(V) chloride ($TaCl_5$, 99%), selenium powder (Se) (99.9%), octadecene (ODE) (70%), hexane (95%), ethanol (96%), sodium borohydride ($NaBH_4$, ≥ 98%), potassium hydroxide (KOH, 90%), isopropanol (≥ 99.5%), Nafion (5 wt%), nickel(II) bis(acetylacetonate) ($Ni(acac)_2$, 95%), cobalt(II) bis(acetylacetonate) ($Co(acac)_2$, 95%), and platinum(II) bis(acetylacetonate) ($Pt(acac)_2$, 97%) were all purchased from Sigma-Aldrich.

5.2.2 Synthesis of $TaSe_2$

Octadecene was added to a three-neck round-bottomed flask and degassed for 15 min. This was followed by a stoichiometric 1:3 addition of $TaCl_5$ and Se. The mixture was heated up to 310 ℃ for 2 h under N_2 flow. The reaction was cooled to room temperature, and the black precipitate was washed with large amounts of hexane, allowed to dry, and ready for characterisation.

5.2.3 Decoration of $TaSe_2$ using the ex-situ method

In the ex-situ synthetic method, a 1:1 ratio of the reducing agent $NaBH_4$ and metal precursors ($Ni(acac)_2$ for the Ni source, $Co(acac)_2$ for the Co source, and $Pt(acac)_2$ for the Pt source) was added to a degassed OLA in a three-necked round bottom flask. The readily synthesised nanoparticles were washed with hexane, followed by distilled water to remove excess/unreacted $NaBH_4$, and then dried and ready for characterisation. Once dried, the transition metal-based nanoparticles (20% wt), Ni, Co, Pt, were mixed with the $TaSe_2$ and added into 1 mL of ethanol. The mixture was sonicated for 60 min then placed onto a shaker at 180 rpm for 24 h. The mixture was then washed with hexane, dried, and ready for characterisation. Table 1 contains the reaction conditions used for each sample.

Table 1: Summary of the reaction conditions for the synthesis of Ni, Co, and Pt nanoparticles

Sample	Metal precursor	Capping agent	Concentration (M)	Temperature (℃)	Time (min)
1	$Ni(acac)_2$	OLA	0.0500	280	120
2	$Co(acac)_2$	OLA	0.0251	280	120
3	$Pt(acac)_2$	OLA	0.0234	300	120

5.2.4 Characterisation of the pristine $TaSe_2$ and the hybrid nanomaterials

The structure and phase of the powdered materials were determined using the Bruker MeasSrv (D2-205530)/D2-205530 diffractometer using secondary graphite monochromated CuKα radiation (λ = l 1.54184 Å) at 30 kV/30 mA. Measurements were taken using a glancing angle of incidence detector at an angle of 2°, for 2θ values over 10 – 90° in steps of 0.026° with a step time of 37 s, and at room temperature. X-ray photoelectron spectroscopy (XPS) measurements were performed with a Thermo ESCAlab 250Xi using monochromatic Al Kα (1486.7 eV) X-rays at a power of 300 W with a spot size of 900 mm. An FEI Spirit 120 kV transmission electron microscope (TEM) was operated at an accelerated voltage of 200 kV with a beam spot size of 20–100 nm in TEM mode and was also used to study the morphology of the samples. The samples were dispersed in hexane and drop-casted onto a lacey carbon copper grid. The solvent was then evaporated at room temperature.

5.2.5 Electrochemical characterisation

The Biologic SP 300 was used to investigate the electrochemical performance of HER in a three-electrode system. The measurements were performed in an alkaline solution of 0.1 M of KOH. The Ag/AgCl electrode was used as a reference electrode, the Pt wire as a counter electrode, and the working electrode made up of the hybrid nanomaterials' thin film on a glassy carbon electrode with a surface area of 0.07065 cm^2. The electrochemical performance of pristine $TaSe_2$ and Pt/C loaded onto the glassy carbon electrode was also measured for comparison. The thin films were formed by drop-casting about 10 uL of ink onto the glassy carbon electrode and left to dry at room temperature. The inks were formed by dissolving 2.2 mg of the sample and 1.6 mg of Vulcan in a mixture of 20 μL Nafion (5 wt%) and 400 μL isopropanol and then sonicated for 1 h. The electrolyte was purged with argon for 30 min. This was followed by cyclic voltammetry (CV) measurements where the working electrode's potential was swept between -0.2 – 0.5 V vs RHE for 20 cycles at 100 mV/s. This process

activates the surface of the electrocatalyst. The double layer was measured within the potential window of -0.2 – 0.4 V at various scan rates: 10, 15, 20, 25, 30, and 40 mV/s. The linear sweep voltammetry (LSV) was conducted at a scan rate of 2 mV/s. The electrochemical impedance spectroscopy measurements were recorded at a potential of -0.836 V vs RHE and a frequency range between 0.2 Hz and 100 kHz. The working electrode potentials vs Ag/AgCl were converted to the RHE scale using the equation below:

$$E_{RHE} = E_{Ag/AgCl} + 0.059pH + 0.0197$$

where E_{RHE} is the measured potential and pH = 13.

5.3. Results and discussion

5.3.1 Synthesis and characterisation of $TaSe_2$

XRD and TEM analysis was performed to investigate the structure and morphology of the readily synthesised 2H-$TaSe_2$ nanomaterial. Fig. 1a shows the XRD pattern of $TaSe_2$ resulted in the formation of 2H-$TaSe_2$ (PDF 01-073-1798) hexagonal phase with some impurities denoted by '*' and '&' due to excess Se and surface oxidation (Ta_2O_5), respectively. Fig. 1b shows a TEM image of 2H-$TaSe_2$ containing a mixture of rodlike and irregularly shaped wrinkled structures. At higher magnification, the rodlike structures are made up of sheets with an interlayer spacing of 0.63 nm (shown in Fig. 1b), suggesting multi-layer sheet formation.

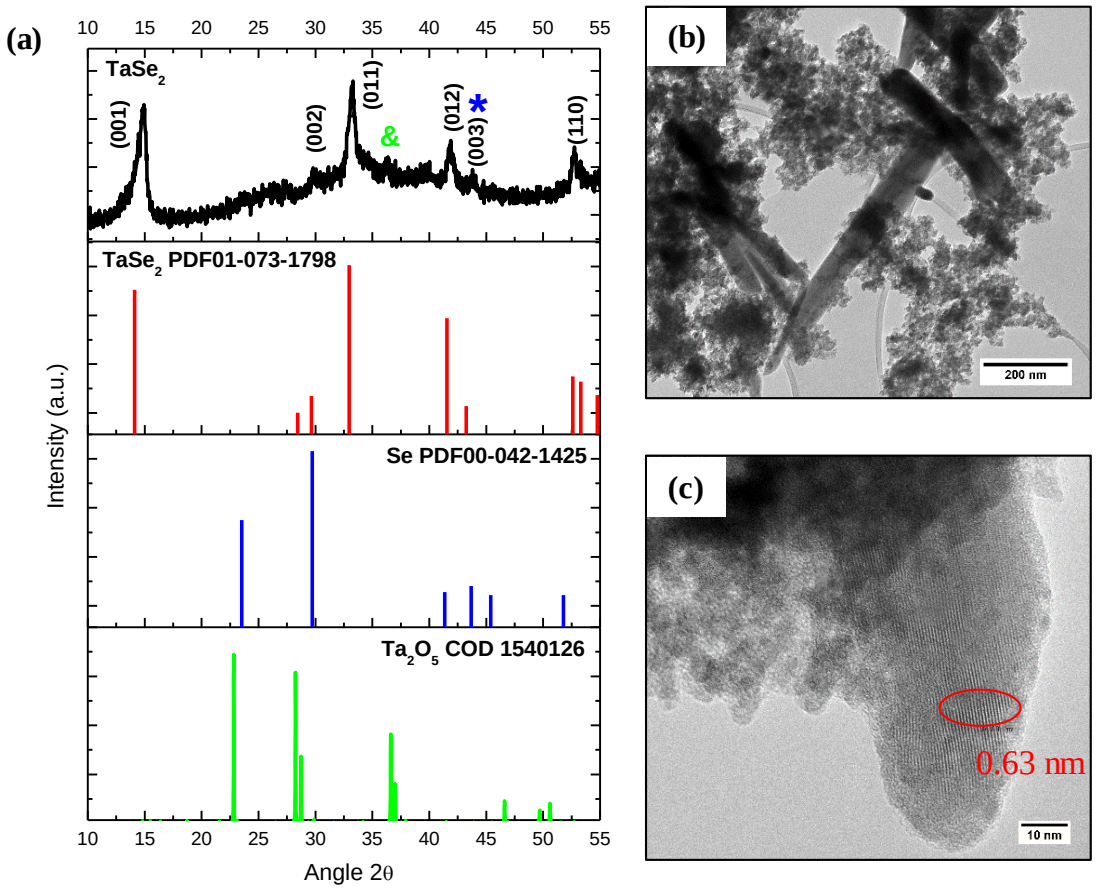

Fig. 1: (a) XRD pattern, (b) and (c) TEM images of $TaSe_2$ nanomaterial; '*' and '&' represent Se and Ta_2O_5, respectively.

X-ray photoelectron spectroscopy (XPS) analysis was performed to investigate further the surface compositions and valency of the as-prepared $TaSe_2$ nanomaterials. Fig. 2a shows that the XPS survey spectra contained the following species Ta, Se, C, and O, where O was due to the oxidation of the samples and C due to the capping agent used in the synthesis [31]. Fig. 2b shows the Ta 4f XPS spectrum of the $TaSe_2$ sample and reveals four prominent peaks attributed to Ta-Se and Ta-O bonding [12, 18]. The weaker Ta-O peaks of Ta $4f_{5/2}$ at 29 eV and Ta $4f_{7/2}$ at 27 eV are caused by oxidation on the surface. The Ta-Se peaks of Ta $4f_{5/2}$ 24 eV and Ta $4f_{7/2}$ 22 eV imply that $TaSe_2$ was synthesised [12, 19, 20]. Tsai *et al.* synthesised $TaSe_2$ on a Si/SiO_2 supported and also obtained four prominent peaks (Ta 4f XPS spectrum) attributed to Ta-Se and Ta-O [12]. Fig. 2c shows the Se 3d XPS spectrum deconvoluted two peaks, $3d_{3/2}$ at 54.2 eV and $3d_{5/2}$ (53.0 eV); these peaks agree with the $TaSe_2$ spectra [19, 18]. Fig. S1a show the O1s spectra deconvoluted to three peaks: metal oxide at 530 eV, C-O at 532 eV, and C=O at

33 eV. In this case, the C-O peak is attributed to O^{2-} from the Ta-O lattice. The C=O peak indicates surface-adsorbed oxygen (O_2) through the capping agent synthesising $TaSe_2$ [12]. Fig. S1b shows the C 1s XPS spectra consisting of C-C (sp^2 and sp^3), C-O, O-C=O, and C=O.

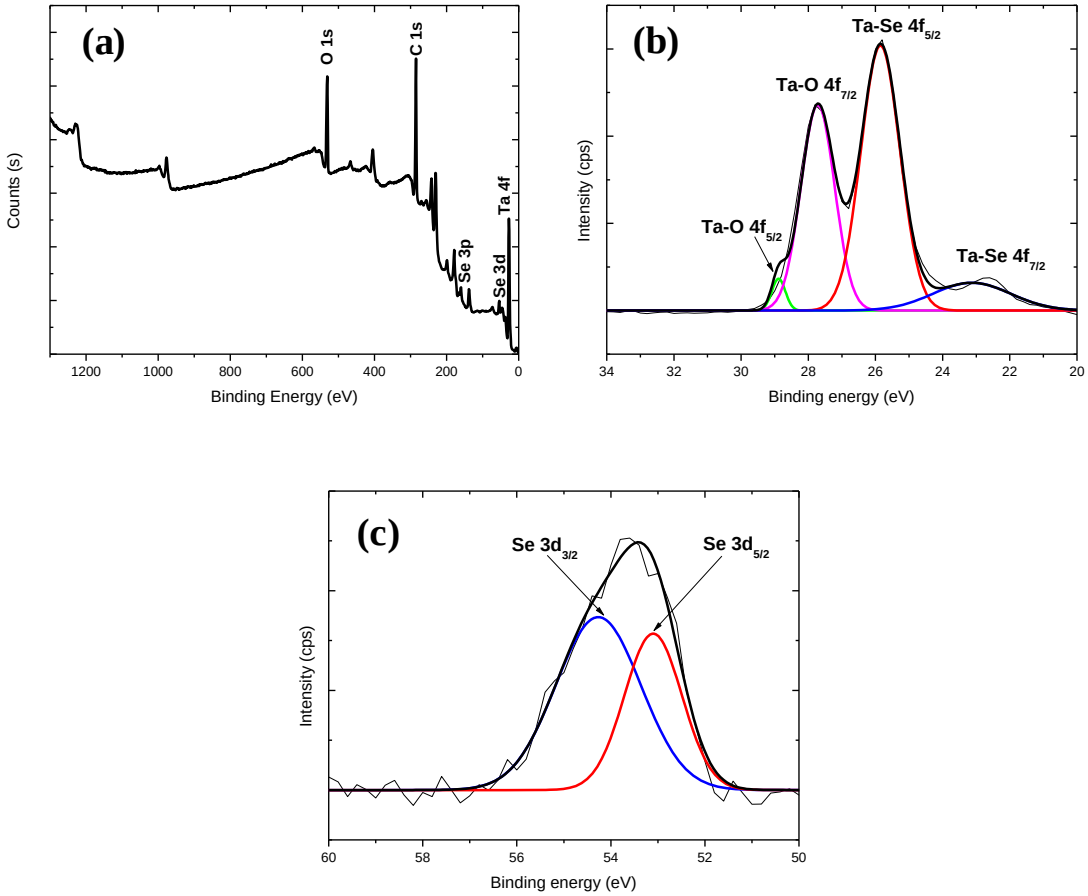

Fig. 2: (a) XPS survey spectra, (b) Ta 4f, and (c) Se 3d XPS core-level spectra of $TaSe_2$.

5.3.2 Decoration of $TaSe_2$ using Co nanoparticles

The phase, composition, and crystallinity of the ex-situ Co-decorated $TaSe_2$ sample were confirmed using XRD (shown in Fig. 3). The sample was compared to the pristine 2D $TaSe_2$. The sample is a mixture of structures obtained in the pristine $TaSe_2$ with additional Co nanoplates. Fig. 3a shows that the sample comprises 2H-$TaSe_2$ (PDF 01-073-1798) hexagonal phase and Co cubic phase (PDF 00-001-1259) denoted by '♦'. Fig. 3b shows the TEM image of the Co-decorated $TaSe_2$ sample. In addition, Ta_2O_5 (CDO #1540126) peak was observed at 36.4 ° 2θ denoted by '&', Se (PDF 00-042-1425) peak at 43.6 ° 2θ denoted by '*', and Co_3O_4 (COD #1526734) peak overlapping the Se peak at 43.6 ° 2θ denoted by '∀'. The overlapping of Co and Co_3O_4 peaks with the $TaSe_2$ peaks were observed due to a mixture of the materials.

.

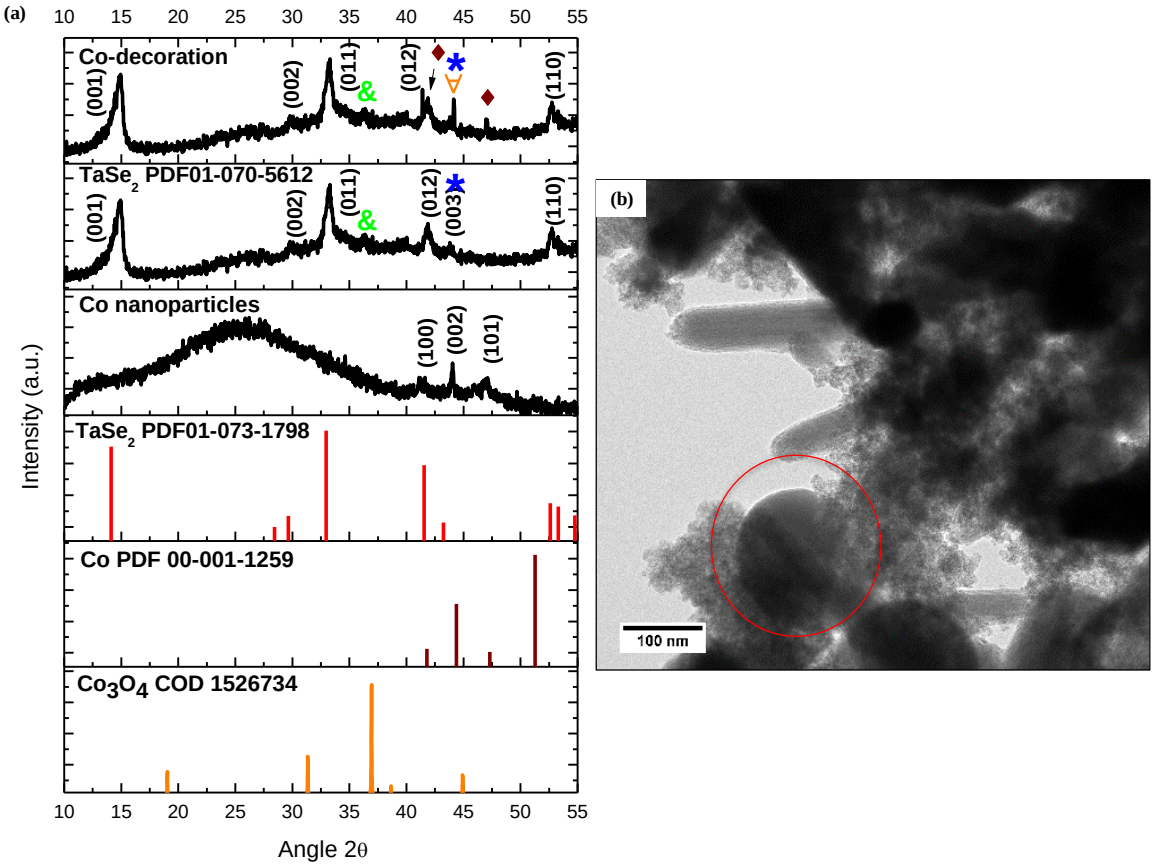

Fig. 3: (a) XRD pattern and (b) TEM images of Co-decorated $TaSe_2$ nanomaterial; '*', '&', '♦', and '∀' represent Se, Ta_2O_5, Co, and Co_3O_4, respectively.

Fig. 4a shows the XPS survey spectra of the Co-decorated $TaSe_2$ nanomaterial. The nanomaterial contained expected species such as Co, Ta, Se, C, and O, where O was due to the oxidation of the samples and C was due to the capping agent used in the synthesis [21]. Fig 4b shows that the Co-decorated $TaSe_2$ nanomaterial Ta 4f XPS spectra have two Ta-Se peaks ($4f_{5/2}$ at 24.9 eV and $4f_{7/2}$ at 23.1 eV) attributed to $TaSe_2$ and a Ta-O peak ($4f_{7/2}$ at 27.7 eV) due to oxidation at the surface of the nanomaterial [12, 18, 20]. Similarly, the Se 3d XPS spectra also comprised two peaks at 55.0 eV ($3d_{3/2}$) and 53.2 eV ($3d_{5/2}$) (shown in Fig. 3c) [17, 18]. This confirms the presence of $TaSe_2$ nanomaterial within the sample. Fig. 4a shows the Co 2p XPS spectrum of the Co-decorated $TaSe_2$ nanomaterial, which decomposed into two distinct peaks and two weak satellites. The spin-orbit was assigned to Co oxides corresponding to Co $2p_{1/2}$ and Co $2p_{3/2}$ located at 795.9 and 780.8 eV, respectively. The Co $2p_{1/2}$ was deconvoluted into peaks contributed by Co^{2+} at 798.6 eV, Co^{3+} at 796.4 eV, and satellite peak denoted as 'sat.' at 803.5 eV [22]. Similarly, the Co^{2+}, Co^{3+}, and satellite peaks can also be seen from Co $2p_{3/2}$ at

782.6, 780.7, and 788.0 eV, respectively. The satellite peaks near two spin doublet peaks further provide evidence of cobalt oxides such as Co_3O_4 [34-36]. Smyrnioti *et al.* synthesised Co_3O_4 nanoparticles with similar XPS results [22-24]. This agrees with the XRD results; however, no Co^0 peak was observed in Co 2p XPS spectra for metallic Co observed in the XRD pattern. Fig. S2a show the O1s spectra deconvoluted to three peaks: metal oxide at 530.2 eV, C-O at 531.5 eV, and C=O at 532.8 eV. The C-O peak is attributed to O^{2-} from the Ta-O and Co-O lattice [24]. Similarly, Fig. S1b shows the C 1s XPS spectra consisting of C-C (sp^3), C-O, O-C=O, and C=O.

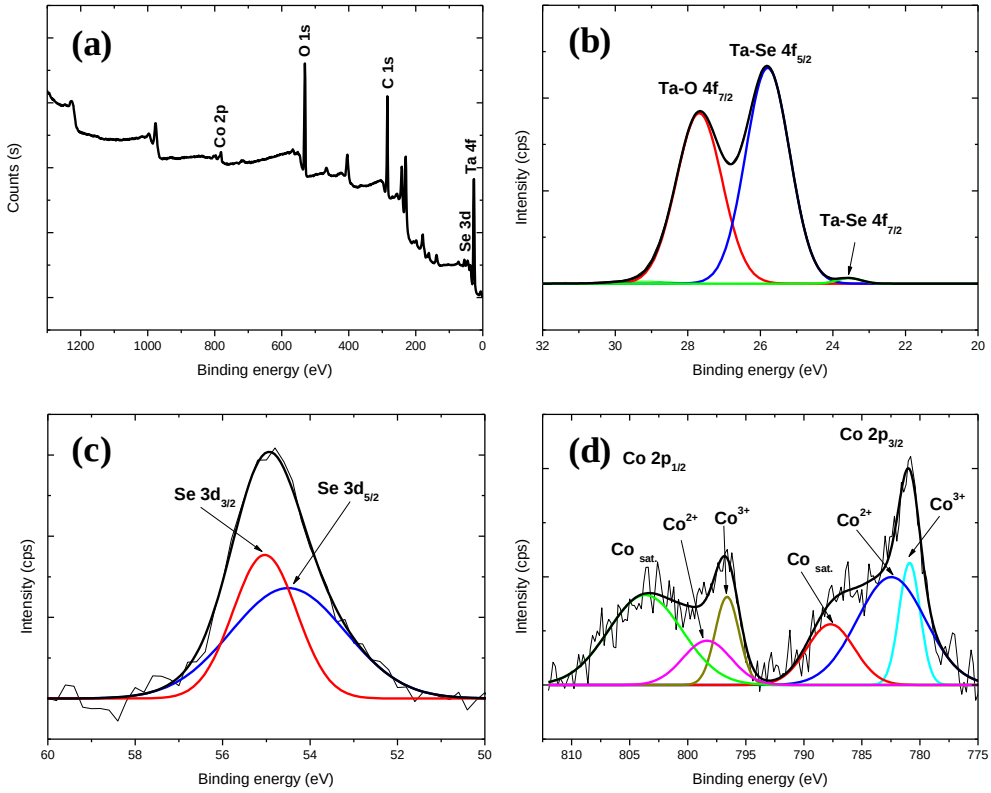

Fig. 4: (a) XPS survey spectra and XPS core-level spectra: (b) Ta 4f, (c) Se 3d, and (d) Co 2p of Co-decorated $TaSe_2$.

The Co-decoration of the $TaSe_2$ ex-situ method resulted in Co/Co_3O_4-$TaSe_2$ hybrid nanomaterial formation. The XRD pattern showed the presence of excess Se, indicating that no bonding was formed between the Co and Se during the decoration of $TaSe_2$. Hence the random distribution of the Co nanoplates on the irregular structures of $TaSe_2$.

5.3.3 Decoration of $TaSe_2$ using Ni nanoparticles

Fig. 5a shows the XRD pattern of the readily synthesised Ni-decorated $TaSe_2$ sample compared to the pristine $TaSe_2$. The Ni-decorated $TaSe_2$ sample comprises 2H-$TaSe_2$ (PDF 01-073-1798) and cubic phase Ni (PDF 01-071-4655) denoted by 'Σ'. The ex-situ method involved adding Ni nanoparticles to $TaSe_2$ and mixing overnight; hence the results obtained are expected. However, the sample also contained Se (PDF 00-042-1425) peak at 44.2 ° 2θ denoted by '*' and $Ni(OH)_2$ (COD #1011134) peak at 38.6 ° 2θ denoted by 'Ω'. Fig. 5b shows the TEM image of the Ni-decorated $TaSe_2$ nanomaterial containing irregular structures similar to pristine $TaSe_2$ and Ni nanoplates within the structures.

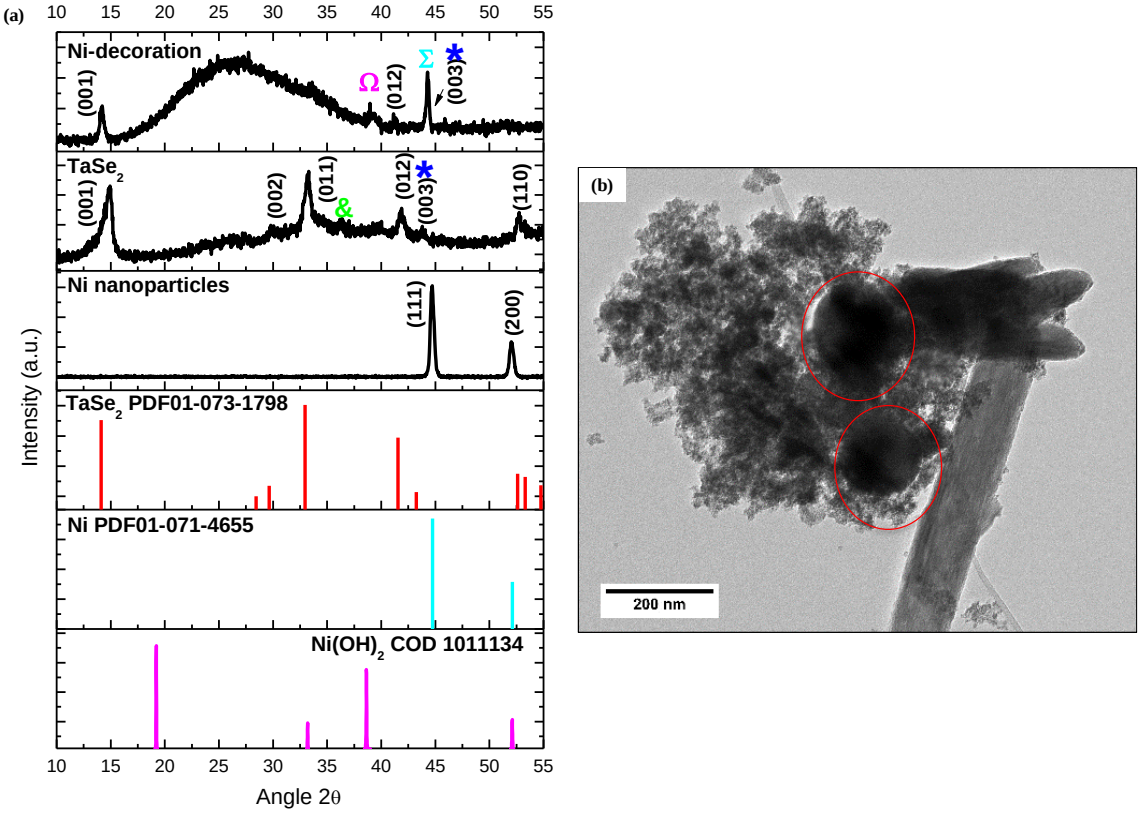

Fig. 5: (a) XRD pattern and (b) TEM images of Ni-decorated $TaSe_2$ nanomaterial; '*', '&', 'Ω', and 'Σ' represent Se, Ta_2O_5, $Ni(OH)_2$, and Ni, respectively.

Fig. 6a shows the XPS survey spectra of the Ni-decorated $TaSe_2$ nanomaterial containing expected species such as Ni, Ta, Se, C, and O, where O was due to the oxidation of the samples and C due to the capping agent used in the synthesis [21]. Fig 6b shows that the Ni-decorated $TaSe_2$ nanomaterial Ta 4f XPS spectra also have two Ta-Se peaks ($4f_{5/2}$ at 25.8 eV and $4f_{7/2}$ at 23.3 eV) attributed to $TaSe_2$ and a Ta-O peak ($4f_{7/2}$ at 27.7 eV) due to oxidation at the surface

of the nanomaterial [19, 20]. Similarly, two peaks of Se 3d XPS spectra at 55.0 eV ($3d_{3/2}$) and 53.2 eV ($3d_{5/2}$) (shown in Fig. 3c) [17, 18]. This confirms that $TaSe_2$ is within the nanomaterial and consistent with the XRD pattern. Fig. 6a shows the Ni 2p XPS spectrum of Ni-decorated $TaSe_2$ nanomaterial with two peaks, Ni $2p_{1/2}$ and Ni $2p_{3/2}$. The Ni $2p_{1/2}$ peak was deconvoluted into peaks contributed by Ni^{2+} at 873.0 eV, Ni^{3+} at 875.7 eV, and the satellite peak denoted as 'sat.' at 879.4 eV [25-27]. Similarly, the Ni^{2+}, Ni^{3+}, and satellite peaks can also be seen from Ni $2p_{3/2}$ at 855.8, 858.1, and 862.4 eV, respectively. The satellite peaks further provide evidence for the presence of Ni^{2+} [28-30]. Fingerle *et al.* reported that Ni^{3+} ions might undergo surface reduction to Ni^{2+} ions; the unstable nature of Ni^{3+} leads to the formation of $Ni(OH)_2$ [27, 29]. Fig. S3a show the O1s spectra deconvoluted to three peaks: metal oxide at 530.2 eV, C-O at 531.5 eV, and C=O at 532.8 eV. The C-O peak is attributed to O^{2-} from the Ta-O and or Ni-O lattice [27]. Similarly, Fig. S3b shows the C 1s XPS spectra consisting of C-C (sp^3), C-O, O-C=O, and C=O.

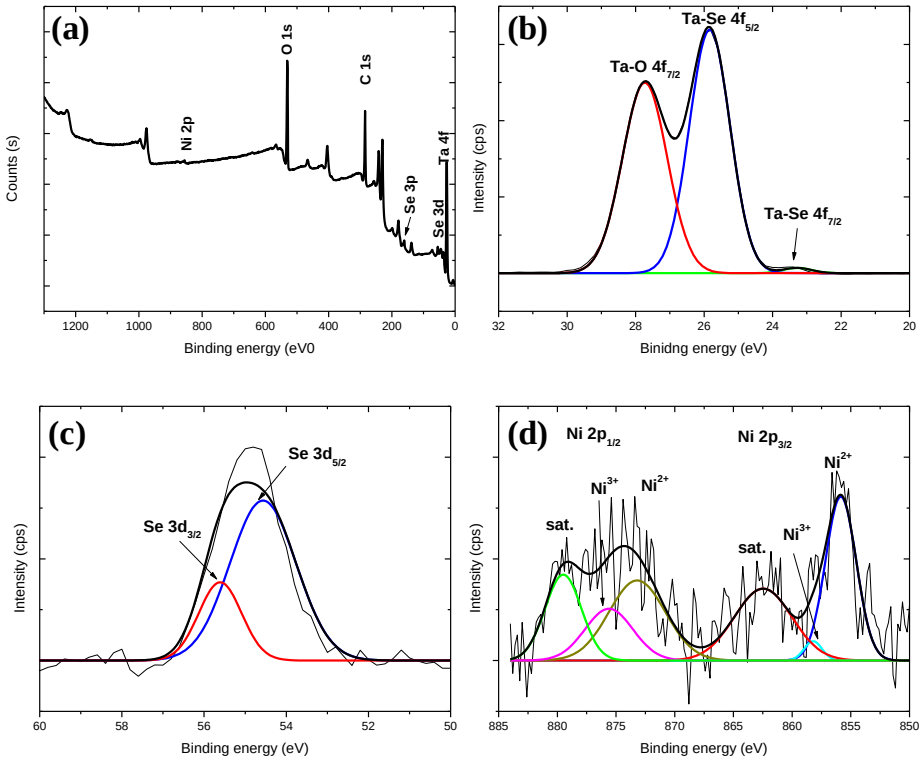

Fig. 6: (a) XPS survey spectra and XPS core-level spectra: (b) Ta 4f, (c) Se 3d, and (d) Ni 2p of Ni-decorated $TaSe_2$.

The Ni-decoration of the $TaSe_2$ ex-situ method resulted in $Ni/Ni(OH)_2$-$TaSe_2$ hybrid nanomaterial formation. No bonding was formed between the Ni and Se during the decoration

of $TaSe_2$. Hence the random distribution of the Ni nanoplates on the irregular structures of $TaSe_2$.

5.3.4 Decoration of $TaSe_2$ using Pt

Fig. 7a shows the XRD pattern of the readily synthesised Pt-decorated $TaSe_2$ sample compared to the pristine $TaSe_2$. The Pt-decorated $TaSe_2$ sample comprises 2H-$TaSe_2$ (PDF 01-073-1798) and cubic phase Pt (PDF 01-087-0640) denoted by 'σ'. However, the sample also contained PtO (COD #1522314) peak at 51.2° 2θ denoted by 'ϖ' and PtO_2 (COD #1537410) peak at 39.8° 2θ denoted by 'κ'. The ex-situ method involved mixing Pt nanoparticles with $TaSe_2$. Therefore, the results obtained are expected. Fig. 7b shows the TEM image of the Pt-decorated $TaSe_2$ nanomaterial containing irregular structures similar to pristine $TaSe_2$ samples and Pt-agglomerated nanoparticles within the structures.

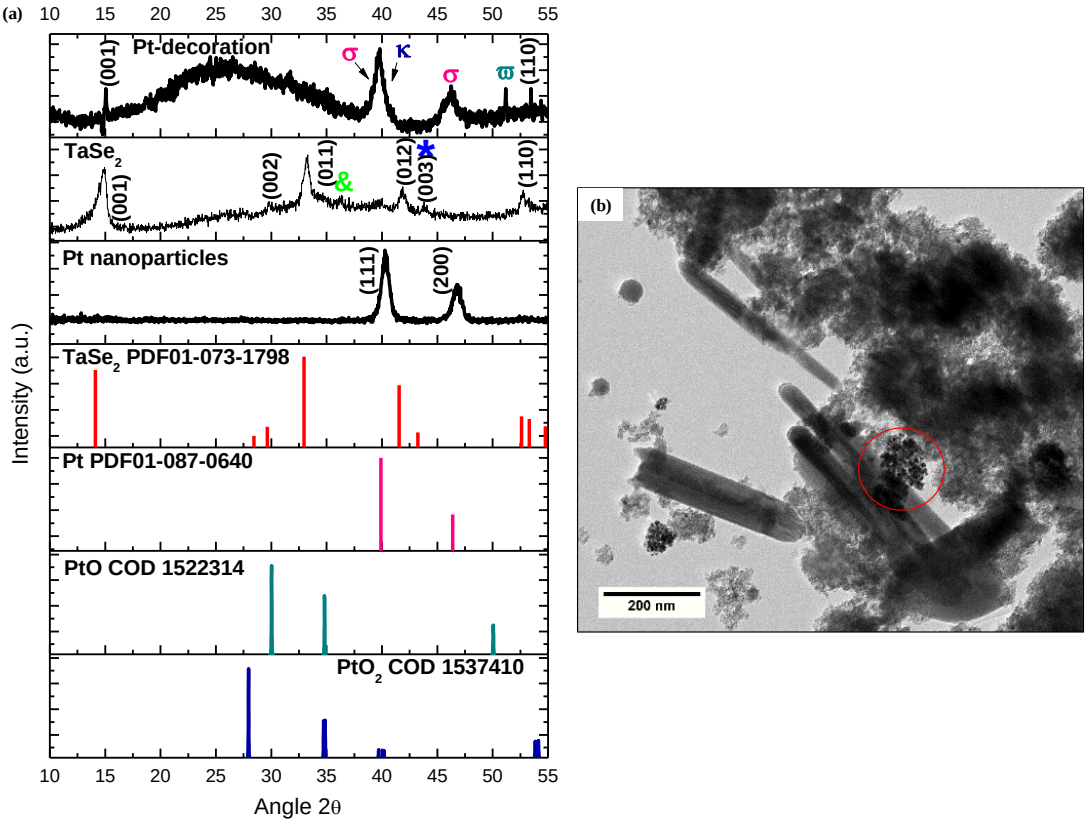

Fig. 7: (a) XRD pattern and (b) TEM images of Pt-decorated $TaSe_2$ nanomaterial; '*', '&', 'σ', 'ϖ', and 'κ' represent Se, Ta_2O_5, PtO, and PtO_2, respectively.

Fig. 8a shows the XPS survey spectra of the Pt-decorated $TaSe_2$ nanomaterial containing expected species such as Pt, Ta, Se, C, and O, where O was due to the oxidation of the samples and C due to the capping agent used in the synthesis [17]. Fig 8b shows that the Pt-decorated $TaSe_2$ nanomaterial Ta 4f XPS spectra also have two Ta-Se peaks ($4f_{5/2}$ at 25.8 eV and $4f_{7/2}$ at 23.5 eV) attributed to $TaSe_2$ and two Ta-O peaks ($4f_{5/2}$ at 28.9 eV and $4f_{7/2}$ at 27.6 eV) due to oxidation at the surface of the nanomaterial [18, 19]. Se 3d XPS spectra contained two peaks at 54.8 eV ($3d_{3/2}$) and 54.3 eV ($3d_{5/2}$) (shown in Fig. 3c) [17, 18]. This confirms that $TaSe_2$ is within the nanomaterial. The Pt 4f XPS spectrum has three possible chemical states, namely, Pt^0 with binding energies at 70.7 ($4f_{7/2}$) and 74.7 eV ($4f_{5/2}$) due to metallic Pt nanoparticles, Pt^{2+} at 72.1 eV ($4f_{7/2}$) due to PtO, and Pt^{4+} at 73.8 eV ($4f_{7/2}$) due to PtO_2, respectively [31]. Fig. S3a show the O1s spectra deconvoluted to three peaks: metal oxide at 530.3 eV, C-O at 531.6 eV, and C=O at 533.1 eV. The C-O peak is attributed to O^{2-} from the Ta-O and or Ni-O lattice. Similarly, Fig. S3b shows the C 1s XPS spectra consisting of C-C (sp^3), C-O, O-C=O, and C=O. The Pt-decoration of the $TaSe_2$ ex-situ method resulted in the formation of Pt/PtO/PtO_2-$TaSe_2$ hybrid nanomaterial (PTO- $TaSe_2$).

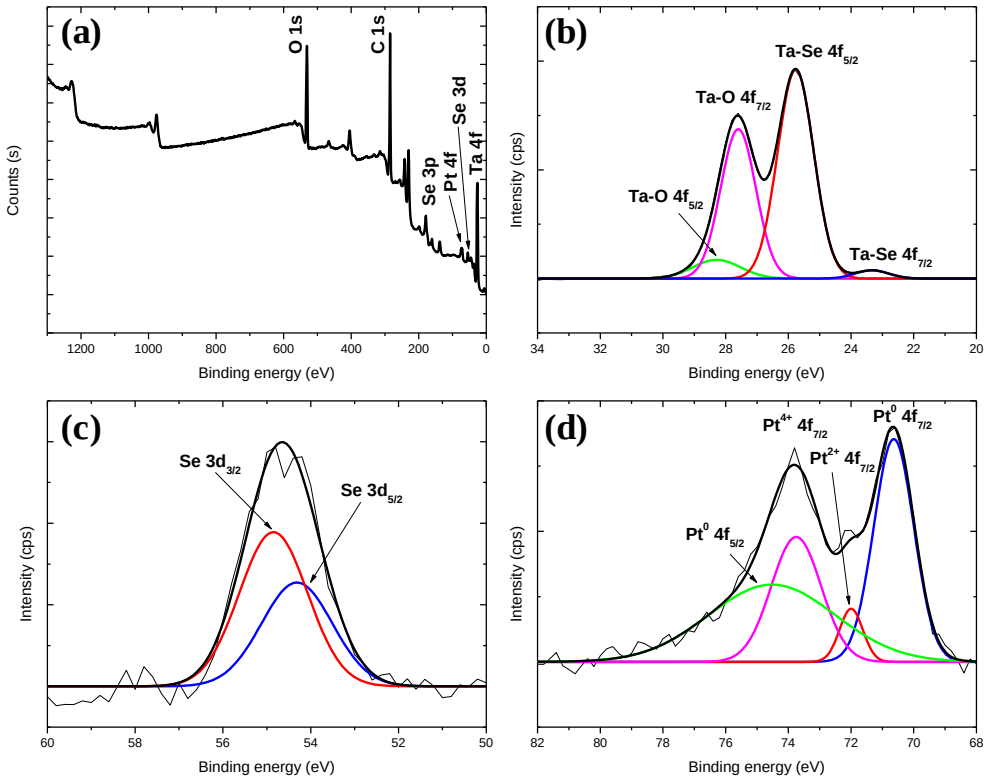

Fig. 8: (a) XPS survey spectra and XPS core-level spectra: (b) Ta 4f, (c) Se 3d, and (d) Pt 4f of Pt-decorated $TaSe_2$.

5.4. Electrochemical characterisation

The LSV polarisation curve was used to determine the onset potential (η) and overpotential at 10 mA/cm^2 (η_{10}). Fig. 9a shows the LSV polarisation curve of $TaSe_2$ with an onset potential of 194 mV compared to Pt/C at 97 mV. The overpotential at 10 mA/cm^2 is the operating current density used for a cost-competitive photoelectrochemical cell [32]. To deliver a current density of 10 mA/cm^2, $TaSe_2$ returned an overpotential of 721 mV. Fig. 9b shows the Tafel plot used to calculate the Tafel slope (b) and the exchange current density. The Tafel slope was calculated from the Tafel equation shown below:

$$\eta = b \log j + a$$

where η is the overpotential, b is the Tafel slope, and a is the Tafel constant. The Tafel slope reveals the intrinsic property of the electrocatalyst as well as the reaction mechanism. The Tafel slope's value is determined by HER's rate-limiting step [33]. The measured Tafel slope for Pt/C is 77 mV/dec, double the reported value of 30.6 mV/dec [34]. This illustrated that the Volmer-Heyrovsky mechanism dominated the HER process [35]. The Tafel slope of $TaSe_2$ was higher than Pt/C at the value of 206 mV/dec, indicating a low catalytic activity. In this case, the rate-determining step was the Volmer step [36]. As such, this motivated us to form hybrid structures with $TaSe_2$ to enhance its electrocatalytic activity for HER.

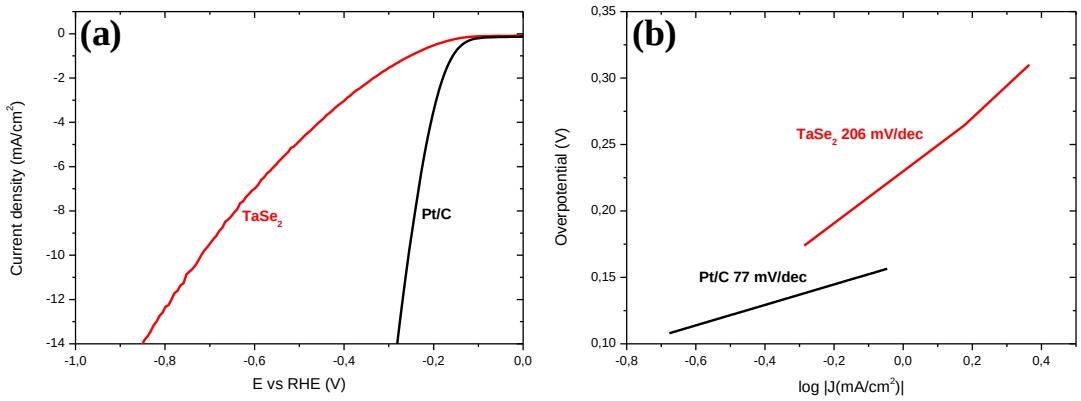

Fig. 9: (a) Polarisation curves of $TaSe_2$ nanomaterial and Pt/C, and (b) Tafel plots of $TaSe_2$ nanomaterial and Pt/C.

The HER activity of $TaSe_2$ decorated using various transition metals (20% wt. each; Co, Ni, and Pt) was evaluated. Fig. 10a shows that the PTO-$TaSe_2$ electrocatalyst exhibits superior HER performance compared with $TaSe_2$, with an extremely low overpotential of 262 mV (to

deliver a current density of 10 mA/cm^2). In addition, the overpotential of PTO-$TaSe_2$ is slightly higher than Pt/C at 256 mV. Furthermore, Fig.10a shows that Co/Co_3O_4-$TaSe_2$ and Ni/$Ni(OH)_2$-$TaSe_2$ also resulted in much lower overpotentials of 685 and 558 mV compared to $TaSe_2$ (to deliver a current density of 10mA/cm^2), respectively. As such, the trend is as follows: PTO-$TaSe_2$ < Ni/$Ni(OH)_2$-$TaSe_2$ < Co/Co_3O_4-$TaSe_2$. Fig. 10b shows that the same trend was observed with the Tafel slopes; the values are summarised in Table 2.

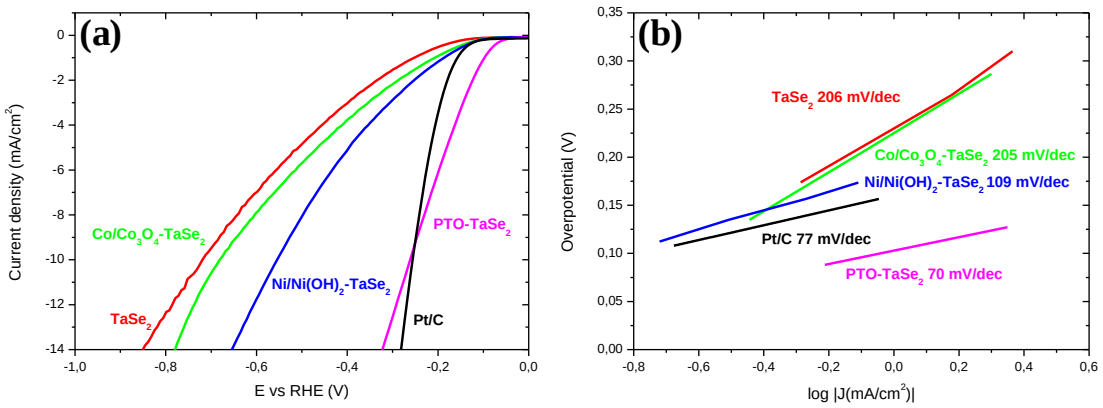

Fig. 10: (a) Polarisation curves and (b) Tafel plots of the Co-, Ni-, and Pt-decorated $TaSe_2$ nanomaterials compared with pristine $TaSe_2$ and Pt/C.

Exchange current density (j_0) is a crucial kinetic parameter used to assess the performance of the electrocatalyst. The exchange current density reveals the electron transfer rate at zero overpotential. It can be calculated from the Tafel equation (log J = a), where a is the x-intercept of the Tafel plot. As such, the exchange current density is directly proportional to the catalytic performance. Table 2 indicates that PTO-$TaSe_2$ nanomaterial has the highest exchange current density, and $TaSe_2$ with the lowest exchange current density compared to the other nanomaterials. This trend is consistent with the LSV and Tafel slope results. However, Pt/C was expected to have the highest exchange current density value compared to all the electrocatalysts, but the value lies slightly below the PTO-$TaSe_2$ electrocatalyst. The exchange current density trend was as follows: PTO-$TaSe_2$ > Pt/C > Ni/$Ni(OH)_2$-$TaSe_2$ > Co/Co_3O_4-$TaSe_2$ > $TaSe_2$. The tailing of the LSV may be the reason for this trend.

Table 2: Electrocatalytic parameters of decorated $TaSe_2$ electrocatalysts in comparison to bare $TaSe_2$ and Pt/C electrocatalyst

Sample	**η (mV)**	**η_{10} (mV)**	**b (mV/dec)**	**j_0 (mA/cm^2)**	**R_{ct} (Ohm)**	**C_{dl} (mF/cm^2)**
$TaSe_2$	160	1017	301	0.472	433	2.65
Ni/Ni(OH)$_2$-$TaSe_2$	142	741	118	0.827	257	3.06
Co/Co_3O_4-$TaSe_2$	146	795	140	0.476	411	3.01
PTO-$TaSe_2$	57	501	60	1.352	89	3.10
Pt/C	97	256	77	0.846	n/a	n/a

Electrochemical impedance spectroscopy was used to investigate the electron transport properties of the electrocatalyst. Rct is charge transfer resistance, the smaller the Rct values, the faster the transfer kinetics. Fig. 11a shows the Nyquist plots, which show improvement in the performance of $TaSe_2$ due to the formation of hybrid nanomaterials using transition metal nanoparticles. There was a significant Rct reduction from $TaSe_2$ to PTO-$TaSe_2$ electrocatalyst. As such, this denotes a substantial improvement in the charge transfer kinetics of HER in the electrocatalytically activated electrocatalyst. Fig. 11 c shows the equivalence circuit fitted to the Nyquist plots. The trend R_{ct} was as follows: PTO-$TaSe_2$ < Ni/Ni(OH)$_2$-$TaSe_2$ < Co/Co_3O_4-$TaSe_2$ < $TaSe_2$.

The electrochemical double-layer (C_{dl}) is calculated using cyclic voltammetry (CV) measurements at different scan rates. Fig. S5 shows the CV curves used to obtain the change in current density (between the anode and cathode) at zero potential for each scan rate (15, 20, 25, 30, 35, 40). The change in current density vs the scan rates was plotted, resulting in a linear plot, where C_{dl} = gradient. Fig 11b shows the C_{dl} plots. As expected, the Cdl values trend agrees with the Rct trend's reverse (summarised in Table 2). The electrochemically active surface area (ECSA) can be calculated by dividing the Cdl value of the electrocatalyst by the specific capacitance (Cs) of 40 μF/cm^2 from the literature [37, 38]. The ECSA values of the electrocatalysts in this study are summarised in Table S1. where a Cs value of 40 μF/cm^2 was used in the calculations. PTO-$TaSe_2$ electrocatalyst has the highest ECSA value of 15.2 cm^{2,} and $TaSe_2$ with the lowest value of 13.0 cm^2. The stability of the best-performing PTO-$TaSe_2$ electrocatalyst was evaluated by performing chronoamperometry studies. Fig. 11d shows the

chronoamperometry profiles; when a potential of 500 mV was applied, the current density increased exponentially for approximately ~4 h and began to stabilise for 1 h. This indicates that PTO-$TaSe_2$ generates more current the more it is being used.

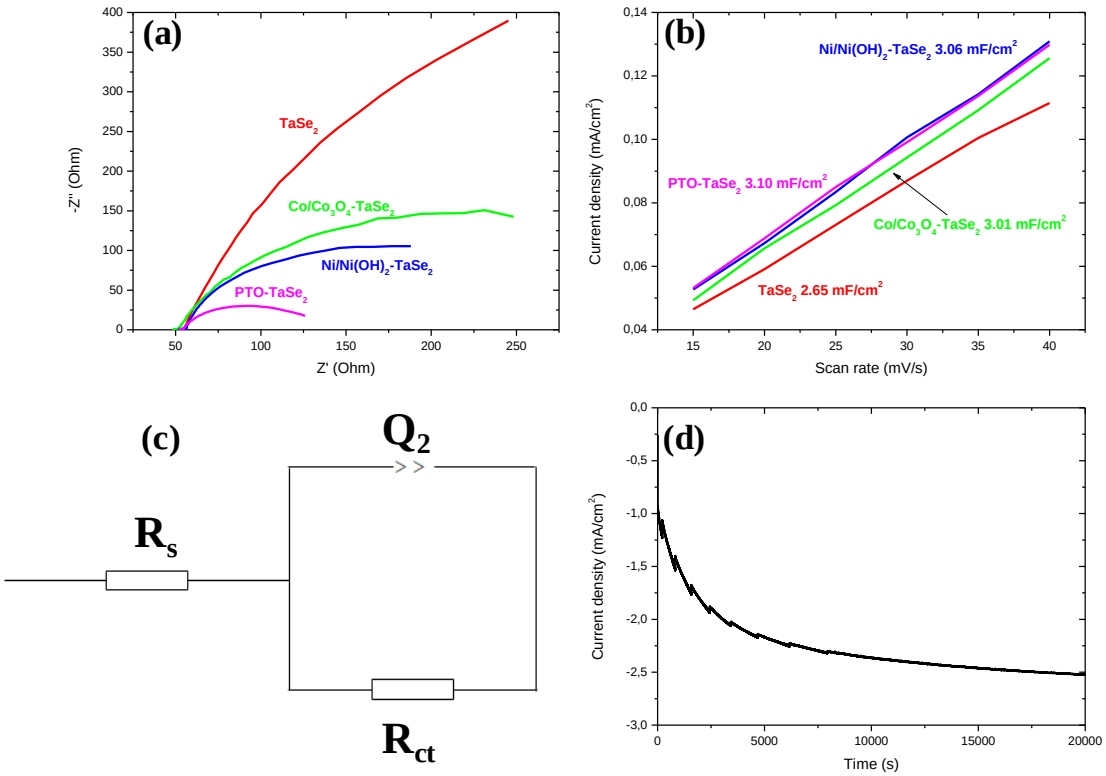

Fig. 11: (a) Nyquist plots, and (b) exchange current density (j_0) of $TaSe_2$ compared to the resultant nanomaterials after the decoration of $TaSe_2$, (c) equivalence circuit fitted to the Nyquist plots nanomaterials synthesised, and (d) Chronoamperometry for PTO-$TaSe_2$ nanomaterial at 500 mV vs RHE applied potential and 13 000 s time scale.

According to the volcano plot, the trend for the electrocatalyst HER activity under alkaline conditions is as follows: Pt > Ni > Co [38]. Pt has the highest electrocatalytic activity. As such, the decoration of $TaSe_2$ with these transition metals resulted in enhanced electrocatalytic activity following the volcano plot trend. PTO-$TaSe_2$ hybrid material was the best-performing electrocatalyst. The increase in the C_{dl} value from one $TaSe_2$-based electrocatalyst to another suggests an increase in the surface area of the electrocatalyst or the introduction of new active sites [37, 38]. Najafi *et al.* formed a TaS_2/$TaSe_2$ hybrid and obtained enhanced HER activity under alkaline conditions [1]. They reported that forming the hybrid tunes the Gibbs free energy of the adsorbed hydrogen onto the TaS_2 basal planes to the optimal thermo-neutral value [1].

5.5. Conclusion

This work evaluated the electrocatalytic activity of 2H- $TaSe_2$ nanomaterials. The performance of $TaSe_2$ was relatively poor, with high overpotential, high onset potential, low exchange current density, and a high Tafel slope. This motivated us to find new ways to enhance the performance of $TaSe_2$. The enhancement was obtained by decorating $TaSe_2$ with transition metals such as Pt, Ni, and Co. The hybrids' electrocatalytic activity followed the volcano plot trend, i.e. Pt > Ni > Co. As such, the PTO-$TaSe_2$ electrocatalyst (resulted from decorated $TaSe_2$ with 20 % wt Pt using the ex-situ method) presented the lowest overpotential at a current density of 10 mA/cm^2, Tafel slope, exchange current density, and R_{ct}, as well as the highest C_{dl} and ECSA. Therefore, the process worked and has the potential to produce electrocatalysts that are comparable to Pt.

5.6. References

[1] L. Najafi, S. Bellani, R. Oropesa-Nuñez, B. Martín-García, M. Prato, L. Pasquale, J. Panda, P. Marvan, Z. Sofer, F. Bonaccorso, *ACS Catal.*, 2020, 10, 3313−3325.

[2] M. Momirlan, T. N. Veziroglu, *Int. J. Hydrogen Energy*, 2005, 30, 795−802.

[3] X. Zou, Y. Zhang, *Chem. Soc. Rev.*, 2015, 44, 5148−5180.

[4] Z. Cao, Q. Chen, J. Zhang, H. Li, Y. Jiang, S. Shen, G. Fu, B. Lu, Z. Xie, L. Zheng, *Nat. Commun.*, 2017, 8, 15131.

[5] Z. Liu, J. Qi, M. Liu, S. Zhang, Q. Fan, H. Liu, K. Liu, H. Zheng, Y. Yin, C. Gao, *Angew. Chem., Int. Ed.*, 2018, 57, 11678−11682.

[6] J. Greeley, T. F. Jaramillo, J. Bonde, I. B. Chorkendorff, J. K. Nørskov, Nat. Mater. 2006, 5, 909−913.

[7] H. Xu, J. Wei, K. Zhang, Y. Shiraishi, Y. Du, *ACS Appl. Mater. Interfaces*, 2018, 10, 29647−29655.

[8] D. Merki, X. Hu, *Energy Environ. Sci.*, 2011, 4, 3878−3888.

[9] M. Pumera, Z. Sofer, A. Ambrosi, *J. Mater. Chem. A*, 2014, 2, 8981−8987.

[10] X. Shi, M. Fields, J. Park, J. M. McEnaney, H. Yan, Y. Zhang, C. Tsai, T. F. Jaramillo, R. Sinclair, J. K. Nørskov, et al., *Energy Environ. Sci.*, 2018, 11, 2270−2277.

[11] B. Martín-García, D. Spirito, S. Bellani, M. Prato, V. Romano, A. Polovitsyn, R. Brescia, R. Oropesa-Nuñez, L. Najafi, A. Ansaldo, G. D'Angelo, V. Pellegrini, R. Krahne, I. Moreels, F. Bonaccorso, *Small*, 2019, 15, 1904670.

[12] H. Tsai, F. Liu, J. Liou, C. Chi, S. Tang, C. Wang, H. Ouyang, Y. Chueh, C. Liu, S. Zhou, W. Woon, *ACS Omega*, 2019, 4, 17536−17541.

[13] Y. Liu, J. Wu, K. P. Hackenberg, J. Zhang, Y. M. Wang, Y. Yang, K. Keyshar, J. Gu, T. Ogitsu, R. Vajtai, J. Lou, P. M. Ajayan, B. C. Wood, B. I. Yakobson, *Nat. Energy*, 2017, 2, 17127.

[14 J. Shi, Z. Wang, S. Zhang, L. Xiao, Y. Huan, Y. Gong, Z. Zhang, Y. Li, X. Zhou, M. Hong, Q. Fang, Q. Zhang, X. Liu, L. Gu, Z. Liu, Y. Zhang, *Nat. Commun.*, 2017, 8, 958.

[15] B. Han, S. H. Noh, D. Choi, M. H. Seo, J. Kang, J. Hwang, *J. Mater. Chem. A*, 2018, 6, 20005−20014.

[16] L. Najafi, S. Bellani, R. Oropesa-Nuñez, B. Martín-García, M. Prato, V. Mazánek, D. Debellis, S. Lauciello, R. Brescia, Z. Sofer, *J. Mater. Chem. A*, 2019, 7, 25593−25608.

[17] J. Zhang, J. Wu, X. Zou, K. Hackenberg, W. Zhou, W. Chen, J. Yuan, K. Keyshar, G. Gupta, A. Mohite, P. M. Ajayan, J. Lou, *Mater. Today*, 2019, 25, 28−34.

[18] H. Wang, Y. Chen, C. Zhu, X. Wang, H. Zhang, S. Tsang, H. Li, J. Lin, T. Yu, Z. Liu, E. H. T. Teo, *Adv. Funct. Mater.*, 2020, 30, 2001903.

[19] J. Zhang, Y. Wang, C. Zhang, H. Gao, L. Lv, L. Han, Z. Zhang, *ACS Sustainable Chem. Eng.*, 2018, 6, 2231−2239.

[20] H. Luo, W. Xie, J. Tao, I. Pletikosic, T. Valla, G. S. Sahasrabudhe, G. Osterhoudt, E. Sutton, K. S. Burch, E. M. Seibel, J. W. Krizan, Y. Zhu, R. J. Cava, *Chem. Mater.*, 2016, 28, 1927−1935.

[21] K. Horiba, K. Ono, J. H. Oh, T. Kihara, S. Nakazono, M. Oshima, O. Shiino, H. W. Yeom, A. Kakizaki, Y. Aiura, *Phys. Rev. B*, 2002, 66, 073106.

[22] M. Smyrnioti, T. Loannides, *Intech Open Science*, Chapter 3, 50-66.

[23] C. Wang, C. Zhang, W. Hua, Y. Guo, G. Lu, S. Gil, A. Giroir-Fendler, *Chemical Engineering Journal.*, 2017, 315, 392-402.

[24] Q. Huang, J. Zhang, Z. He, P. Shi, X. Qin, W. Yao, *Chemical Engineering Journal*, 2017, 313, 1088-1098.

[25] N. K. M. Safeer, C. Alex, R. Jana, A. Datta, N. S. John, *J. Mater. Chem. A*, 2022.

[26] M. A. Airo, F. Otieno, L. Mxakaza, A. Ipadeola, R. S. Kadzutu-Sithole, L. F. E. Machogo-Phao, C. Billing, M. J. Moloto, N. Moloto, *RSC advances*, 10 (65), 2020, 39509−39520.

[27] M. Fingerle, S. Tengeler, W. Calvet, T. Mayer, W. Jaegermann, *J. Electrochem. Soc.*, 2018, 165, H3148– H3153.

[28] X. Wang, Y. V. Kolen'ko, X. Q. Bao, K. Kovnir, L. Liu, *Angew. Chem., Int. Ed.*, 2015, 54, 8188−8192.

[29] B. Conway, B. Tilak, *Electrochim. Acta*, 2002, 47, 3571−3594.

[30] Z. B. Ndala, N. P. Shumbula, S. Nkabinde, T. Kolokoto, S. Gqoba, C. Linganiso, N. Moloto, *Journal of Electroanalytical Chemistry*, 2022, 918, 116464.

[31] J. Yang, A. R. Mohmad, Y. Wang, R. Fullon, X. Song, F. Zhao, I. Bozkurt, M. Augustin, E. J. Santos, H. S. Shin, *Nat. Mater.*, 2019, 18, 1309–1314.

[32] P. Connor, J. Schuch, B. Kaiser, W. Jaegermann, *Z. Phys. Chem.*, 2020, 234, 979–994.

[33] C. C. L. McCrory, S. Jung, J. C. Peters, T. F. Jaramillo, *J. Am. Chem. Soc.*, 2013, 135, 16977.

[34] R. Boggio, A. Carugati, S. Trasatti, *J. Appl. Electrochem.*, 1986, 17, 828.

[35] M. J. Gira, K. P. Tkacz, J. R. Hampton, *Nano Converg.*, 2016, 3, 6.

[36] P. Quaino, F. Juarez, E. Santos, W. Schmickler. *Beilstein. J. Nanotechnol.*, 2014, *5* (1), 846-854.

[37] H. U. Kim, M. Kim, H. Seok, K. Y. Park, J. Y. Moon, J. Park, B. S. An, H. J. Jung, V. P. Dravid, D. Whang, J. H. Lee, T. Kim, *ChemSusChem*, 2021, 14, 1344–1350.

[38] Z. Ndala, N. Shumbula, S. Nkabinde, T. Kolokoto, O. Nchoe, P. Shumbula, Z. N. Tetana, E. C. Linganiso, S. S. Gqoba, N. Moloto, *Nanomaterials*, 2020, 10, 1786.

Chapter 5

Supplementary information

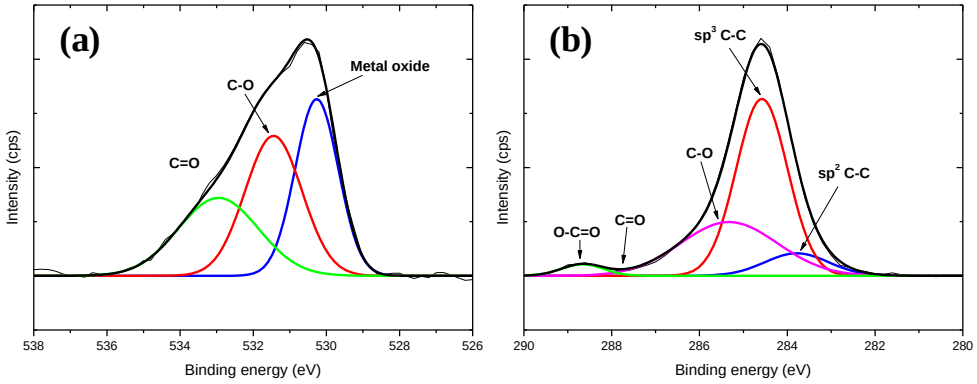

Fig. S1: (a) O1s and (b) C1s XPS core-level spectra of $TaSe_2$ nanomaterials.

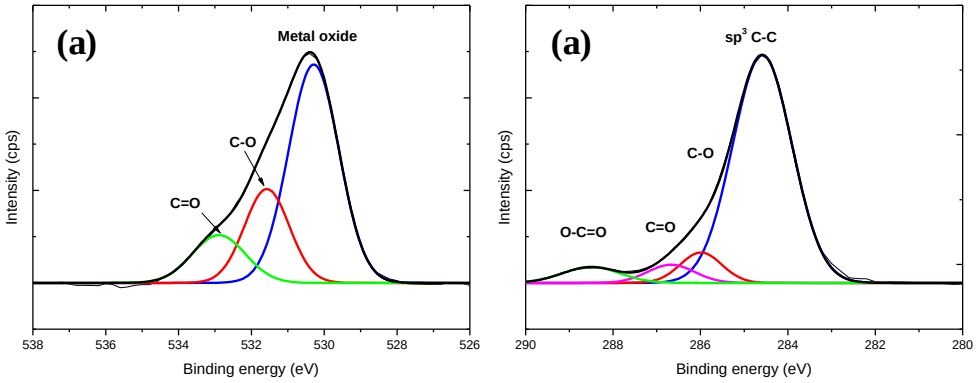

Fig. S2: (a) O1s and (b) C1s XPS core-level spectra of Co-decorated ex-situ $TaSe_2$ nanomaterials.

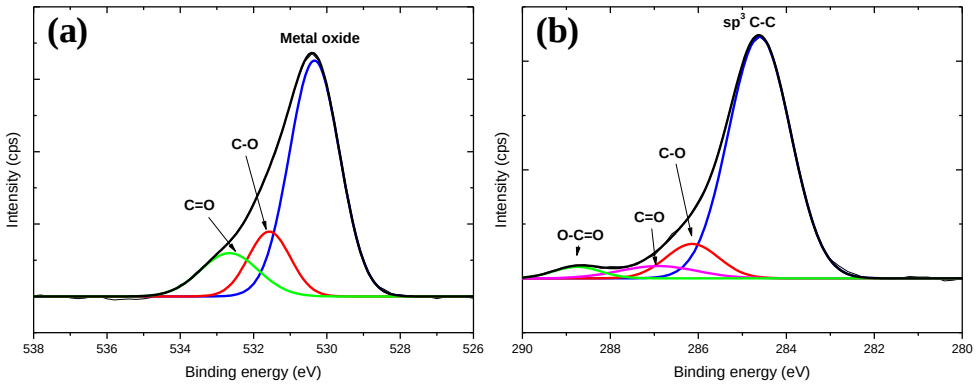

Fig. S3: (a) O1s and (b) C1s XPS core-level spectra of Ni-decorated ex-situ $TaSe_2$ nanomaterials.

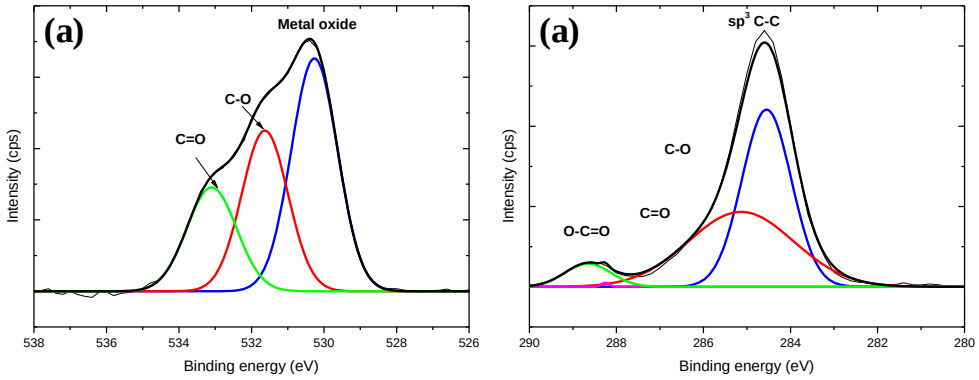

Fig. S4: (a) O1s and (b) C1s XPS core-level spectra of Pt-decorated ex-situ $TaSe_2$ nanomaterials.

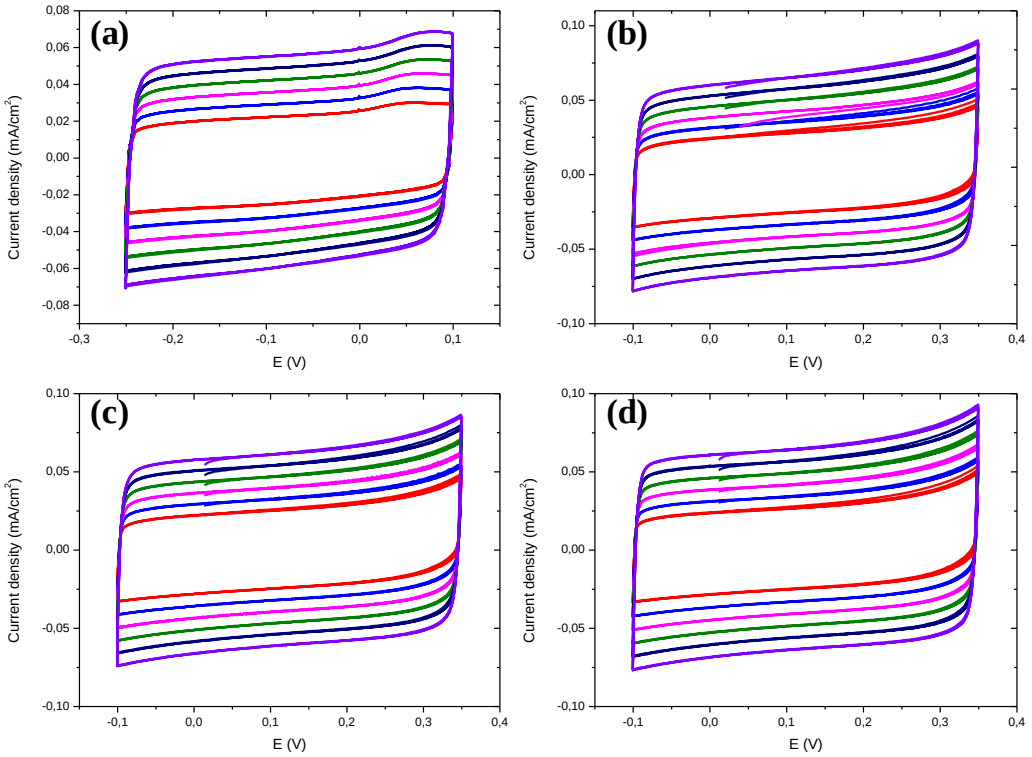

Fig. S5: (a) $TaSe_2$, (b) $Ni/Ni(OH)_2$-$TaSe_2$, (c) Co/Co_3O_4-$TaSe_2$, (d) PTO-$TaSe_2$.

Table S1: ECSA of the decorated $TaSe_2$ in comparison to pristine $TaSe_2$ calculated using electrochemical double-layer capacitance (C_{dl}) and specific capacitance (Cs) of 40 μF/cm^2

Sample	**ECSA (cm^2)**
$TaSe_2$	14.7
Ni/Ni(OH)$_2$-$TaSe_2$	14.8
Co/Co_3O_4-$TaSe_2$	70.6
PTO-$TaSe_2$	56.4

Chapter 6

Conclusions

6.1. Overall conclusions

Herein we reported on the successful synthesis of $NbSe_2$ and $TaSe_2$ 2D materials. These materials are different from their 2D counterparts such as MoS_2, $MoSe_2$, WS_2 and WSe_2 due to their properties. More specifically for electrocatalytic application, they have been shown to have active sites not only on the edges but also on the basal planes. In addition, the 2H phase is known to be more metallic rather than the semiconducting 1T phase (these are the most common phases). Therefore this suggests that they will outperform those of group 6 TMDCs ($MoSe_2$ and WSe_2). Shown in Fig. 1 is the Volcano Plot of some of the commonly studied TMDCs. While these are metal sulphides, the trend however suggests that the performance of Nb and Ta TMDCs is closer to that of Pt. The chemistry of selenides is similar to sulfides with the selenides being slightly more metallic.

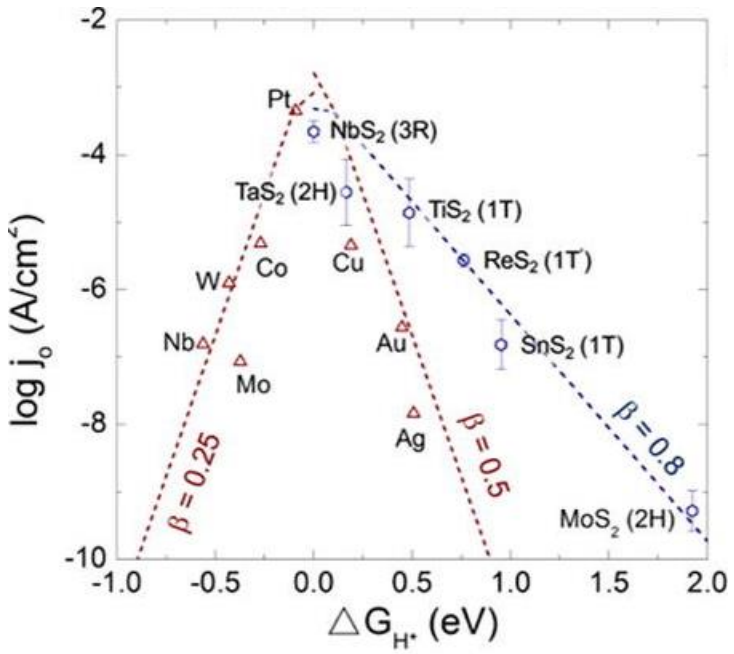

Fig. 1: Volcano plot of the exchange current density as a function of the DFT-calculated Gibbs free energy of adsorbed atomic hydrogen at the basal planes of 2D TMDCs and pure metals [1].

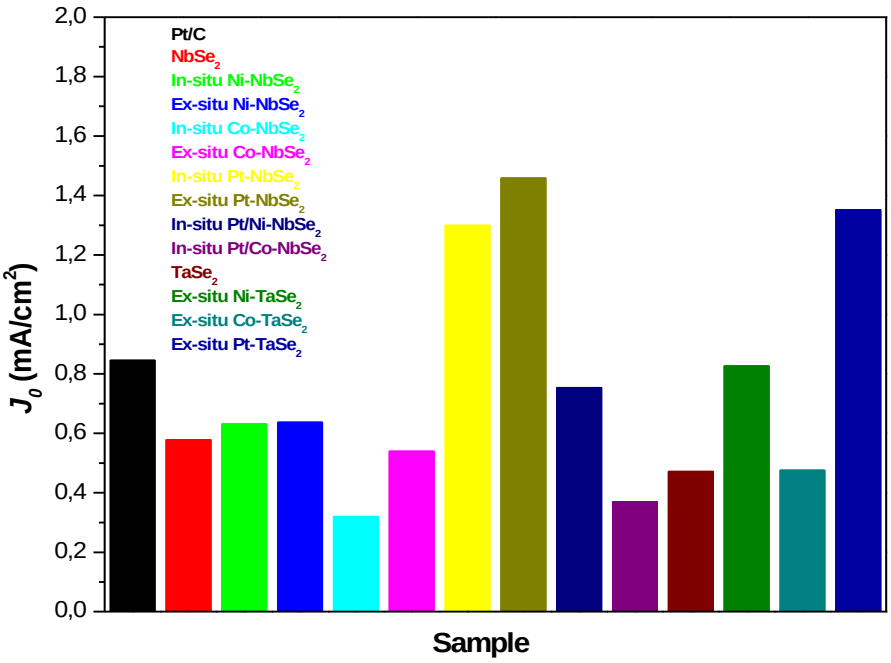

Fig. 2: Plot of exchange current densities of the synthesized electrocatalysts.

In this study, pristine $NbSe_2$ was a slightly better-performing catalyst than $TaSe_2$. While both were poorer than the model Pt/C catalyst. This trend was similar to the one observed in Fig. 1. To improve their performance, hybrid nanostructures were formed with Ni, Co, Pt, Pt/Ni and Pt/Co based nanocrystals. The Pt-based nanohybrids had the highest exchange current densities (good catalyst) for both $NbSe_2$ and $TaSe_2$ as compared to the model Pt/C. This was attributed to the increased surface area as the platinum particles are supported on the 2D materials as well as the additional active sites of the 2D materials. Moreover, the Ni-based catalysts showed promising activities towards the HER as significant improvement of both the $NbSe_2$ and $TaSe_2$ were observed with the latter having j_0 similar to the model Pt/C electrocatalyst. Finally, the ex-situ method for the formation of hybrids appeared to be the better method as it resulted in higher catalytic activities. This can be attributed to the presence of metal nanoparticles and the minimization of oxide formation.

While this study has yielded promising results, further improvements may result in better performance, such as:

- Minimization of the oxidation of the metallic particles using a glove box.

- Electrochemical activation of the active site by performing a 1000 cycles of CV prior to measurements. This has been shown to increase performance, although this is not yet well understood [2].
- Performing ligand exchange on $NbSe_2$ and $TaSe_2$ where the long-chain OLA is replaced by shorter molecules. This has been shown to be effective in solar cell application of the capped metal chalcogenides. The shorter molecules result in a compact film thus allowing for better electron flow [3].

Finally, the obtained results will contribute effectively to the field and will edge us closely to the discovery of non-noble metal electrocatalysts or electrocatalysts where noble metals are used with better performance compared to the model Pt/C electrocatalyst, as in our case.

6.2. References

[1] T. F. Jaramillo, *et al.*, *Science*, 2007, 317 (5834), 100.

[2] Z. B. Ndala, N. P. Shumbula, S. Nkabinde, T. Kolokoto, S. Gqoba, C. Linganiso, N. Moloto, *Journal of Electroanalytical Chemistry*, 2022, 918, 116464.

[3] T. Xaba, M. J. Moloto, O. B. Nchoe, Z. Nate, N. Moloto, Chalcogenide Letters, 2017, 337 – 346.